

ABSTRACT

Title of Dissertation: DEVELOPMENT OF NANOPARTICLE-BASED
INTRACELLULAR DUAL SENSING AND
ACTUATION MODALITIES

Lauren D. Field, Doctor of Philosophy, 2017

Dissertation directed by: Igor L. Medintz
Naval Research Laboratory
Ian White
Fischell Department of Bioengineering

The integration of therapeutics with diagnostic agents, or theranostics, is vital for the development of novel and effective disease treatments. To effectively design new and efficient theranostic materials, a thorough understanding of the carrier ensemble, the interactions within the construct components, and the surrounding environment is required. This dissertation focuses on the development of new strategies to produce an effective ‘toolbox’ of nanoscale theranostics, namely through the use of a central NP scaffold and the visualization technique of Förster Resonance Energy Transfer (FRET). The NP scaffold used throughout this work, the semiconductor quantum dot (QD), is ideal for visualizing sensing modalities due to their high quantum yield (QY), tunable, narrow and symmetric emission profiles with broad, far-UV excitation, and resistance to photobleaching - making them optimal FRET donors. We first examined the intracellular assembly of QDs to proteins by injecting 545 nm emitting QDs, coated with various capping ligands, into cells transfected to express mCherry at two distinct intracellular locations: the cytosol and the plasma

membrane. We found that the small, zwitterionic capping ligand CL4 and the cytosolically located mCherry protein assembled into the most efficient FRET complexes. We used this knowledge to design and implement a novel intracellular actuation modality for drug delivery that used a 520 nm emitting QD with the carrier maltose binding protein appended to the surface and carrying drug or dye conjugated to a maltose analog, β -cyclodextrin in the binding pocket. Rather than relying on intracellular environmental changes or external stimuli to actuate release, the addition of the innocuous sugar maltose to the medium induced cargo actuation and could be visualized *via* FRET. Finally, the same methods were implemented to develop a novel pH sensor to report on the extracellular changes that occur in tumor development where the physiological pH is lowered dramatically. Using a 464 nm QD scaffold conjugated to pH-responsive FITC, we successfully monitored changes in extracellular pH and accurately determined unknown pH values. With the work in this thesis, we believe we have contributed greatly to the advancement and development NPs for the design and implementation of sensing and actuation complexes.

**DEVELOPMENT OF NANOPARTICLE-BASED
INTRACELLULAR DUAL SENSING AND ACTUATION
MODALITIES**

Lauren D. Field

Dissertation submitted to the Faculty of the Graduate School of the
University of Maryland, College Park in partial fulfillment
of the requirements for the degree of
Doctorate of Philosophy

2017

Committee Members:
Professor Ian White, Co-chair
Dr. Igor L. Medintz, Co-chair
Professor Yu Chen
Dr. James Delehanty
Professor Philip DeShong, Dean's Representative

DEDICATION

This work is dedicated to:

My Parents, Brownlee Dickenson Field and Kim Georgette Kvocka, for their unfailing support and without whom this degree would have never been completed.

I am so grateful and so blessed to call you my parents.

ACKNOWLEDGEMENTS

First, I would like to thank my Naval Research Lab advisors, Dr. Igor Medintz and Dr. James Delehanty, for their unfailing support and assistance in completing this work. I have learned so much at NRL and this dissertation could not have happened without your encouragement. Second, I would like to thank my lab members: Dr. Joyce Breger, Dr. Sebastian Diaz, Ajmeeta Sangtani, Dr. Okhil Nag, Dr. Scott Walper and Dr. Kelly Burns for always being there to help with tricky experiments, recalcitrant graphing programs and proof-reading my writing. I would especially like to thank Dr. Kimihiro Susumu for always being willing to make fresh quantum dots whenever I needed them (which was often).

Finally I would like to thank all of my friends, especially Dr. Amy Lee, Dr. Molly Hyer, Poonam Sharma, Deepali Clare Sengupta and Kelly Snead for always being there to listen when research wasn't going how I hoped- you all have kept me (relatively) sane over these last 5 years!

TABLE OF CONTENTS

CHAPTER 1: Introduction	1
Intracellular Sensors	2
Nanoparticle Delivery Modalities	5
Passive Actuation.....	6
Responsive Actuation	9
Semiconductor Nanocrystal Quantum Dots	14
Förster Resonance Energy Transfer	20
Specific Aims	24
<i>Specific Aim 1: Understanding the effect of NP surface ligands and protein</i> <i>localization on intracellular assembly and FRET efficiency</i>	24
<i>Specific Aim 2: Design and implementation of a novel actuation method for cellular</i> <i>drug delivery</i>	25
<i>Specific Aim 3: Design and implementation of an extracellular pH sensor</i>	26
CHAPTER 2: Understanding the Effect of NP Surface Ligands and Protein	
Localization on Intracellular Assembly and FRET Efficiency	28
Introduction	28
Experimental	31
Materials	31
QD Synthesis and Capping Ligands	32
Cell Culture and Transfection.....	33
Microinjection.....	34
Microscopy and Image Analysis.....	34
Gel Electrophoresis.....	35
FRET Analysis.....	36
Results	37
Experimental Rational and Design	37
Efficacy of the FRET System	40
Intracellular QD-mCherry Assembly and FRET Efficiency	44
Discussion	47
CHAPTER 3: Design and Implementation of a Novel Actuation Method for Cellular	
Drug Delivery	51
Introduction	51
Experimental	53
Materials	53
Synthesis of QDs and β -cyclodextrin (β CD) Conjugation	53
Maltose Binding Protein Synthesis.....	54
Gel Electrophoresis.....	56
Preparation of QD-MBP- β CD Conjugates	56
Analysis of QD-MBP- β CD Conjugate Responsiveness	57
Cellular Culture and Plating	58
Microinjection.....	59
Maltose Delivery.....	59
Image Acquisition and Analysis	60

Fluorescence Lifetime Imaging Measurement (FLIM)	61
Results and Discussion.....	62
Design and Rationale of Theranostic NP Actuation	62
Characterization of FRET Efficiency of QD-MBP- β CD Conjugates	66
Determination of Actuation Efficiency of QD-MBP- β CD Conjugates by Plate- based Assay.....	68
Intracellular Actuation of the QD-MBP- β CD Conjugate System	70
Conclusions.....	78
CHAPTER 4: Design and Implementation of an Extracellular pH Sensor	79
Introduction.....	79
Current pH Sensors	80
JB858: A Unique Membrane-Labeling Peptide	82
Experimental	84
QD-FITC Coupling and pH Sensing Assay.....	84
Cell Culture and Cytotoxicity Test	85
QD-FITC Delivery to Cellular Membranes Using Peptide JB858.....	86
Acquisition and Image Analysis of Extracellular pH Sensing	86
Results and Discussions	87
Ligand Exchange to Produce Biocompatible Blue-Emitting QDs	87
Ratiometric pH Sensing Assay	90
Conclusions.....	98
CHAPTER 5: Conclusions.....	100
Conclusions Overview	100
Future Directions	106
APPENDIX.....	111
REFERENCES:	113

TABLE OF FIGURES

Figure 1: Types of NP actuation	5
Figure 2: QD schematic and size-dependent emission	14
Figure 3: Schematic of QD-FRET construct for Specific Aim 1	24
Figure 4: Schematic of FRET-based Actuation Modality for Specific Aim 2	26
Figure 5: Schematic and Spectral Sensitivity for the FRET-based pH Sensor.....	27
Figure 6: Fluorescent materials and FRET rationale used in this study.	37
Figure 7: Assembly and FRET analysis of the QD-mCherry donor-acceptor pair	40
Figure 8: Cytosolic assembly of QDs and mCherry.	44
Figure 9: Assembly of QDs and mCherry at the cytofacial leaflet of the plasma membrane.....	46
Figure 10: Design of QD-MBP- β CD-dye- and -drug conjugate systems.....	63
Figure 11: FRET analysis of the QD-TF3 and QD-DOX donor-acceptor pairs.....	66
Figure 12: Responsiveness of QD-MBP- β CD-TF3/DOX systems to the addition of maltose.	69
Figure 13: Response of intracellular QD-MBP- β CD-TF3 to maltose addition.....	72
Figure 14: Time-resolved response of intracellular QD-MBP- β CD-TF3 to addition of extracellular maltose.	73
Figure 15: Response of intracellular QD-MBP- β CD-DOX to maltose addition.....	76
Figure 16: Time-resolved response of intracellular QD-MBP- β CD-DOX to addition of extracellular maltose.	77
Figure 17: 464 nm QD- FITC FRET construct analysis.....	93
Figure 18: 464 nm QD-FITC Sensor Efficacy.....	96
Figure 19: Unknown pH Analysis.	97

TABLE OF APPENDIX FIGURES

Figure A 1: Schematic of synthesized β CD-DOX.....	111
Figure A 2: Representative images and data from FRET bleaching experiments.....	111
Figure A 3: Rate equation used for maltose delivery analysis.	112
Figure A 4: Representative image and data from FLIM analysis.....	112
Figure A 5: β CD-DOX and free DOX delivery comparison.	112

Chapter 1: Introduction

Theranostics, or the combination of a therapeutic and diagnostic capabilities within the same agent, is a burgeoning field of research with numerous potential applications as it can combine delivery of medicinal agents with the ability to image the localization of the agent *in vivo*³. Overcoming the limitations of systemic drug delivery, which include the necessity for high doses and the potential for serious secondary side effects, is at the forefront of the design and implementation of theranostic agents. Ideally, a well-designed theranostic agent will be targeted, controllable and multifunctional to achieve the best therapy possible. Several characteristics are desired from such a system *in vivo*: 1) a large accumulation of the delivered theranostic agent in the targeted location such as a tumor site, 2) the potential for the material to be delivered with precision to a specified intracellular location and overcome intracellular delivery barriers, 3) minimal toxicity caused by the carrier itself, 4) controllable release of material in response to either an external stimuli or based on the location's environment and 5) be visualizable for real-time monitoring of delivery and treatment⁴. Theranostic treatments are most desired for use as chemotherapeutic agents, which traditionally requires biopsy of cancerous tissue to evaluate status and therapeutic response, which can take hours or even days to thoroughly analyze⁵. Therefore, the most effective treatment combines a therapeutic and diagnostic agent allowing doctors to better monitor every aspect of treatment, from drug release kinetics, efficacy, and localization over time. In order to successfully design new and effective theranostic materials, one needs a thorough understanding of the carrier ensemble, the interactions within the construct components, and the surrounding area.

Intracellular Sensors

Inherent in a theranostic system is the ability to visualize either the location or, even more specifically, a reaction or process that occurs at the target location. Design of these sensing modalities relies on the visualization of first, the system itself and second, a change caused by an interaction or cellular process. These types of sensors usually rely on fluorescent molecules as the reporting agents, and these can be organic molecules like fluorescein isothiocyanate (FITC) or proteins like green fluorescent protein (GFP). For example, FITC is widely used for its responsiveness to the pH of the local environment, due to its pK_a of 6.4, which causes changes in the absorption and emission over the pH range of 5 to 9. Chen *et al.* capitalized on this property to design a ratiometric pH sensor for studying mitochondrial pH⁶. They conjugated FITC to a non-pH sensitive hemicyanine group that acted as both an internal control and a mitochondrial targeting agent as it has a lipophilic cationic nature. The sensor showed good localization to the mitochondria of MCF-7 cells and produced a visualizable dynamic range between pH 6.5 and pH 8.5. This is just one example of the ways research groups are attempting to study intracellular pH, be that in mitochondria or, more commonly, lysosomal pH change⁷⁻⁹. Later in this dissertation we will discuss the lack of current research focusing on extracellular pH sensing and our attempt to expand the current field in this regard.

Comparable to FITC's inherent responsiveness to pH, fluorescent proteins can be genetically engineered to be sensitive to and report on intracellular processes. Toward this end, the Hisabouri Group modified a cyan version of GFP, mTurquoise (480 nm emission), and a farther blue emitting protein Sirius (425 nm) to respond to a redox environment through a lowering of the protein's quantum yield (QY). Dubbed oxidation

balance sensed quenching proteins (Oba-Q), they saw a 50% reduction in QY for the mTurquoise protein and an almost 70% reduction in the QY of Sirius after addition of the oxidizing agent diamide to protein-expressing HeLaS3 cells. They also saw a recovery of fluorescence after 30 minutes, producing a multi-use sensor ¹⁰. In addition to sensing an environmental change, these systems can be designed to report the presence of a target. One such system uses two molecular beacons, which are single-stranded stem-loop DNA probes usually conjugated to fluorescent molecules, to look for a mutation in the K-ras gene common in cancerous cells ¹¹. To more efficiently tether the fluorescent probe (either cyan fluorescent protein (CFP) or yellow fluorescent protein (YFP)) to each specific beacon, Blackstock and Chen used the HaloTag® labeling system where a modified haloalkane dehalogenase is specifically designed to covalently bind to a suicide chlorohexane (CH) ligand. When both of the molecular probes are bound to the mutated DNA sequence, the cells expressing the genes can be subsequently imaged ¹². In order to achieve intracellular delivery of this construct the HIV-derived internalization peptide, TAT, was employed to ensure their sensor entered the cells sufficiently to label the desired DNA sequence, adding another level of complexity to their system.

While the aforementioned systems certainly contributed to the development of intracellular sensors, many of these modalities are limited by their ability to introduce a sensor to a desired cellular location and the inherent limitations of many commonly used fluorescent molecules. More specifically, these fluorescent molecules are highly susceptible to photobleaching, chemical and physical degradation, broad overlapping absorption and emission profiles, and have low QYs ¹³. Consequently, these limitations represent an area that requires far more research and development. Nevertheless, using

these and similar sensing mechanisms within a theranostic agent can provide multiple levels of information about the interaction of the agent within the body and about the potential efficacy of the agent as a therapeutic.

Combining a theranostic agent with a sensing modality is intrinsically complicated and has continuously relied on one type of primary scaffold to engineer these constructs: nanoparticles (NP) ¹⁴⁻¹⁵. NPs are extremely small, ranging in size from a few nanometers to less than 100 nm in diameter ¹⁶. This size means that they are similar in scale to proteins but smaller than cells themselves, allowing for intracellular targeting potential. Additionally, they have many qualities that make them ideal scaffolds for complex theranostic agents. These include their large surface-area-to-volume ratio, their ability to circulate throughout the body and potentially clear through the renal system and, more importantly, the possibility for bioconjugation to targeting proteins or peptides ¹⁷⁻¹⁸. Finally, they can facilitate delivery of the therapeutic component of a theranostic agent by being 'loadable' with a desired drug cargo. As NPs fall broadly into two categories, 'soft' and 'hard', loading can be either within the NP itself as with soft NPs (liposomes, polymersomes, or mesoporous silica NPs), or conjugated to the particle surface either with soft NPs or hard NPs (iron oxide NPs, quantum dots, upconversion NPs) ¹⁹⁻²⁰. Release of the cargo from the NP once the theranostic agent has been delivered to the desired location is the final and critical component to designing these systems, and can be performed in a variety of methods that are delineated in the following section.

Nanoparticle Delivery Modalities

Delivery of NP cargo can be broadly defined as occurring by one of two actuation modalities. The first is passive actuation, which requires no external stimulus but relies on the passive efflux of the cargo, either from within the NP core (as from soft or porous NPs) or from the NP surface of all NP types. The second method is an active stimulation

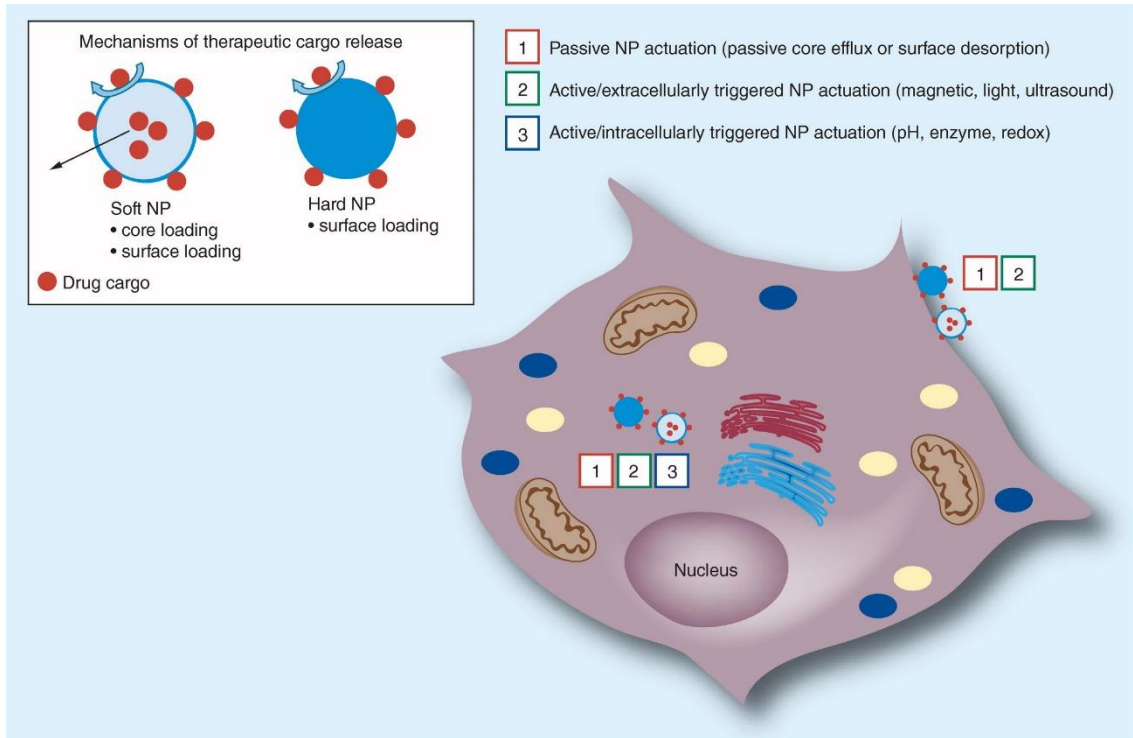


Figure 1: Types of NP actuation. NP-associated cargos can be actuated or released by three general mechanisms: passive, active/extracellularly-triggered or active/intracellularly-triggered. (*Inset*) NP drug cargo release mechanisms. Drug cargos are released from soft and hard NPs in various ways. Soft NPs can be loaded in the NP core or on the surface while hard NPs are primarily loaded on their surface. Drug cargo release is indicated with arrows. (*Main*) Spatiotemporal control of NP actuation. Both soft and hard NPs are subject to actuation by all three modalities. The primary difference is the location of the triggering mechanism as indicated with the numbered boxes. Figure reproduced with permission from ².

of release that can be achieved either in response to a change in the NP environment (*e.g.* pH change ²¹, enzymatic cleavage ²², or redox ²³) or to an external application of a power source (*e.g.* magnetism ²⁴, light ²⁵⁻²⁶, or ultrasound ²⁷). These mechanisms provide a

range of temporal control over release, where passive actuation occurs regardless of environment and therefore produces the least control. Active triggering utilizing an external stimulus inherently provides a high degree of temporal and spatial control over cargo release; while actuation caused by intracellular changes can be highly specific to the intracellular localization of the theranostic agent, and so also affords control over spatial and temporal release. Such actuation modalities will now be discussed individually to more clearly define the pros and cons of each method.

Passive Actuation

Passive actuation is a simple and elegant method for incorporation of a delivery element to a NP complex, and is uncomplicated in design as it only requires the cargo to be contained within or absorbed onto the NP surface. Hard NPs typically have only the surface area available as space for cargo loading, and rely on transient interactions. One of the more popular types of hard nanoparticulate materials are gold NPs (AuNPs), as they can be synthesized in a large range of particle sizes²⁸ and can be made biocompatible and inert through the use of a variety of capping ligands²⁹. Gold is also on the FDA's 'generally recognized as safe' or GRAS list³⁰. Additionally, they can be visualized either with fluorescence if the particle is small enough³¹ or using methods like X-ray 'computed tomography' (CT) scanning³². Conjugation of these particles with low molecular weight drugs has been clearly shown to increase the efficacy of the therapy over that of the freely delivered agent, verifying this approach³³⁻³⁵. Doxorubicin (DOX), an anthracycline antitumor drug, is a widely studied small molecule that intercalates in the DNA backbone and is most commonly used as a chemotherapeutic³⁶. Assembling

DOX onto the surface of AuNPs has been studied by many groups and even simplified to a self-assembly method that utilizes heavy metal binding proteins (HMBPs) as shown by the Park Lab³³. Reduction of the gold ions within the NP surface was accomplished using recombinantly-expressed HMBPs (metallothionein and phytochelatin) and produced minimally toxic AuNP-HMBPs that could be incubated with DOX and caused a subsequent 30% increase in the efficacy of the DOX as compared to freely delivered DOX when tested in HeLa cells. In addition to simply allowing for accumulation due to increased circulation times, targeting moieties can be appended to the NP surface. One such targeting molecule is folic acid (FA), which the Huang Group conjugated onto the surface of graphene quantum dots (QDs) that had DOX absorbed onto the QD surface. Addition of FA provided specific delivery of the QDs by targeting the commonly over-expressed folate membrane receptor in cancerous cells and facilitated increased endocytosis and long-term DOX delivery. When analyzing the effect of FA on internalization and DOX delivery, the addition of FA increased delivery and subsequent cytotoxicity by 40 percent preferentially to the cancerous HeLa cells compared to the non-cancerous cell lines (A549 and HEK293A)³⁷.

In comparison, soft NPs can incorporate the cargo within the particle itself, and the release is mainly driven by a concentration gradient of internal vs external cargo concentrations. One type of soft NP currently studied can be created from proteins themselves, producing what is called a protein nanocage. The Prosperi Group used DOX loaded apoferritin nanocages - a protein that interacts with ferritin receptors that are also overexpressed on cancerous cell membranes. These protein-DOX complexes internalized much more rapidly than free DOX, allowed for increased nuclear accumulation of DOX

and subsequently caused higher rates of cellular apoptosis in HeLa cells ³⁸. Other biological components can also be used for soft NP construction - namely lipids, which make up the bilayer plasma membrane. Functionalized liposomes were produced by Ding *et al.* containing the drug methotrexate (MTX), with a targeting peptide chosen to facilitate delivery of the liposomes to CD-40 positive cells. These cells are a cause of autoimmune dysfunction and so the group studied the effect of the delivered liposomes on the number of CD-40+ cells in autoimmune encephalomyelitis (EAE) mice, showing significant improvement in their clinical scores over 18 days ³⁹. Soft NPs are not required to be made of biological agents as was shown by our lab in work using liquid crystal NPs (LCNPs). These particles were decorated with transferrin to increase their internalization and the high photostability of the embedded pyrene fluorophore afforded photostable imaging not achievable with AlexaFluor-transferrin conjugates. Importantly, the particles demonstrated an increase in DOX delivery efficacy by ~40 percent as the LCNPs could carry DOX within the NP core, and shows promise for the delivery of other hydrophobic drug molecules ⁴⁰.

These systems rely on the ability for the NP-drug carrier to remain circulating for a longer period of time compared to systemically delivered drugs ⁴¹⁻⁴² or for accumulation of the delivery system due to functionalization with targeting elements, subsequently permitting for administration of lower doses ⁴³⁻⁴⁴. These types of delivery systems are currently the only FDA approved NP-drug systems, with the first being a liposomal formulation of DOX, called Doxil ⁴⁵, and most current NP treatments utilizing this concept of a small-molecule drug encapsulated in a protective coat like a liposome, or complexed with a polymer or a protein (like albumin) ⁴⁶. Better methods of targeted

release could further reduce the systemic side effects compared to these passive delivery systems.

Responsive Actuation

Compared to passive actuation, responsive actuation requires an external stimulus to trigger the release of the cargo. This can be further broken-down into two types of stimulation: internally-triggered or externally-triggered. Internally triggered actuation relies on a specific change in the environment around the NP carrier caused by the localization of the carrier within various compartments of the cell. One of the most commonly utilized changes is that which occurs in the endo-lysosomal pathway. As vesicles are shuttled through this pathway, the pH in the vesicles lowers from a physiological 7.4 to a final pH of around 5 in the lysosomes⁴⁷. Acid-responsive NP constructs can be produced from soft polymeric NPs that will degrade in the lysosomal environment or hard NP that have acid-labile linkages between the NP surface and the cargo. One pH-responsive polymer commonly used in this approach is Poly(2-(diisopropylamino) ethyl methacrylate (PDPA), which can be formed into carriers *via* a layer-by-layer technique⁴⁸. Using this method, the Dong Group increased the circulation time of PDPA particles by functionalization with zwitterionic polycarboxybetaine (PCB) methacrylate, targeted them with the use of an appended arginylglycylaspartic acid (RGD) peptide, and loaded with a therapeutic cargo (DOX). The addition of the targeting RGD peptide increased internalization and efficacy of the NPs in HepG2 and HeLa cells and the addition of the PCB produced prolonged circulation and tumor accumulation in HepG2 tumor-bearing nude mice⁴⁹. The use of

acid-labile linkages like hydrazone bonds has also shown to be efficacious, with Zolata *et al.* appending Trastuzumab-DOX to the surface of superparamagnetic iron oxide NPs (SPIONS) and showing the ability to image the construct using magnetic resonance imaging (MRI) in addition to tumor targeting in HER2 + breast tumor bearing BALB/c mice and subsequent DOX release after particle internalization ⁵⁰. An alternate internal cellular environment that can be exploited is the redox potential within the cytosol, commonly achieved through the use of disulfide linkages. Glutathione is present in the cytosol at around 10 mM ⁵¹ and will normally reduce any available thiol-linkages. One very recent study performed by the Hu Lab uses this reactivity to produce responsive mesoporous silica NPs (MSNPs) that are loaded with DOX and capped with thiol-linked transferrin (Tf) to ensure the DOX encapsulation. The Tf both targets and subsequently causes release after the linker is reduced intracellularly in Huh7 cells, and the efficacy of the delivery system was reduced with the addition of free Tf that competitively internalized, resulting in hindered DOX release ⁵². In lieu of a response to an environmental change, the presence of intrinsically expressed enzymes can also actuate release. Tumor cells have a higher number of matrix metalloprotease (MMP) enzymes to facilitate tumor metastasis. MMPs allow for migration of malignant cells as they cleave extracellular matrix proteins, allowing cells to move more freely in their environment. Using MSNPs, the Cai Group targeted DOX to HepG2 cells *in vitro* and to tumor-sites in a murine model *in vivo*. Specifically, they capped the MSNPs with a cell penetrating peptide, a passivating human serum albumin to increase circulation and MMP-2 cleavable DOX, the combination of which produced an efficacious therapeutic when delivered to HepG2-tumor bearing nude mice ⁵³. The combinatorial effect of the

multifunctional NP system produced a high degree of tumor-specific toxicity with minimal side effects on normal organs. All of these methods for actuation necessitate the internalization to a specific final location for the delivered theranostic system. However, this usually requires the addition of secondary targeting molecules like Tf or RGD peptides, and consequently reduces the loading capacity of the NP carrier.

Externally-triggered actuation often relies on the application of an external power source, allowing for more cargo loading potential. One commonly used method, magnetically-driven actuation, can provide both targeting and actuation upon localization. These systems function due to the use of metal oxide NPs (MNP) as the active scaffold, producing a theranostic agent *via* Magnetic Resonance Imaging (MRI) ⁵⁴. ⁵⁵. The common small molecule drug, DOX, was again used in a supramolecular, multicomponent MNP. PEI-linked β -cyclodextrin (β CD) coated the MNP surface and allowed for the β CD to self-assemble with a polycyclic hydrocarbon adamantine (Ad) grafted onto polyamidoamine dendrimers producing complex nanocarriers through a host-guest interaction and caging DOX molecules within the NP structure ⁵⁶. Once localized, the MNPs were heated using an alternating magnetic field releasing DOX from the β CD. This system reduced the quantity of delivered agent required to 1/1000th of that required for free DOX in a murine tumor xenograft model.

Magnetic stimulation necessitates the use of a magnetically-responsive element within the NP design, whereas light-triggered actuation does not have such requirements. Light can facilitate multiple reactions within the stimulated area, including localized heating around the NP construct, the generation of reactive oxygen species (ROS), the initiation of molecular isomerization and the breaking of chemical bonds. Photo-labile

linkers (quinolone, coumarin, o-nitrobenzyl) can be incorporated into delivery systems and stimulated using UV light to trigger release *via* cleavage. O-nitrobenzyl was used by Hu *et al.* within FA- functionalized micelles carrying the camptothecin (CPT) prodrug⁵⁷. The micelles were crosslinked using pH-reductive acylhydrazone and disulfide bonds, which require acidic and reductive environments to further stimulate release after initiation with UV light. UV light, however, is a high energy light source that has limited tissue penetration in addition to causing unwanted DNA damage to surrounding tissue⁵⁸. To overcome some of these limitations, a lower-energy near infrared light (NIR) source has been utilized, which can be absorbed by both AuNPs and organic polymers. One interesting application used single-wall carbon nanotubes (CNTs) that were functionalized with chitosan and loaded into a thermally and pH responsive nanogel⁵⁹. DOX was integrated into the system through a π - π stacking with the incorporated chitosan backbone, and on-demand release was facilitated by CNT heating due to excitation with NIR (808 nm) wavelengths. These carriers significantly increased cytotoxicity in HeLa cells when subjected to NIR irradiation compared to particles without irradiation and free DOX. Finally, ultrasound has also proven to be an effective extracellular trigger, as it has a greater penetration depth than either light or magnetic targeting and, additionally, can exert physical effects on the tissue in addition to the theranostic agent. These including pressure variations (push and stress), acoustic fluid streaming, cavitation and local hyperthermia⁶⁰. Liposomes loaded with both calcein and DOX were used by the Shimizu Group, and were functionalized first with aptamers (single stranded DNA) chosen to target platelet-derived growth factor receptors present on breast cancer cells and second with a poly(NIPMAM-co-NIPAM) as a

thermosensitive polymer. They showed selective targeting of the breast cancer cell line MDA-MB-231 and ultrasound-triggered release and subsequent cell death with confirmation of release shown by the fluorescence of the calcein ⁶¹. All of these externally-triggered actuation modalities require for the targeted delivery location to be known to reduce secondary effects due to the power source. This can potentially be an issue in cases like metastasis, where the known tumor location is not the only place cancerous cells are present and would be missed with this type of treatment.

One currently under-explored method of actuation is that of an active extracellular trigger that does not rely on an external application of power. If release of the cargo could be caused by the addition of a secondary and inert molecule, a nutrient for instance, then release would happen regardless of the construct location either within the body or a specific cellular site. One major focus of this dissertation is the design and implementation of an actuation modality that accomplishes just this task that is described thoroughly in Chapter 4. As a prototypical NP scaffold, all research described herein was performed using semiconductor nanocrystals, which are ideal for biological research and sensing methods as described in the following section.

Semiconductor Nanocrystal Quantum Dots

Semiconductor nanocrystals, or quantum dots (QDs), have unique optical and electrical properties due entirely to their extremely small (a few nanometers) size. Colloidal versions were first synthesized by Louis Brus in the 1980s⁶², these particles are so small that their radii are within the Bohr radius for their composite material and so

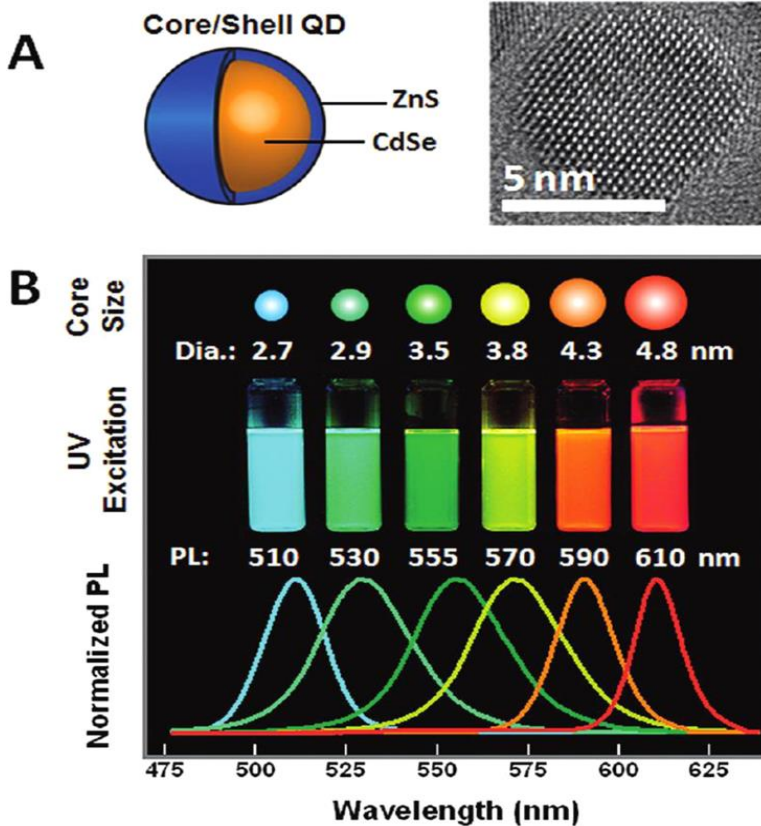


Figure 2. (A) Schematic and TEM image of a CdSe/ZnS QD. (B) Schematic, photograph, and PL emission spectra illustrating progressive color changes of CdSe/ZnS with increasing nanocrystal size. Adapted with permission from¹.

produce some very interesting optical properties as they display discrete energy levels as a single atom would despite being composed of hundreds of atoms. This quantum confinement produces a spatial enclosure for the electronic charge carriers within the nanocrystal structure, and the minimal band gap becomes a varied quantity that is dependent on the size of the nanocrystal structure. They are commonly synthesized from a binary combination of elements, from either group III to V or II to VI on the periodic table of elements and are crystalline in

nature. One of the most common combinations of these elements is the combination of Cd (group II) and Se (group VI) to produce a CdSe core QDs using organometallic methods of synthesis⁶³⁻⁶⁵. To improve stability and increase the QYs of these nanoparticles, they are often coated with a material that has a higher bandgap than the core material. When not protected by the outer shell, the inorganic semiconductor is prone to reorganizations of atomic positions within the crystalline structure, causing formations of electron traps or 'holes' that cause a reduction in the optical properties of the material itself. Using a capping material with a higher bandgap essentially confines the electrons within the cluster by removing the potential for structural reconstructions. In the case of CdSe cores, a shell of ZnS is used as it absorbs at a shorter wavelength than CdSe and also will protect it from oxidative degradation, increases the biocompatibility of the nanoparticles and passivates the core surface (Figure 2A)^{13,63}. As the size of these QDs is reduced a visualizable 'blue shift' in emission occurs by physically controlling the energy levels (Figure 2B)⁶⁴. Specifically, the CdSe core QDs can be tuned from a range of deep red emission to green emission by changing the core size from ~ 200 Å to 20 Å, respectively, which is an ideal range for imaging in biological samples. QDs, regardless of size, absorb more readily at higher energies (the UV range of wavelengths) and over a broad area, which is atypical for commonly used fluorophores⁶⁶. Despite their similar absorption spectra, the emission spectra are tunable, narrow and highly symmetric. Additionally, they have relatively long excited state lifetimes (10-30 ns) which is in marked contrast to most fluorescent molecules that have shorter lifetimes (<4 ns⁶⁷) and broad, red-tailed emission profiles⁶⁸. QDs have high quantum yields of around ~20% when in an aqueous environment, which is higher than many of the commonly used

fluorophores as previously mentioned in the sensing section ⁶⁹. The optical properties of QDs have other benefits in many areas where fluorescent molecules have limitations for biological applications. QDs display the aforementioned marked 'effective' Stokes shift, a red-shift of emission spectra with respect to absorption spectra, have greater resistance to physical and chemical degradation compared to organic or biological fluorophores ⁷⁰, and have a large two-photon cross section which provides the ability to use smaller energy wavelengths for excitation deeper in tissue samples. One of the paramount properties of QDs is their resistance to photobleaching, which allows for longer-term visualization of real-time intracellular process that would not be possible for fluorescent probes like FITC or GFP ^{13, 71}.

While ideal optically, there are some limitations for the use of QDs in biological samples. First and foremost, they need to be stabilized as a colloid for use in aqueous environments as they are synthesized in organic solvents and commonly have tri-octylphosphine/tri-octylphosphine oxide (TOP/TOPO) ligands on their surface after synthesis. There are a range of potential stabilization methods that could be used for QD biological applications, including the use of amphiphilic polymers, lipids or silica coatings which usually increase the overall size of the QDs dramatically, and therefore limiting the intracellular application potential⁷². Alternatively, the native TOP/TOPO ligands can be exchanged for more hydrophilic ligands, producing much smaller and colloidally stable QDs. One of the seminal papers written by Chan and Nie utilized mercaptoacetic acid to both produce stabilized QDs and conjugate proteins to the QD surface⁷³. The mercapto group bound to the zinc present in the ZnS shell of the QDs and the hydrophilic carboxylic acid produced soluble QDs and could be reacted *via* EDC chemistry with

amine groups to covalently couple proteins to the QD surface. They showed that the addition of transferrin produced internalized clusters of QDs in response to receptor-mediated endocytosis. After this initial success, numerous other groups started investigating a wide range of new capping ligands. The Bawendi group specifically examined QDs capped with a small capping ligand dihydrolipoic acid (DHLA), where they saw little success using EDC reaction chemistry for protein labeling and so designed a new self-assembly method to coordinate maltose binding protein (MBP) to the QD surface⁷⁴. To facilitate this interaction, they inserted a positively charged leucine zipper that would associate with the alkyl-COOH capping ligand and produced a much simpler method of bioconjugation for QD applications. Numerous capping ligands have been subsequently produced that range from small capping ligands that allow for greater access to the QD surface but also can cause aggregation in complex biological environments to larger, more biocompatible, capping ligands which can contain long poly(ethylene glycol) (PEG) chains that increase the hydrodynamic radius of the QD and can make protein coordination more difficult⁷⁵⁻⁷⁶. One very widely used method of bioconjugation was developed based off of the chelation of metal ions by multi-histidine tags originally used for protein purification through immobilized metal affinity chromatography (IMAC). Proteins engineered to contain His-tags can be associated to the QD surface either through the addition of a nitrilotriacetic acid (NTA) into the QD capping ligand and assembling with nickel added to the solution or, more simply, by allowing the histidine tag to associate with the zinc in the QD protective shell^{1, 77-78}. While this area of research has grown dramatically, further study of the effect these various capping ligands have on the implementation of QDs in sensing modalities is

required. In Chapter 2 this dissertation examines a range of these capping ligands and their effect on intracellular assembly to attempt to increase the potential applications for future theranostic research.

One final concern for biological applications for QDs is that some of the metals that make up the most commonly used QDs are toxic (cadmium and lead) and will likely never be approved for clinical applications in human subjects, but this does not detract from their power as a research tool. There are QD types that use alternate core compositions including: ZnO⁷⁹, ZnSe:Mn/ZnO⁸⁰, InP/ZnS⁸¹. A recent related study performed by the Prasad Group on rhesus macaques used lipid-micelle-encapsulated cadmium-based QDs intravenously injected and monitored the animals response to the injection over 3 months⁸². They saw no detrimental effects from the cadmium QD delivery, which is very likely due to the passive nature of the micelle coating on the QD surface which could have promoted clearance of the QDs from the body. A 2016 meta-analysis performed by members in our lab analyzed over 307 publications containing over 1700 sample data points, each with 24 descriptions, and determined that QD toxicity was dependent on their surface properties, the size of the QDs delivered, and the exposure time to the QD sample⁸³. Biological applications of QDs must clearly take these factors into account during the design of any potential research system.

QDs have been used for many studies on the efficacy of NP delivery platforms as their optical properties allow for easy monitoring after delivery. Chen *et al.* used glutathione (GSH)-coated CdTe QDs that were conjugated to DOX through a condensation reaction and further decorated with FA-terminated PEG to specifically target HeLa cells⁸⁴. The PEG coating availed minimal nonspecific binding while the FA

moiety facilitated localization of the particles and subsequent increased intracellular accumulation of the QD-drug conjugates. The photophysical properties of QDs also mean that they make ideal Förster Resonance Energy Transfer (FRET) donors (a more detailed discussion of the characteristics of FRET itself will follow after this section)⁸⁵⁻⁸⁶. Using QDs as a biosensor can be accomplished by conjugating them to proteins with an attached fluorophore and incorporating certain biological interactions, which can modify the distance between the QD and protein and therefore modify the FRET between them⁷⁸. FRET-based QD systems have been used in various applications, including work performed by the Bao Group using QDs coupled to pH sensitive fluorescent proteins to monitor intracellular pH and determine if modifications to the fluorescent protein, mOrange, could allow for a more sensitive system⁸⁷. In another study, Shaheen *et al.* used plasmid DNA (pDNA) coated QDs as a FRET donor and rhodamine-labeled cations as a FRET acceptor to visualize condensation of pDNA within the nucleus to determine an effective cationic carrier for increased transfection efficiency⁸⁸. These systems show the versatility of using QDs as a scaffold for a FRET sensing construct, but more information is required to fully understand the tools needed to optimize a QD-based FRET sensor for biological applications. One major goal in current nanobiotechnology research is control over the location of delivered NPs, be that intracellularly or to a specific site within the body. As such, a system that could both deliver a therapeutic while simultaneously imaging and sensing could help overcome some current therapeutic limitations and provide a basis for designing better, next generation materials. Implementing such a system, however, requires both rational design and a practical understanding of the conditions under which such assemblies work.

Förster Resonance Energy Transfer

FRET is a mechanism of energy transfer that occurs between a donor (D) fluorophore in an excited state and a ground state acceptor (A) fluorophore *via* nonradiative dipole-dipole coupling⁶⁵. Due to the inverse 6th power dependency of FRET on donor-acceptor separation, close proximity, typically between 20-60Å, of the two fluorophores is a requirement for efficient transmission to occur. Additionally, an efficiently designed FRET pair should have a high degree of spectral overlap between the acceptor emission profile and donor absorbance profile. The following equation depicts the calculation used to determine the distance between the donor and acceptor where the efficiency of transfer would be 50%, also known as the Förster distance or R_0 for the donor-acceptor pair:

$$R_0 = 9.78 \times 10^3 [\kappa^2 n^{-4} Q_D J(\lambda)]^{1/6} \quad \text{Eq. 1}$$

This calculation takes into account the refractive index of the medium ($n = 1.33$), the dipole orientation ($\kappa^2 = 2/3$ for random orientation), the known quantum yield of the donor species (Q_D) and $J(\lambda)$, the spectral overlap function, which is calculated using the following equation:

$$J(\lambda) = \int F_D(\lambda) \varepsilon_A(\lambda) \lambda^4 d\lambda \quad \text{Eq. 2}$$

Where λ is the wavelength of the donor-acceptor spectral overlap, $F_D(\lambda)$ is the integrated donor emission normalized to unity, and $\varepsilon_A(\lambda)$ is the molar extinction coefficient for the

acceptor at the defined wavelength. The FRET pair chosen, therefore, must take into account these factors to produce a system sensitive over the desired physical distance.

Efficiency for a given system can be calculated by measuring the donors peak spectral intensity both in the presence of the acceptor and alone. These values can then be used in the following equation to determine the FRET efficiency for the donor-acceptor pair in their current state:

$$\text{FRET}_E = 1 - \frac{F_{DA}}{F_D} \quad \text{Eq. 3}$$

This is a useful equation as it means that efficiency and, therefore, the distance between the donor and acceptor can be determined by monitoring the fluorescent output from the donor alone. Once this value is known for the experimental system, the actual distance between the donor and acceptor in the current conformational shape can be calculated, which is very important given the aforementioned 6th power dependency of efficiency on distance¹³. Using the calculated FRET efficiency (E) and the calculated R_0 the following equation can be used:

$$E_n = \frac{n \left(\frac{R_0}{r_{DA}} \right)^6}{1 + n \left(\frac{R_0}{r_{DA}} \right)^6} \quad \text{Eq. 4}$$

In Eq. 4, ‘n’ refers to the number of acceptors per donor, and so the effect of increasing acceptors on efficiency can also be calculated for the donor-acceptor system. The calculated r_{DA} is defined as a center-to-center distance between the donor and acceptor for

the measured system, and so the distances calculated from these equations is not the distance of the acceptor from the surface of the donor, but from the center of the donor. To specifically calculate the r_{DA} the efficiency must be determined using Eq. 3, and then using the specific R_0 for the donor-acceptor pair and the number of acceptors per donor (n)- Eq 4 can be utilized to solve for the specific distance between the donor and acceptor at that point in time. Given that FRET is highly influenced by the distance between two fluorophores, it is a sensitive technique that can allow for investigation of many biological processes. These can include protein conformational changes⁸⁹, protein interactions⁹⁰, binding events and therefore kinetic rates for various enzymes and metabolic pathways⁹¹⁻⁹².

The benefit of using QDs as FRET donors are numerous. Specifically, their highly tunable emission profiles mean that they can be optimized for a desired acceptor molecule, and their excitation far in the UV reduces acceptor direct excitation that can influence efficiency calculations. Their large QY's mean that the effective R_0 , or the distance where FRET efficiency is 50%, for the donor-acceptor pair will be larger, and so the dynamic range of the designed FRET pair will be visualizable over longer distances. Moreover, the nanometer size range of the QDs allows for a large surface area-to-volume ratio and so numerous acceptors can be complexed to the QD surface, increasing the efficiency as shown by Eq. 4. The subsequent FRET efficiency can be 'tuned' for optimum cargo capacity and to produce a more sensitive intracellular sensor than a simple one donor - one acceptor system common when using fluorescent probes. Finally, it has also been shown that the use of QDs as the donor molecule in a sensing structure can improve the longevity of fluorescent molecules used as acceptors⁹³. This protection is

due to the fact that the excitation of the QD is far in the UV, which reduces direct excitation of the acceptor molecule in addition to the nonradiative nature of FRET, so the energy being absorbed by the acceptor molecule is significantly less than what would be required to visualize the acceptor directly. These benefits have been repeatedly confirmed in numerous experiments and studies ^{65, 85, 94}.

Specific Aims

This dissertation focuses on expanding our understanding of the NP components necessary to design an efficient cellular sensor and ultimately a theranostic platform, from the type of surface necessary for intracellular use to the efficacy of a new actuation modality. Using QDs as the NP platform for visualization, three NP based sensing functions were examined to increase the available tool-box for future specialized sensing functions.

Specific Aim 1: Understanding the effect of NP surface ligands and protein localization on intracellular assembly and FRET efficiency

The ability of an intracellularly-assembled FRET based construct is examined for dependence on the biocompatible capping ligand used on the QD surface and on the localization of the targeted protein with the cellular environment. To achieve this, a variety of capping ligands were synthesized to vary in size and charge and exchanged to populate the QD surface. These QDs were then microinjected into the cytosol of cells that

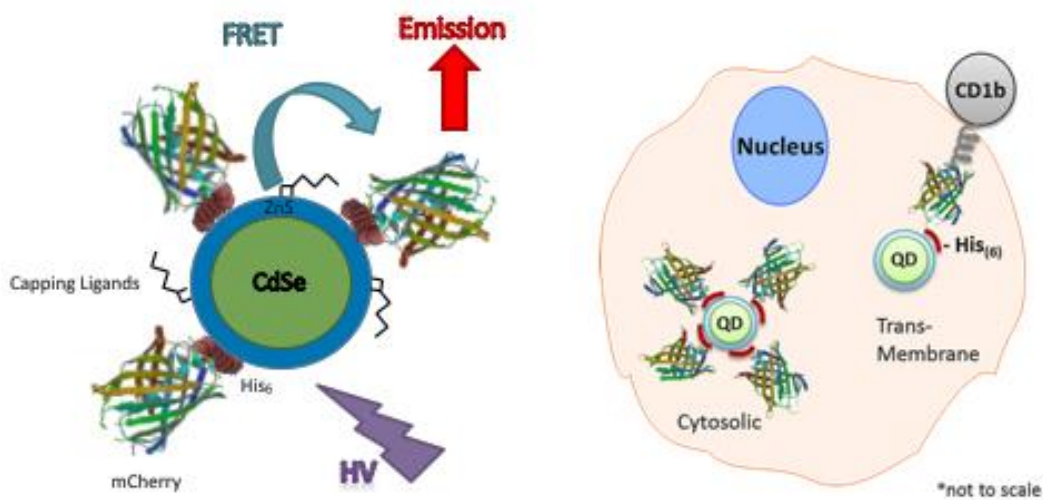


Figure 3: Schematic of QD-FRET construct for Specific Aim 1

were previously transfected to express a hexahistidine-tagged mCherry protein construct. The histidine tag allows for the mCherry to self-assemble to the QD surface *via* metal-affinity coordination. mCherry is an ideally suited FRET-acceptor for the 545 nm QD donor, as they have a high degree of spectral overlap and so a signal would only be produced when the protein is coordinated with the QD surface and highly proximal. To determine the effect of protein location on the coordination abilities of the injected QD and mCherry, a cytosolically expressed mCherry was compared to a trans-membrane bound mCherry protein (Figure 3). We expect that the capping ligand will affect the intracellular stability of the QDs themselves in addition to the efficiency of the assembled FRET construct, and that the location of the mCherry within the cell will also affect the efficiency of the construct with the more sterically hindered transmembrane-appended mCherry producing a lower FRET efficiency.

Specific Aim 2: Design and implementation of a novel actuation method for cellular drug delivery

The ability of an injected QD-based actuation system to respond to an external secondary signal and release cargo was studied. A novel actuation modality was produced to respond to an external delivery of an inert secondary nutrient molecule, maltose, and to report the release *via* change in the FRET signal visualized throughout the system. The system was analyzed for responsiveness over both time and maltose concentration, and for multiple types of cargo. A central scaffold of 520 nm emitting QDs was used and had the bacterial periplasmic transport protein, maltose binding protein (MBP), coordinated with the QD surface through the addition of a hexahistidine tag. β -

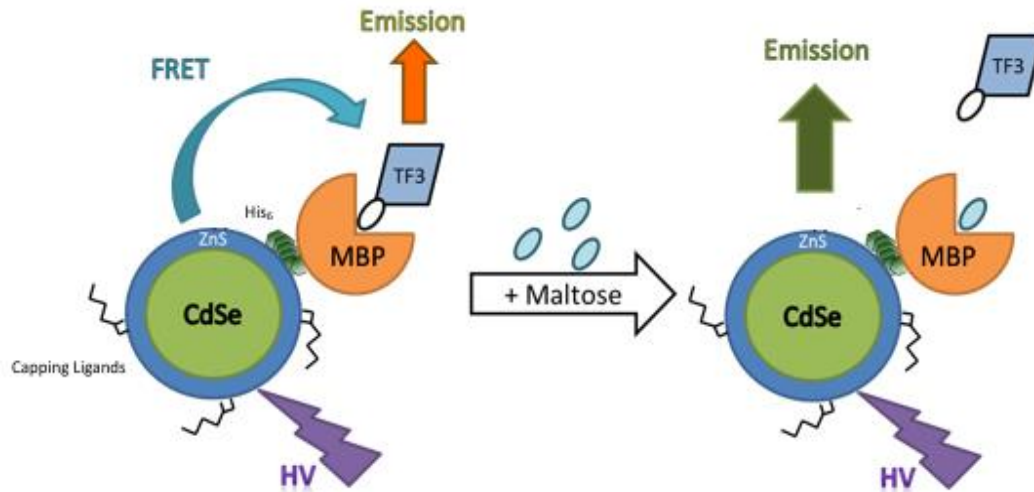


Figure 4: Schematic of FRET-based Actuation Modality for Specific Aim 2

cyclodextrin, a maltose analog, was conjugated to one of two cargos, allowing for them to be carried within the MBP's binding pocket (Figure 4). The cargos were chosen to specifically act as acceptors for the 520 QD to produce visual and quantifiable evidence of release. The Cy3 analog, TideFluor3 (TF3), was used as a standard acceptor molecule and the small molecule drug, DOX, was chosen as a drug analog. TF3 will produce a visualizable acceptor peak when within the MBP's binding pocket but as the DOX has a low molar extinction coefficient, the release of the DOX from the binding pocket will be measured by monitoring the QD PL peak height. We expect that the release of these cargos will be actuated by the addition of maltose and that this process will be affected by the time of incubation and the amount of maltose introduced into the cellular environment.

Specific Aim 3: Design and implementation of an extracellular pH sensor

Commonly used pH sensors focus on the intracellular environment, and disregard the direct extracellular environment. This area is of particular interest due to the change

that occurs in tumor microenvironments, where the pH lowers from a physiological level of ~ 7.4 to as low as 5⁹⁵. An extracellular pH-sensor was designed utilizing the pH responsive FITC fluorescent molecule as a FRET acceptor, and a new biologically-compatible blue-emitting (462 nm) QD that is an ideal FRET donor for FITC. (Figure 5). We anticipate that by avoiding direct excitation of the FITC, the extracellular pH will be able to be monitored by looking at the QD and FITC peak emissions. To append the sensor system onto the exofacial leaflet of the cells, a novel peptide JB858 was used. This peptide was previously found to robustly label the cellular membrane and to remain localized for up to 48 hours after delivery. Using this system, we analyzed the responsiveness of the QD-FITC pair to various extracellular pH's ranging from 3 to 8, both in the presence and absence of cells and then attempted to discern the pH of various 'unknown' buffers based on the sensor output. We hypothesize that the responsiveness of the system will be modified by the more complicated cellular environment but that the change will still be discerned over the system's dynamic range.

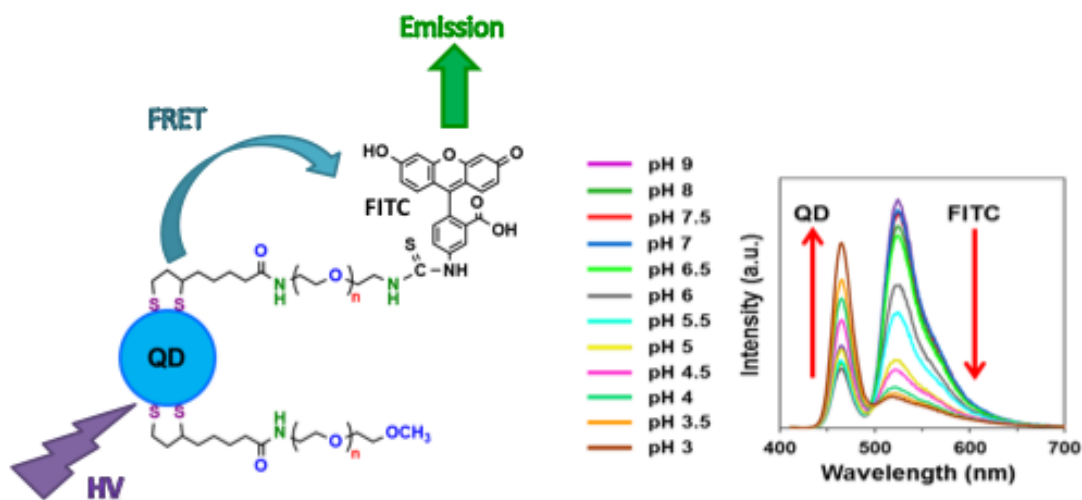


Figure 5: Schematic and Spectral Sensitivity for the FRET-based pH Sensor

Chapter 2: Understanding the Effect of NP Surface Ligands and Protein Localization on Intracellular Assembly and FRET Efficiency⁹⁶

Introduction

Increasing the efficacy of theranostic probes, those that can simultaneously sense/report on as well as treat a disease state, is currently a major focus of biomedical research⁹⁷⁻⁹⁸. In order to effectively design new and even more efficient theranostic materials, one needs a thorough understanding of the complex intracellular processes that are to be targeted. Historically, fluorescence-based approaches have been used to probe and monitor these processes, which necessitates efficient means of delivering/localizing the fluorophore to the targeted molecule of interest. Various approaches have been employed here and these have ranged from the cellular delivery of fluorophore conjugates directed to epitope tags expressed on targeted proteins to the recombinant expression of the fluorophore tag as a fusion to the protein of interest. Examples of the former include the metal-affinity-driven complexation of nitrilotriacetic acid (NTA)-dye conjugates to targeted proteins bearing cognate polyhistidine sequences⁹⁹⁻¹⁰⁰. Fessenden, for example, used a Cy3-NTA conjugate to probe a dual polyhistidine/green fluorescent protein (GFP)-tagged version of the Ca²⁺ release channel, ryanodine receptor type 1, as a means to probe membrane channel function¹⁰¹. Recombinant tagging of targeted proteins for sensing function has also been shown by Yip *et al.* who expressed the channel protein aquaporin as a fusion to the photoconvertible fluorescent protein (mEos2) for the visualization of protein trafficking in response to vasopressin¹⁰². Other approaches have

utilized the *in situ* assembly of the sensing construct. One example is the HaloTag system wherein a modified haloalkane dehalogenase is specifically designed to exogenously bind specified tags that can be linked *via* a chloroalkane linker to numerous target molecules. Los *et al.* utilized this system to study NF- κ B associated cellular processes ranging from DNA-protein complexes to protein translocation¹⁰³. Another example is the FLAsH/ReAsH system developed by Tsien's group which utilize biarsenical fluorophores that react with vicinal tetracysteine motifs expressed in target proteins¹⁰⁴. A still further example described by Lee *et al.* used a fluorescent molecular beacon reporter construct comprising a masking/quenching protein, a mitochondrial targeting sequence, a protease-specific cleavage sequence and a GFP reporter¹⁰⁵. This sensing construct reported on *both* the location and activity level of matrix metalloproteases in living cells.

Despite the demonstrated utility of the aforementioned sensing schemes, they all rely on the use of organic dye fluorophores or fluorescent proteins which can be limited by their inherent photophysical properties. Chief among these are their susceptibility to photobleaching, potential for chemical degradation, and their limited two photon action cross sections which can severely limit deep tissue *in vivo* imaging applications¹³. Luminescent semiconductor nanocrystals, or quantum dots (QDs), are nanoscale probes whose optical properties are ideal for the real-time, long-term monitoring of cellular processes. These attributes include high quantum yields, large 'effective' Stokes shift, and resistance to photobleaching and chemical degradation⁷⁰. Further, their broad absorption that extends into the UV coupled with their narrow, size-tunable emission peaks make them ideal donors for Förster resonance energy transfer (FRET)⁸⁵⁻⁸⁶. Finally, their large effective surface area-to-volume ratio makes them an ideal scaffold for the

assembly of biologicals around the central QD. To realize their full utility as the basis of intracellular FRET-based sensing (and ultimately in theranostics) one must not only develop a full understanding of how to control the FRET process in the sensing assembly but one must also be able to exert fine control over the intracellular location of the assembled FRET ensemble.

We have previously shown the ability to drive the intracellular assembly of a His₆-tagged form of the fluorescent protein mCherry to the Ni²⁺-loaded carboxyl termini on the polymer shell of a commercial QD preparation⁹³. Intracellular assembly of such FRET-based probes could reduce the complexity of the design and implementation of such structures. By having the cells themselves produce components, namely the acceptor protein, the location of the final complexes could be controlled without using other targeting moieties and, additionally, reactive moieties could be engineered into the protein structure and produced *via* the cells themselves. Using microinjection of QDs coupled with the transient expression of His₆-mCherry, our results showed the ability to assemble *in situ* a QD-fluorescent protein FRET-based assembly in the cytosol of COS-1 cells. The assembled complexes were stable intracellularly over a 6 h window and it was shown that the QD-sensitized mCherry exhibited an enhanced photostability when excited in a FRET configuration using the QD as donor compared to when the mCherry was excited directly. Despite these positive findings, numerous aspects of the FRET system are worthy of further interrogation in order to fully understand the potential utility of such a system for in real-time intracellular sensing. First, the use of a commercial, polymer-coated QD preparation in that initial experiment did not allow for strict control over the distance between the donor QD surface and the appended mCherry acceptor.

Second, control over the intracellular localization of the sensor system was not implemented, with the complexes only being assembled within the cytosol; any effects of intracellular assembly location on the FRET efficiency of the complex were not assessed. Here we build upon those initial studies and continue developing this intracellular assembly approach by performing a detailed examination of the role played by both the QD ligand coating and the assembly location of the QD-mCherry complex on the FRET efficiency of the system. Our working hypothesis in this study is that the nature of the QD ligand coating as well as the location of the FRET assembly can have a profound influence on the resulting FRET efficiency of the system. We make a comparative assessment of the FRET efficiency mediated by a suite of custom ligand molecules when appended to the surface of our in house-synthesized QDs and examine the effects of cytosolic *versus* membrane-directed assembly of the FRET complex. We discuss our results within the context of the considerations that one needs to be mindful of when designing a QD-fluorescent protein FRET ensemble to be used for real-time intracellular sensing.

Experimental

Materials

Bovine fibronectin, Anotop-10 filters (0.2 μm) and Dulbecco's phosphate buffered saline (DPBS, 137 mM NaCl, 10 mM phosphate, 3 mM KCl, pH 7.4) were purchased from Life Technologies (Carlsbad, CA). Nalgene syringe filters (0.2 μm) were purchased from Thermo Scientific. The plasmid encoding cytosolic mCherry utilized was previously described⁹³. The plasmid encoding mCherry on the cytofacial side of the

plasma membrane was generated by cloning the mCherry gene downstream of the extracellular and transmembrane domains of CD1b (CD1b-TMD)¹⁰⁶. The CD1b-TMD-mCherry-His₆ construct was synthesized (Genscript Corp., Piscataway, NJ) and cloned into the pcDNA3.1-myc-his(A) vector (Life Technologies) as a *KpnI-NotI* fragment and confirmed by sequencing. This construct resulted in the expression of a C-terminal His₆ motif to drive QD-mCherry assembly at the membrane. See Supplementary Information⁹⁶ (SI) for the complete nucleic acid and amino acid sequences. Recombinant mCherry-His₆ for QD assembly experiments outside cells was expressed and purified as described in ref⁹³.

QD Synthesis and Capping Ligands

Core-shell CdSe-ZnS QDs were synthesized to have an emission maxima centered at 545 nm and were made hydrophilic by exchange of the native hydrophobic trioctylphosphine/trioctylphosphine oxide (TOP/TOPO) ligands with polyethylene glycol (MW 750; PEG₇₅₀)-appended dihydrolipoic acid (DHLA-PEG₇₅₀-OMe) ligands terminated in methoxy groups as previously described⁶⁹. For comparison, QDs were also capped with either DHLA-PEG₆₀₀ terminated with nitrilotriacetic acid (DHLA-PEG₆₀₀-NTA) or with zwitterionic CL4 capping ligands¹⁰⁷. In a previous report, DHLA-PEG-NTA ligands were generated “on-QD” using carbodiimide chemistry after the initial cap exchange that removed the native hydrophobic ligands¹⁰⁸. In this study, the DHLA-PEG₆₀₀-NTA ligand was first synthesized “off-QD” and then used in the cap exchange procedure (see SI for ligand synthesis details⁹⁶). TEM analysis showed that QDs capped CL4 and DHLA-PEG₆₀₀-NTA had average diameters of 4.6 ± 0.4 nm and QDs capped

with DHLA-PEG₇₅₀-OMe had an average diameter of 4.7 ± 0.4 nm (see SI). TEM analysis was performed using Gatan Microscopy software to determine the size of at least 100 randomly selected QDs and averaged to determine the estimated size and polydispersity of the QD sizes¹⁰⁹.

Cell Culture and Transfection

African green monkey kidney (COS-1) cells were cultured in complete growth medium (Dulbecco's Modified Eagle's Medium (DMEM; American Type Culture Collection ATCC)) supplemented with 10% (v/v) heat inactivated fetal bovine serum (ATCC) and 1% (v/v) antibiotic/antimycotic (Sigma). Cultures were maintained in T25 flasks and incubated at 37°C under a 5% CO₂ humidified atmosphere and passaged at 80% confluency. For microinjection, cells were seeded at a density of $\sim 6 \times 10^4$ cells/mL per dish onto MatTek™ 14 mm dishes (Ashland, MA) which were coated overnight with fibronectin and allowed to adhere overnight. Transfection of adhered cells was performed by removing the complete growth media and washing the cell monolayers once with serum free DMEM. During this time, plasmid DNA was complexed with Lipofectamine2000™ in serum free DMEM. For each dish, 0.4 µg of DNA was added to 25 µL of serum free DMEM and allowed to equilibrate while 1 µL of Lipofectamine2000™ was mixed carefully with 25 µL of DMEM. After five minutes, the two mixtures were combined and allowed to form DNA-lipid complexes for 20 minutes at room temperature whereupon 50 µL was added to each well. After a 6 h incubation of the Lipofectamine2000™-DNA complexes with cell monolayers, the transfection media

was removed and replaced with complete media and the cells were cultured overnight to allow for mCherry expression.

Microinjection

After successful transfection was visualized *via* mCherry fluorescent signal, cells were injected using an Eppendorf FemtoJet[®] Microinjector controlled by an InjectMan[®] NI 2 micromanipulator in a manner similar to that described previously¹⁰⁹. Cells were washed once with DPBS to remove excess media and injection was performed on cells incubated in filter-sterilized DPBS. The microinjection tip (Eppendorf Femtotips) was loaded with 10 μ L of QDs (0.2 μ m filtered). QDs capped with DHLA-PEG₇₅₀-OMe and CL4 were filtered using DPBS alone while QDs capped with DHLA-PEG₆₀₀-NTA were complexed with ~20 equivalents of NiCl₂ for 20 minutes and then filtered with 0.5% FBS in DPBS to increase intracellular stability of the QDs upon injection. Injection time and pressure was optimized for each tip loading to ensure cellular viability upon injection and uniform distribution of QDs throughout the cytosol. Typical injection conditions used were 0.6 sec at pressures of 600-700 hPa.

Microscopy and Image Analysis

Differential interference contrast (DIC) and epifluorescence microscopy were utilized to determine the QD distribution throughout the cells and visualize the FRET interaction between the injected QDs and the expressed mCherry protein. Images were acquired with an Olympus IX-71 total internal reflection fluorescence microscope equipped with a 60x oil immersion lens. Samples were excited using a metal halide arc

lamp and images were collected using the excitation and emission settings described in the SI⁹⁶. Various fields were examined for mCherry expression and injection was performed such that fields of view were comprised of cells containing 1) QD donor only, 2) mCherry acceptor only and 3) both QD donor and mCherry acceptor. This approach provided the necessary controls for FRET-based image analysis. After injection, fields were imaged for the donor excitation and emission (410 nm and 435 nm, respectively), acceptor excitation and emission (576 nm and 620 nm, respectively) and donor excitation with acceptor emission (410 nm and 620 nm, respectively) in addition to DIC images. Relative quantification of relative acceptor sensitization across ligand species was performed by first performing a background correction of all images followed by normalization of the intensity of the FRET channel to the ligand that mediated the most efficient FRET (CL4 in all cases). All data analyses were performed using Image J (ver. 1.48v). The images were false-colored and prepared for publication using MetaMorph Advanced software (ver. 7.8.0.0).

Gel Electrophoresis

Gel electrophoresis (1% low EEO agarose (Sigma)) was performed on DHLA-PEG₆₀₀-NTA and CL4 QDs assembled with mCherry protein to demonstrate ratiometric assembly. QDs (7.5 pmol) were complexed with increasing ratios of mCherry protein in DPBS at QD-mCherry ratios ranging from 1:1 to 1:30 and allowed to incubate for 30 minutes. Additionally, an mCherry only control was included at the 1:30 mCherry equivalent. QD-protein mixtures were subjected to electrophoresis for 30 minutes and images were taken at 5 min intervals.

FRET Analysis

To determine the FRET efficiency of the QD-mCherry complexes, QDs were assembled with mCherry protein at QD-mCherry ratios from 1:1 to 1:30 and were allowed to incubate for 30 minutes. Control solutions containing mCherry alone were included at all mCherry equivalents to determine the contribution of direct excitation of the acceptor in absence of the donor. The assemblies were excited at 400 nm using a Tecan Infinite M1000 microplate reader and emission spectra was collected from 450-700 nm. The FRET efficiency at each QD-mCherry ratio was determined using the Eq. 3, where F_{DA} and F_D are the fluorescence intensity of the QD donor in the presence and absence of the mCherry acceptor, respectively. The QD-mCherry separation (r) distance for each ratio was determined using the results of the efficiency calculation and according to Eq. 4, where R_0 is the calculated Förster distance for the donor-acceptor pair. Data analysis was performed in Excel (ver. 14.0).

Results

Experimental Rationale and Design

The design and implementation of a QD-protein FRET ensemble as an effective intracellular sensing modality first requires the careful consideration of two critical elements: (1) the FRET efficiency of the assembly wherein the donor-acceptor distance can be manipulated and (2) control over the intracellular localization of the sensing

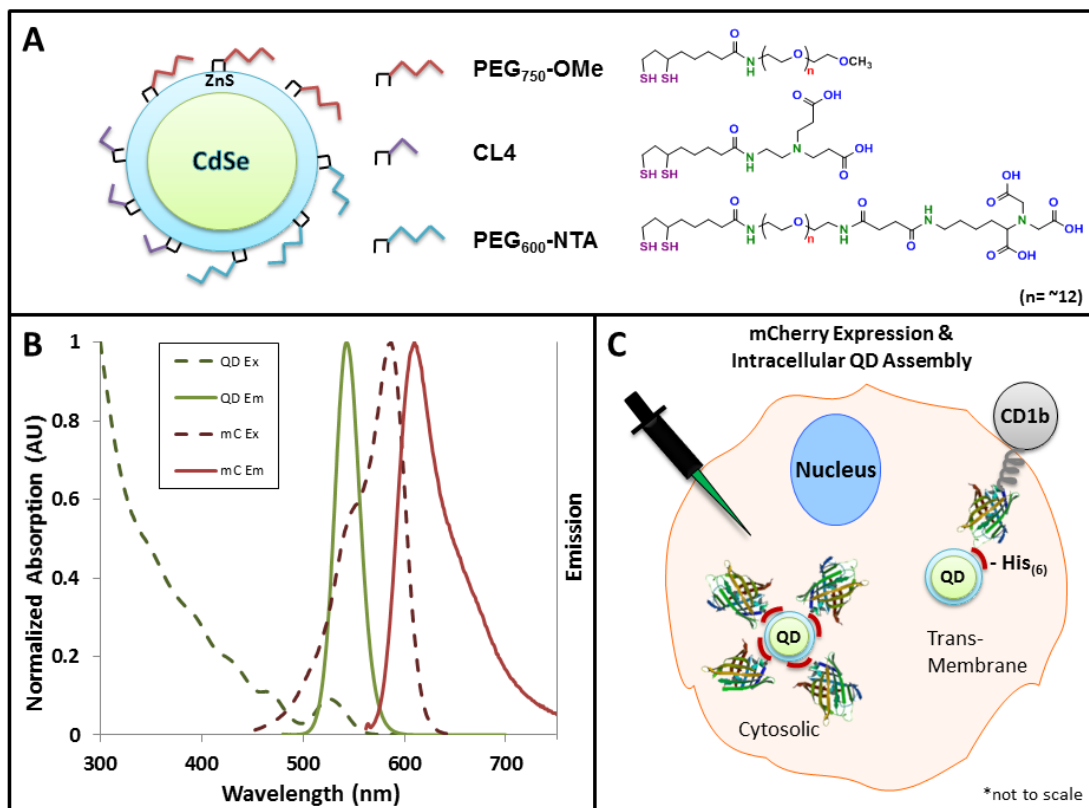


Figure 6. Fluorescent materials and FRET rationale used in this study.

(A) Schematic of CdSe-ZnS core-shell QDs and various capping ligands. (B) Absorbance and emission spectra of the QD and mCherry (mC) donor-acceptor pair showing significant overlap of the QD emission and mCherry absorption, allowing for FRET-sensitized emission of mCherry. (C) Intracellular QD-mCherry assembly strategies. mCherry was expressed either free in the cytosol or as a fusion to the C-terminus of the transmembrane receptor, CD1b. Upon microinjection of QDs, a His₆ motif on the C-terminus of the mCherry drove the intracellular assembly of mCherry to the QD surface either in the cytosol or at the cytofacial leaflet of the plasma membrane.

assembly. Our goal in this study was to assess the ability to control the intracellular FRET efficiency of a QD-mCherry donor-acceptor assembly by modulating the ligand coating on the QD donor while simultaneously site-specifically expressing the mCherry acceptor to control the location of the *in situ* assembled QD-mCherry complex (cytosol *versus* the cytofacial leaflet of the plasma membrane). We began these studies by first performing QD-mCherry assembly and FRET efficiency experiments outside the cellular environment. We subsequently employed microinjection of the QD donor coupled with transient transfection/expression of the mCherry acceptor to determine the efficiency of site-specific intracellular FRET.

The ligands used in this study included: (1) CL4, a small zwitterionic molecule bearing two carboxyl groups and one each secondary and tertiary amine moieties (length = ~1.8 nm)¹⁰⁷, (2) DHLA-PEG₇₅₀-OME (PEG₇₅₀-OMe; length = ~6.8 nm)¹⁰⁷, a PEGylated ligand terminating with a neutral methoxy group, and (3) DHLA-PEG₆₀₀-NTA (PEG₆₀₀-NTA; length = ~6 nm)¹⁰⁸, a shorter PEGylated ligand that terminates with a negatively charged nitrilotriacetic acid (NTA) function (Figure 6A). All three ligands share the same DHLA anchor wherein the thiol pair mediates stable binding of the ligand to the ZnS shell. This panel of ligands was selected specifically because they have been shown to mediate intracellular QD stability¹⁰⁷ and they span a range of lengths for controlling the donor-acceptor distance in the FRET assembly. It is worth noting that the CL4 and DHLA-PEG₇₅₀-OME ligands allow for His-based assembly of the mCherry to the ZnS shell (albeit with differing degrees of accessibility of the His₆ tag to the Zn surface given the varied lengths of the two-ligand species). In contrast, the PEG₆₀₀-NTA ligand promotes assembly to the carboxyl groups on the terminal nitrilotriacetic acid

moiety. As shown in Figure 6B, FRET in this system is driven by the significant degree of spectral overlap between the emission of the 545 nm QD donor and the absorbance of the mCherry acceptor. Two further features drive efficient FRET in this QD-protein system: (1) the excitation of the QDs in the UV (~350 nm) resulting in negligible direct excitation of the fluorescent protein acceptor and (2) the ability to array multiple mCherry protein acceptors around the central QD scaffold which enhances overall FRET efficiency¹¹⁰. Finally, the site-specific assembly of the QD-mCherry FRET ensemble was controlled by expressing the mCherry acceptor in either of two forms; free in the cytosol or appended to the inner leaflet of the plasma membrane *via* its expression as a fusion to the extracellular and transmembrane domains of CD1b (see SI⁹⁶). Upon injection of the QDs into the cytosol, the free C-terminal His₆ domain on either mCherry variant mediated the localized assembly process (Figure 6C).

Efficacy of the FRET System

We first performed *in vitro* assembly experiments to ensure that the His₆-tagged mCherry could successfully assemble to the QD surface. Here, increasing ratios of mCherry were complexed with the CL4- and PEG₆₀₀-NTA-capped QDs and the complexes were subjected to gel electrophoresis. As shown in Figure 7A, QDs bearing either ligand species showed a decreased migration within the gel as increasing numbers of mCherry were added, demonstrating an increase in the size of the QD-mCherry complexes. Analysis of the PEG₇₅₀-OMe QDs was not performed here as they have no net charge and would not migrate when subjected to electrophoresis. Interestingly,

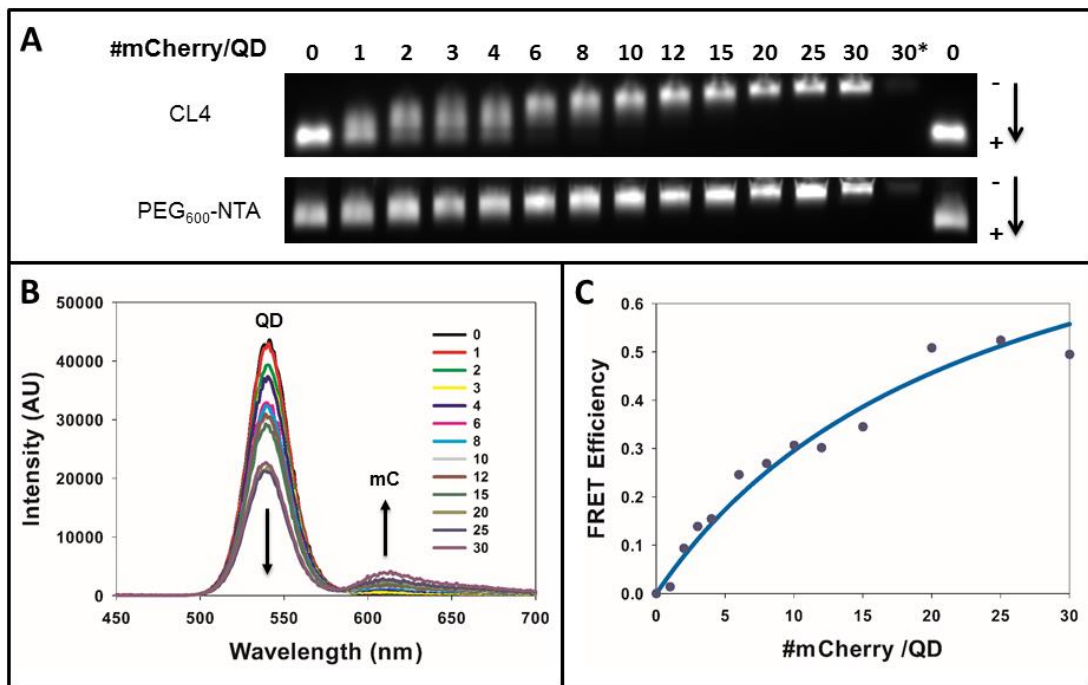


Figure 7. Assembly and FRET analysis of the QD-mCherry donor-acceptor pair. (A) 545 nm-emitting QDs capped with CL4 or PEG₆₀₀-NTA were assembled with increasing ratios of mCherry and separated on 1% agarose gels. (B) Emission spectra of CL4 capped 550 nm QDs showing sensitization of QD donor emission with increasing ratio of mCherry acceptor. Data has been corrected for direct excitation of mCherry. (C) Plot of QD-mCherry FRET efficiency as a function of increasing QD-mCherry ratio. Line is fit to Eq. 4 by using the calculated r_{DA} values for each ratio and back-calculating what the corresponding FRET efficiency should be for that ratio of QD donor to mCherry acceptor.

assembly of mCherry to the PEG₆₀₀-NTA QDs resulted in discrete gel bands at nearly all QD-mCherry ratios while assembly of the protein to CL4-capped QDs yielded a “smearing” banding pattern at ratios below ~10 indicative of a mixed population of QDs wherein the number of proteins per QD, or valence, varied. This has been observed previously and been consistent with a Poissonian distribution at lower QD-protein valencies⁷⁶. At valences greater than ~10, however, we observed tight, discrete fluorescent bands for QDs capped with both ligands demonstrating the formation of more homogeneous populations of QD-mCherry complexes. These results are not unexpected given the fact that the manner in which the His₆-tagged mCherry assembles to the QD surface differs slightly between these two QD species. For the PEG₆₀₀-NTA QDs, the NTA groups on the termini of the PEG₆₀₀-NTA are more readily accessible to the His₆ tag on the mCherry while for the CL4-capped QDs, the binding of the His₆ tag to the Zn-rich surface of the QD shell requires the interdigitation of the tag through the ligand layer to reach the QD shell. Despite this slight difference, our results clearly show that at mCherry valences >10, similar binding/assembly efficiencies are obtained for both QDs.

Having demonstrated the controlled assembly of QD-mCherry complexes, we next performed FRET analysis to determine the efficiency of the energy transfer process between the QD donor and the mCherry acceptor. For this analysis, we opted to use QDs capped with CL4, the shortest ligand used in these studies and, therefore, the species expected to mediate the most efficient FRET. To determine the FRET efficiency of the QD-mCherry FRET pair, increasing ratios of mCherry were assembled onto the QD surface and the emission spectra of the complexes were read when excited at 400 nm. As increasing numbers of mCherry were arrayed around the central QD, a concomitant

decrease in QD emission coupled with a corresponding increase in mCherry emission was observed (Figure 7B). As shown in Figure 7C, a plot of the FRET efficiency (see Experimental) *versus* the QD-mCherry ratio initially follows a linear increase that corresponds to the sum of the efficiencies of the aforementioned Poissonian distribution of mCherry per QD, as the number of uncoordinated QDs decreased (*i.e.* QDs with no mCherry coordinated to the surface), the FRET efficiency reaches a plateau that corresponds to the maximum potential transfer possible for the donor-acceptor pair based on both maximum loading capacity and quantum yield of the QD donor. For the CL4 capped QDs a maximum FRET efficiency of ~50% was achieved when ~20 mCherry proteins per QD were assembled onto the QD surface. This corresponded to a calculated center-to-center QD-mCherry distance of ~8.1 nm (using an R_0 value of 6.5 nm for the FRET pair). This calculated distance agrees well with the known sizes of both the QDs (~3 nm radius) and of mCherry (~3 nm radius from barrel end to protein center) when one factors in the CL4 ligand spacing and the enhanced FRET efficiency driven by the arraying of multiple mCherry acceptors around the QD core. Further, these results agree well with our previous characterization of the packing of mCherry to the surface of QDs of this size^{85, 111}. Using mathematical modeling that accounted for the QD surface by calculating the surface area of a 5.8 nm sphere (545 nm QD diameter ~2.9 nm) and estimating the fitting cross section for the maximum mCherry protein per QD, a single quantum dot should be able to carry 20 ± 4 mCherry proteins¹¹¹. Additionally, the other two capping ligands were analyzed and found to have maximum FRET efficiencies of 61% for the PEG₆₀₀-NTA QDs and 38% for the PEG₇₅₀-OMe QDs (see SI⁹⁶). We attribute these variations to differing quantum yields of the QD batches. Specifically,

QDs in organic solution have an extremely high quantum yield (> 90%) but when cap-exchanged their QY's decrease to around 20%⁶⁹. This reduction is thought to be caused in part by the interference of the capping ligand on the available surface states of the outer shell. Additionally, the capping exchange process in itself can cause defects in the QD surface, which has previously been discussed as a major impetus for high QYs¹¹²⁻¹¹³. As the capping ligands and the exchange process damage is not identical for each QD batch, the final QY of the QDs can vary slightly and therefore affect the final efficiency.

Intracellular QD-mCherry Assembly and FRET Efficiency

Having confirmed the successful controlled assembly of His₆-tagged mCherry to the QD donor surface and determined the FRET efficiency of the resultant ensembles, we next sought to characterize the intracellular FRET efficiency as a function of both the QD ligand coating and the location of the donor-acceptor complex. To achieve this, COS-1 cells were transiently transfected to express His₆-mCherry either free in the cytosol or appended to the inner leaflet of the plasma membrane as a fusion to the cell surface

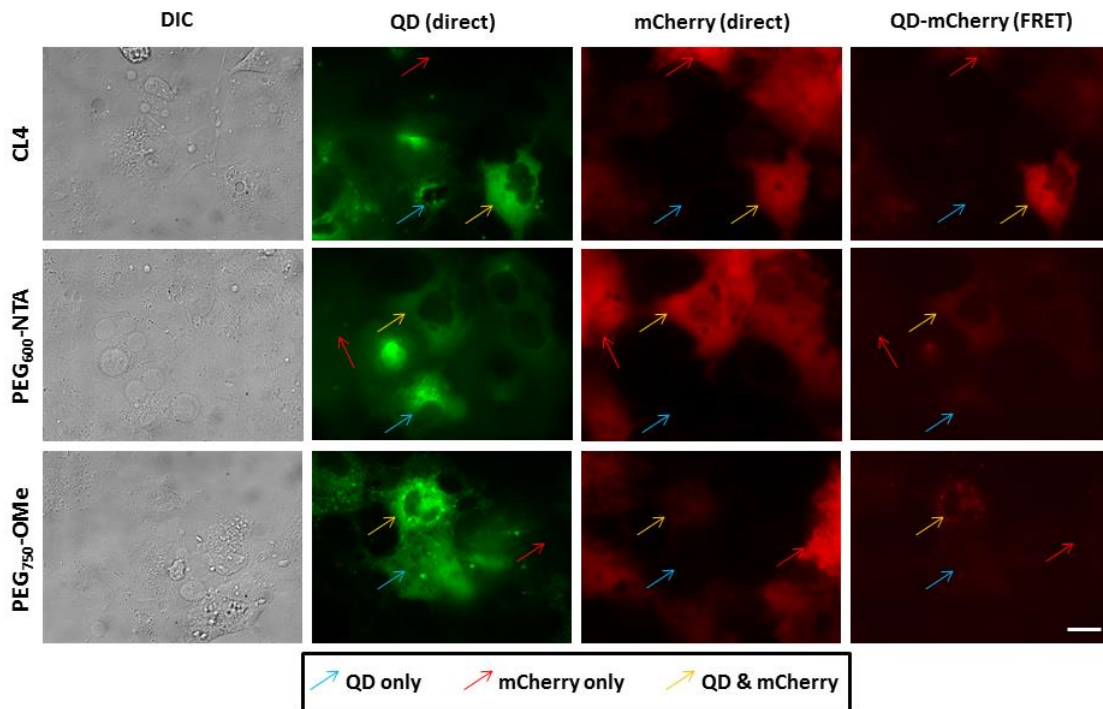


Figure 8. Cytosolic assembly of QDs and mCherry. COS-1 cells expressing His₆-terminated cytosolic mCherry proteins were microinjected with QDs coated with CL4, PEG₆₀₀-NTA and PEG₇₅₀-OMe. Fields were specifically imaged where cells contained mCherry only (red arrow), QDs only (blue arrow) or both QD and mCherry (yellow arrow) to allow for the appropriate FRET imaging controls. Note the level of efficient FRET present in cells injected with the CL4 QDs, with slightly less efficient FRET observed in cells injected with PEG₆₀₀-NTA QDs. PEG₇₅₀-OMe QDs appeared to mediate the least efficient FRET with intracellular mCherry. Scale bar is 20 μ m.

receptor CD1b. During these studies, we noted that the transfection efficiency across experiments was typically ~60-70%. Cells were then injected with QDs capped with CL4, PEG₆₀₀-NTA or PEG₇₅₀-OMe ligands. We employed an injection strategy that ensured all the necessary controls were present in a single field of view. Specifically, the injection was executed such that each field of view contained cells with QD donor only (no mCherry acceptor), mCherry acceptor only (no QD donor) or both the QD and mCherry acceptor. We then imaged these fields for the direct excitation/emission of the donor and acceptor and the FRET between the QD and mCherry. In this manner, the contribution of the QD donor emission and direct mCherry acceptor emission in the FRET channel could be accounted for in the ensuing image analysis.

As shown in Figure 8, both the injected QDs and the cytosolically expressed mCherry displayed a diffuse fluorescence pattern with each fluorophore being well distributed throughout the entire cell volume. Interestingly, quantitative analysis of the FRET channel showed clear differences in the ligand-specific FRET efficiency. Specifically, the cells injected with the CL4-coated QDs displayed the most efficient FRET as evidenced by the highest fluorescence intensity in the FRET channel for this ligand compared to the PEG₆₀₀-NTA and PEG₇₅₀-OMe. Relative quantification of the fluorescence intensities in the FRET channel revealed that for the CL4 ligand the QD-mCherry FRET sensitization was ~7-fold greater than PEG₆₀₀-NTA and ~5-fold greater than PEG₇₅₀-OMe (see SI ⁹⁶). Clearly the shorter, compact CL4 ligand (~1.8 nm in length) afforded the more robust assembly of the His₆-mCherry protein to the QD surface relative to the other two longer ligands whose lengths are greater than 6 nm.

We then expressed mCherry on the inner leaflet of the plasma membrane as a fusion to CD1b and confirmed its localization at the membrane by immunofluorescence analysis (SI). Here, slightly different FRET results were obtained when QDs bearing the various ligands under study were injected (Figure 9). First, it was apparent that the overall fluorescence intensity of the mCherry (under direct excitation) was reduced ~5-fold compared to when it was expressed freely in the cytosol (see SI). We attributed this lower direct fluorescence emission from the mCherry to the fact that the protein was expressed within the secretory pathway and processed/directed to the membrane which

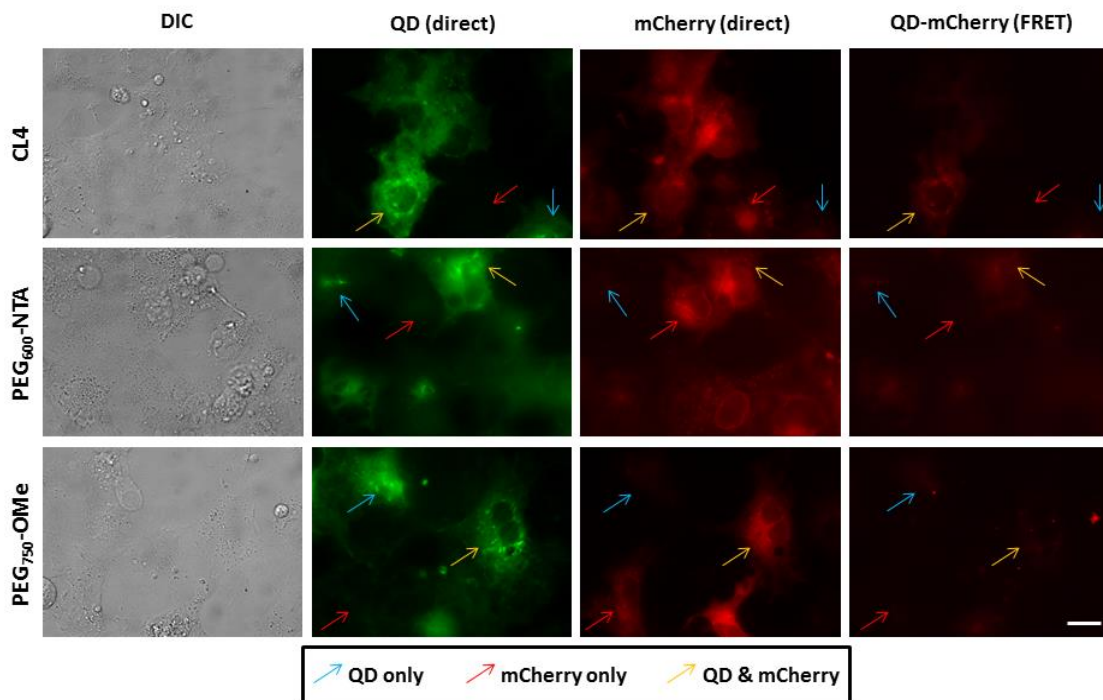


Figure 9. Assembly of QDs and mCherry at the cytofacial leaflet of the plasma membrane. COS-1 cells expressing mCherry proteins on the cytofacial leaflet of the plasma membrane (as a fusion to CD1b) were microinjected with QDs coated with CL4, PEG₆₀₀-NTA and PEG₇₅₀-OMe. Imaging was performed as described for Figure 8. Note the lower level of mCherry expression due to its localization at the plasma membrane. The FRET signal for the CL4 QDs bound to membrane expressed mCherry was ~50% that observed for cytosolic mCherry. Scale bar is 20um.

resulted in an overall lower level of intracellular mCherry. It was also clear that the efficiency of QD-mCherry FRET was diminished as a result of the mCherry being expressed appended to the inner leaflet of the membrane. Upon direct comparison, the FRET for CL4-capped QDs with membrane-bound mCherry was ~60% that observed for this same donor-acceptor pair in the cytosol (see SI). Further, the FRET from for the PEG₆₀₀-NTA QDs was also markedly reduced and there was no measurable FRET signal at the plasma membrane for QDs capped with PEG₇₅₀-OMe. While the lower level of mCherry expression likely contributed to this, it is also likely that steric hindrance of the mCherry tethered to the inner leaflet played a role in diminishing the ability of the injected QDs to dock onto the terminal His₆ tag. In this instance, it was only the small CL4 ligand-capped QDs that were able to engage in efficient FRET with membrane-bound mCherry. Taken together with the cytosolic mCherry results, these findings clearly demonstrate that not only can the localized expression of the mCherry acceptor mediate the controlled site-specific assembly of QD-fluorescent protein but also the nature of the capping ligand plays a critical role in the efficiency of FRET once the resulting donor-acceptor complex is formed.

Discussion

Our need to understand how to exert fine control over nanomaterials when interfaced with cells continues to grow at an almost unabated pace^{20, 114}. New nanoparticle formulations and delivery modalities necessitate that one have a detailed working knowledge of how to control the delivery, assembly and intracellular fate of nanoparticle-biological ensembles. This is indeed true in the case of nanoparticle-based

sensing platforms, particularly those that employ FRET as the readout modality. Multiple factors need to be taken into account including: 1) the facile generation of the FRET donor-acceptor assembly, 2) the delivery of the ensemble sensor, and 3) the efficacy of the sensor *in vitro*. Our goal in this study was to perform a detailed characterization of the efficiency of the intracellular assembly of a QD-fluorescent protein FRET pair.

Specifically, we were interested in the role played by the capping ligand on the QD surface in modulating the FRET efficiency in the assembly as well as the ability to site-specifically control the intracellular generation of the FRET complex.

In previous work, we showed the ability to use metal affinity coordination to drive the intracellular *in situ* assembly of microinjected commercial polymer-coated QDs with His₆-tagged mCherry protein transiently expressed in the cytosol⁹³. Despite the positive results obtained in that work, much more remains to be understood in how to control such assemblies intracellularly if they are to be used as the foundation of FRET-based sensing. For example, the proprietary nature of the polymer capping ligand present on the commercially available QDs used in our previous work did not allow for discrete control of the distance between the QD donor and protein acceptor. Additionally, no strategy was employed to direct the assembly of the FRET complex to a particular subcellular location. Building on the initial success of those studies, our goal here was to perform a more detailed, controlled analysis of the role played by both the QD donor material itself as well as the cellular location of QD-protein assembly. Using the same transient expression/injection approach we first systematically tested a suite of QD-capping ligands for their ability to assemble to and engage in FRET with mCherry proteins outside of the cellular environment. Both a short zwitterionic capping ligand (CL4) and a

longer PEGylated ligand showed the ability to mediate assembly of His₆-tagged mCherry proteins in a quantitative manner. The CL4 ligand facilitated a maximal FRET efficiency of ~50% when ~20 mCherry proteins were arrayed around the central QD. When tested intracellularly, this same CL4 ligand mediated the most efficient rate of FRET of the ligands tested, a testament to the facile and stable assembly of the His₆ tag to the Zn shell on the QD donor. Interestingly, we noted distinct differences in the FRET efficiency depending on whether the mCherry acceptor was expressed in the cytosol or appended to the inner leaflet of the plasma membrane, which tells us that the specific location of the final complex directly affects the coordination potential of the intracellular assembly. This should be taken into account for the future design and implementation of such systems, as the sensitivity of the FRET constructs will vary depending on the potential maximum FRET efficiency.

A few salient features of this system bear pointing out. First, the intracellular synthesis of the acceptor portion of the FRET ensemble is at the same time elegant and practical; it obviates the need for assembly of the preformed FRET ensemble outside the cell followed by its subsequent cellular delivery and targeting. Second, the intracellular location of the assembled complex was controlled entirely by manipulating the location of the His₆-bearing protein acceptor. The success of this approach opens the exciting possibility of other means of directing the site-specific, acceptor-driven QD-protein assembly process. For example, instead of expression of as a fusion with a transmembrane receptor, the inclusion of a post-translational modification signal (e.g., palmitoylation¹¹⁵ or farnesylation¹¹⁶ signal sequence) or a nuclear localization signal¹¹⁷ could have been encoded in the expressed mCherry acceptor. Further, the tractable nature

of the genetically-encoded mCherry acceptor allows for the modification of the spacer sequence between the His₆ tag and the mCherry protein. Here, the inclusion of recognition sequences for kinases, proteases or other enzymes can realize the sensing modalities for a variety of cellular processes. It is fundamental studies such as those performed herein that are a critical first step in building the appropriate “toolbox” that will ultimately drive the successful implementation of these QD-based FRET sensors that utilize intracellularly expressed fluorescent proteins as energy acceptors for the sensing of myriad physiological processes.

Chapter 3: Design and Implementation of a Novel Actuation Method for Cellular Drug Delivery

Introduction

Systemic delivery, the most commonly available drug delivery method available on the market, requires large repeated doses to effectively treat many diseases and it can have serious secondary side effects¹¹⁸. The reduction of these secondary side effects, in addition to reduced dosages, is at the forefront of the development of new drug delivery methods. One critical area of research is the development of theranostic agents which combine both a therapeutic and a diagnostic moiety to allow for simultaneous delivery and visualization of the release of the therapeutic agent³. Development of these theranostic agents requires that numerous criteria be met. First, the agent itself must be non-toxic and biocompatible. Second, it must have long circulation time coupled with the ability to be cleared from the bloodstream. Finally, the agent must efficiently carry and deliver therapeutic cargo with fidelity and control. Cumulatively, achieving these properties within the context of a single deliverable agent is a considerable challenge.

One area of research that is attempting to overcome these obstacles is the design of nanoparticle (NP)-mediated drug delivery complexes¹⁴⁻¹⁵. NPs are on the appropriate size scale for delivery of materials to cells; they are larger than proteins but much smaller than cells and possess a large surface area-to-volume ratio. NPs can be complexed with targeting agents like proteins or peptides, carry drug or imaging cargo and release them *via* a variety of actuation methods. The inherent fluorescence properties of some NPs allows for easy tracking while other NPs must be conjugated to fluorescent molecules for visualization. A critical component of NP-based drug delivery systems is the mechanism

by which the drug cargo is released or “actuated”. As discussed in the Introduction, various NP actuation modalities have been realized to include, for example, the passive efflux of drug cargos from the surface or core of a variety of NPs³⁸. Other forms of NP actuation are active and take advantage of either inherent cellular processes or states (*e.g.*, pH²¹ or enzymatic activity²²) or rely on the use of hardwired devices such as lasers²⁵⁻²⁶ to actively trigger cargo release from the NP. One of the inherent limitations of light-triggered actuation is its limited tissue depth penetration (often only tens to hundreds of microns) which necessitates the development of non-light-based methodologies for active cargo release¹¹⁹. An ideal active NP actuation system would combine the exquisite control of time-resolved cargo release with a simple yet effective triggering mechanism to affect the release of the drug cargo.

Here, we have designed a prototypical NP actuation bioconjugate that incorporates many of the desired attributes of active actuation in a simple, modular, and tractable platform. Importantly, rather than light stimulation, drug release is mediated by the addition of a competitive structural analog to the extracellular medium. The system uses a central QD as the NP scaffold upon which is self-assembled a multicomponent drug delivery complex. The central QD scaffold possesses a multitude of properties that are ideal for controlled drug delivery, as enumerated in the Introduction. Briefly, they are bioconjugatable *via* histidine-tag coordination, they have impressive optical properties for long-term intracellular monitoring and make ideal FRET donors for distance-dependent measurements. See Chapter 5 for more discussion of histidine-tag coordination. The full ensemble conjugate consists of the QD decorated with multiple copies of the bacterial periplasmic transport protein maltose binding protein (MBP). Into the MBP binding

pocket is complexed the cyclodextrin (CD) which exists as a conjugate to either a dye tracer, TideFluor3 (TF3), or the cancer chemotherapeutic, doxorubicin (DOX). Once introduced to cells, the TF3- or DOX-CD is displaced from the ensemble in a time- and dose-dependent manner by the addition of maltose to the extracellular environment. This conjugate system is a novel means by which to achieve the active actuation of NP-appended drug cargos and represents a new pathway for the light-free induction of drug release.

Experimental

Materials

Anotop-10 filters (0.2 μm) and Dulbecco's phosphate buffered saline (DPBS) were purchased from Life Technologies (Carlsbad, CA). Hanks buffered saline solution (HBSS) was made to specifically contain no glucose: 137 mM NaCl, 5.4 mM KCl, 0.3 mM Na_2HPO_4 , 0.4 mM KH_2PO_4 , 4.2 mM NaHCO_3 , 1.3 mM CaCl_2 , 0.5 mM MgCl_2 , 0.4 mM MgSO_4 .

Synthesis of QDs and β -cyclodextrin (βCD) Conjugation

Semiconductor nanocrystals or quantum dots (QDs) were synthesized as previously discussed previously and rendered hydrophilic via cap exchange⁶⁹. Briefly, core-shell CdSe/ZnS QDs were synthesized to have emission maxima centered around 520 nm, or purchased with emission maxima centered around 655nm (Invitrogen), and had their native hydrophobic trioctylphosphine/trioctylphosphine oxide (TOP/TOPO) ligands exchanged for small zwitterionic CL4 capping ligands¹⁰⁷. TEM analysis showed

that the 520 nm QDs had an average diameter of 4.6 ± 0.4 nm. The TideFluor3WS was conjugated to the β CD as previously reported in ¹²⁰ and purified as described in ¹²¹. The DOX conjugated β CD was custom synthesized by BioSynthesis (Lewisville, TX). In brief, β CD was monotosylated by reaction with tosyl chloride, then treated by ethylenediamine to afford amine-functionalized β CD (H_2N - β CD). Meanwhile, doxorubicin was treated by disuccinimidyl suberate (DSS) to yield succinimidyl-activated DOX. Finally, the H_2N - β CD and DSS-DOX were reacted to produce β CD-DOX conjugate, which was purified by reverse phase HPLC and characterized by MALDI-TOF MS (purity >95%). Schematic of final product shown in appendix (Figure A1).

Maltose Binding Protein Synthesis

Maltose binding protein (MBP) was purified from *Escherichia coli* strain BL21(De3) (New England Biolabs Ipswich, MA) harboring a pET22 MBP construct that facilitated the incorporation of a C-terminal hexahistidine tag. Briefly, 5 mL of Terrific Broth (TB) medium containing 100 μ g/mL of ampicillin was inoculated with a single colony from a Lysogeny Broth (LB) Agar plate containing ampicillin. The culture was incubated for 16 hours at 37°C. The entire culture then served as the inoculum for a 500 mL volume of TB containing ampicillin. The culture was incubated at 37°C with shaking in a 2 L baffled flask for approximately 3 hours, until mid-log stage was reached. Protein expression was induced at mid-log phase with the addition of Isopropyl- β -D-thiogalactopyranoside (IPTG) to a final concentration of 0.5 mM. The incubation temperature was decreased to 30°C, protein expression was allowed to proceed for 20

hours. The culture was transferred to a 500 mL centrifuge bottle. Cells were pelleted at 4000 x g for 30 minutes at 4°C. The supernatant was discarded and the pellet frozen at -80°C for 3 hours to improve cell lysis efficiency. The frozen pellet was resuspended in 30 mL of lysis buffer (1/2x PBS, 1 mM EDTA, 0.1% Triton X-100, 1mg/mL lysozyme) then transferred to a 50 mL conical tube. The cell suspension was immobilized on a rocker platform and incubated at room temperature for 30 minutes with gentle agitation to allow for the degradation of the peptidoglycan and bacterial membranes. The suspension was then sonicated 6 times while on ice using a Branon Sonifer 450 (80% duty cycle, output control 5). The lysate was transferred to 50 mL conical tubes and centrifuged at 4500 x g for 30 minutes to pellet insoluble material. Following centrifugation, the supernatant was decanted to a new 50 mL conical tube. A 1 mL bead volume of HisPur Nickel_NTA resin (ThermoFisher) was added to the clarified material. The his-tagged MBP was batch immobilized overnight at 4°C. The Ni-NTA resin was batch washed 3 times with 40 mL wash buffer (50 mM phosphate (pH 7.0) 300 mM NaCl, 10 mM imidazole). Resin was then transferred to a 5 mL disposable column and protein eluted with wash buffer containing 250 mM imidazole. Protein content of fractions collected from the Ni-NTA column was quickly assessed via 280 nm absorbance using a NanoDrop 1000 instrument (Thermo Fisher). Fractions containing protein were pooled and further resolved via FPLC using the NGC Medium Pressure Liquid Chromatography System and Enrich 70 Superdex column (BioRad). Fractions containing MBP were pooled, quantitated, then snap frozen in a methanol dry ice bath.

Gel Electrophoresis

Gel electrophoresis (1% low melting temperature agarose (Sigma)) was performed on QDs assembled with native MBP to analyze the ratiometric assembly of MBP to the QD surface. QDs (7.5 pmol) were complexed with increasing ratios of MBP in DPBS at ratios ranging from 1:1 to 1:15 (QD:MBP) and allowed to incubate at room temperature for 30 minutes. QD-protein mixtures were subjected to electrophoresis for 15 minutes and images were taken at 5 min intervals.

Preparation of QD-MBP- β CD Conjugates

Initial studies were performed to ensure that the MBP was fully loaded with the β CD conjugates before complexing them with the QD surface. First, aliquots of MBP in 20% glycerol were washed to increase protein concentration and remove glycerol. To wash, 30 kDa Amicon® Ultra 0.5 mL filters (Millipore, MA) were loaded with 500 μ L of MBP stock and spun for 10 minutes at 14K RPM. This procedure was repeated two subsequent times, all washes were performed in Hanks Buffered Salt Solution (no glucose) (HBSS). The concentrated MBP solution was spun off the filter at 1000 RPM for 2 minutes, achieving a 22X concentrated MBP stock. Using the concentrated MBP stock, an incubation solution containing 50 μ M of MBP and 250 μ M of either the β CD-TF3 or β CD-DOX at a volume of 23 μ L was incubated at 4°C overnight. For FRET analysis and cellular injections, the solution was diluted to 500 μ L and spun using the Amicon filters to remove unincorporated β CD-conjugates; for analysis of maltose release the incubation solution was used with excess β CD. For cellular injections the loaded MBP was subsequently incubated with 5 μ M 520 nm CL4-capped QDs for 1 h at room

temperature (producing a 1:10 QD:MBP final ratio), or diluted and used for the FRET analysis described in the next section.

Analysis of QD-MBP- β CD Conjugate Responsiveness

To determine the responsiveness of the QD-MBP- β CD-TF3/DOX constructs to varying concentrations of maltose, unfiltered β CD-loaded MBP was incubated at a ratio of 1:10 with 520 nm emitting QDs (7.5 pmol QD; ratio 1:10 (QD:MBP)) for 1 h at room temperature. Control solutions containing TF3 alone were included for all ratios to determine the contribution of direct TF3 excitation, this was not performed for the DOX constructs as DOX has negligible emission in the absence of DNA. The constructs were excited at 400 nm using a Tecan Infinite M1000 microplate reader and emission spectra was collected from 450-700 nm for the TF3 constructs and from 450-600 for the DOX constructs. After initial spectra were taken for each well to ensure uniformity, increasing concentrations of maltose were added to the wells at a 1:1 (v:v) ratio so the final concentration of maltose in each well equated to a range from 50 nM to 20 mM. The spectra were then measured for each maltose concentration. The FRET efficiency at each concentration was determined using the equation described in the Introduction:

$$\text{FRET}_E = 1 - \frac{F_{DA}}{F_D} \quad \text{Eq 3}$$

where F_{DA} and F_D are the fluorescence intensities of the QD donor in the presence and absence of the β CD -TF3/DOX acceptor, respectively. The emission profiles of the TF3 spectra were normalized to the auto-fluorescence produced by corresponding TF3 concentrations alone.

To further analyze the FRET efficiency, increasing amounts of loaded MBP were complexed with 7.5 pmol of QD at ratios from 1:1 to 1:10 (QD:MBP). To ensure that the passivation of the QD surface by His₆ binding was constant for each QD: MBP ratio, unloaded MBP was used to achieve a total ratio of 1:10 MBP (example; for a ratio of 1:3 loaded MBP, a ratio of 1:7 unloaded MBP was added to the incubation solution). The spectra were measured to determine the FRET efficiency over increasing ratios of β CD-TF3/DOX per QD.

The QD-TF3/DOX separation (r) distance for each ratio was determined according to the following equation:

$$E_n = \frac{n \left(\frac{R_0}{r_{DA}} \right)^6}{1 + n \left(\frac{R_0}{r_{DA}} \right)^6} \quad \text{Eq 4}$$

where R_0 is the calculated Förster distance for the donor-acceptor pair. Data analysis was performed in Excel (ver. 14.0).

Cellular Culture and Plating

African Green Monkey kidney cells (COS-1) were cultured using T75 tissue culture flasks in complete growth medium (Dulbecco's Modified Eagle's Medium (DMEM; American Type Culture Collection ATCC)) supplemented with 10% (v/v) heat inactivated fetal bovine serum (ATCC) and 1% (v/v) antibiotic/antimycotic (Sigma). Flasks were incubated under a 5% CO₂ humidified atmosphere at 37°C and passaged at 80% confluency. For microinjection, cells were seeded at a density of $\sim 7 \times 10^4$ cells/mL per dish onto MatTek™ 14 mm dishes (Ashland, MA) and allowed to incubate overnight.

Microinjection

Adherent COS-1 cells were injected using an Eppendorf FemtoJet[®] 4i microinjector controlled by an InjectMan[®] 4 micromanipulator in a manner similar to that described previously¹⁰⁹. Cells were prepared for injection by washing once with glucose-free HBSS to remove excess media, then allowed to incubate for 5-10 minutes in fresh HBSS. The solution was then replaced with fresh HBSS prior to injection. The microinjection tip (Eppendorf Femtotips) was loaded with 5-10 μL of the 5 μM QD-MBP- βCD -TF3/DOX constructs with excess βCD -TF3/DOX removed by filtration. Injection time (0.48 sec) and pressure (300 hPa) was maintained for uniformity of injection volume and to produce an even distribution of QDs throughout the cytosol. As an internal control for the QD-MBP- βCD -DOX injections, far red-emitting 655 nm QDs capped with CL4 at a concentration of 300 nM were added to the complexes prior to filtration and loading into the tip.

Maltose Delivery

After a minimum of 50 cells were microinjected with either the QD-MBP- βCD -TF3 or QD-MBP- βCD -DOX constructs, dishes were transferred to a Nikon A1RSi confocal microscope and placed within a cellular incubator maintained at 37 °C. The area of microinjected cells was located with a 10x objective before moving to 60x oil immersion objective for imaging. For each time course, 5 locations were chosen per plate, 7 each 1.5 nm slices were taken per z-stack and 2x averaging was performed per 512 x 512 pixel image. This timing allowed for an entire set of images to be captured in 1 minute, 43 seconds with time points taken every two minutes for a total of 30 minutes for

each maltose delivery. Maltose solutions in HBSS were added between the final image of time point one and the beginning of the second time point so that the final concentration of maltose in the plate ranged from 1.25 mM to 30 mM.

Image Acquisition and Analysis

Images were captured using the spectral imaging modality on the Nikon A1RSi confocal imaging system. Briefly, a 32 PMT array captured the intensity for a range of wavelengths as designated by the experimental setup. Three wavelength 'bin' sizes were available for use: 2.5, 6, and 10 which facilitate capture of a max wavelength range of 80, 192 and 320 nm, respectively, where the PMT spectral range extends from 400 nm to 750 nm. For our experimental setup, ranges were chosen to include the QD peak and the TF3 (470 nm - 660 nm) or the QD and the far red QD control (480 nm - 740 nm), and given the scale of these ranges the largest bin size (10 nm) was chosen. The images produced by this setup were compilations of the intensities for each of the PMTs false colored for their delineated wavelength range. To include as much cellular cytosol as possible and because of the inherent dimness of a spectral image acquisition, the pinhole was set to maximum during image acquisition. As each PMT recorded a maximum intensity associated with its designated wavelength range, a spectral intensity profile was produced for each pixel within the image. To analyze this data, specific regions of interest (ROIs) were chosen to focus on the cytosolic environment and the spectral profiles for the brightest three slices (of the 7 originally captured) were exported into Microsoft Excel. These were then summed together to give the overall intensity for that ROI at that time point. Data was compiled for all time points and either the donor/acceptor ratio (TF3

samples) or for the normalized donor PL increase of the QD peak (DOX samples) was calculated for each ROI and averaged over all the individual ROIs taken at each concentration. Donor PL increase was calculated using Eq. 3, and the 520 nm QD peak intensity was normalized to the 655 nm QD peak intensity, which should not be affected by maltose delivery and remain somewhat constant throughout experimental acquisition. Analysis was performed in Excel and graphs were plotted using GraphPad Prism (V7).

Fluorescence Lifetime Imaging Measurement (FLIM)

Injected cells were also imaged using a ISS LSM upgrade system for the Nikon A1SRi on trial from the company. The system was set up with a 405 nm laser launch. The laser was either modulated by the data acquisition card (FastFLIM) or self-modulated. FastFLIM (proprietary technology) was used as it is frequency based and faster and more sensitive than TCSPC (time domain) mode. The modulation frequency was set to 20MHz. To be delivered to the Nikon confocal head, the excitation laser beam was coupled to a single mode fiber. The coupling efficiency of laser into the fiber optic were around 30% (140 μ W out of 350 μ W input power). Prior to experimental imaging, the system was calibrated with a Coumarin 6 solution (2.55 ns) and a fluorescein solution (4.00 ns - a fluorescence standard) was tested to verify the system functioned as expected. Samples injected with the QDs alone were imaged first to determine the 520nm QD's lifetime within the cytosolic environment, and measurements were taken over 12 minutes to determine stability and decay. This was also compared to the 520 nm QD's lifetime with 10 unloaded MBP attached per QD, this data showed no change in the lifetime (data not shown). Finally, both the QD-MBP- β CD-TF3 and QD-MBP- β CD-DOX constructs

were measured before and after addition of 30 mM maltose to the cell solutions to determine the lifetime change in response to maltose addition.

Results and Discussion

Design and Rationale of Theranostic NP Actuation

Efficient theranostic nanostructures depend on the specific and controlled release of cargo from the NP structure, and such a process requires careful design of the nanoparticle complex. To be effective, the NP complex must not only be easily traceable/visualized, but the release of the NP-appended drug cargo must be induced with fine control. Importantly, both of these processes must be carried out with exquisite spatiotemporal resolution. With these goals in mind, we set out to produce a multifunctional nanoparticle composite that would remain unresponsive until the addition of an inert secondary triggering molecule. Ideally, that process could be monitored optically in real-time using FRET. Here we have designed a NP drug delivery system that is activated in a novel way. Rather than using ‘hard-wired’ modalities such as light⁵⁷, magnetic field⁵⁴⁻⁵⁵, or ultrasound⁶¹, here we induce drug release by simple addition of an inert molecule to the extracellular medium. The addition of the inert sugar maltose triggers the release of the analog β CD by competitively displacing it from the binding pocket, thereby delivering the cargo to the cells. Monitoring this release is slightly varied for each of the systems, as can be seen in Figure 10 A/B. TF3 will undergo ‘standard’ FRET with the QD donor, and so two peaks will be visible when the MBP binding pocket is occupied by the β CD-TF3; a quenched QD peak and a smaller TF3 sensitized peak. With

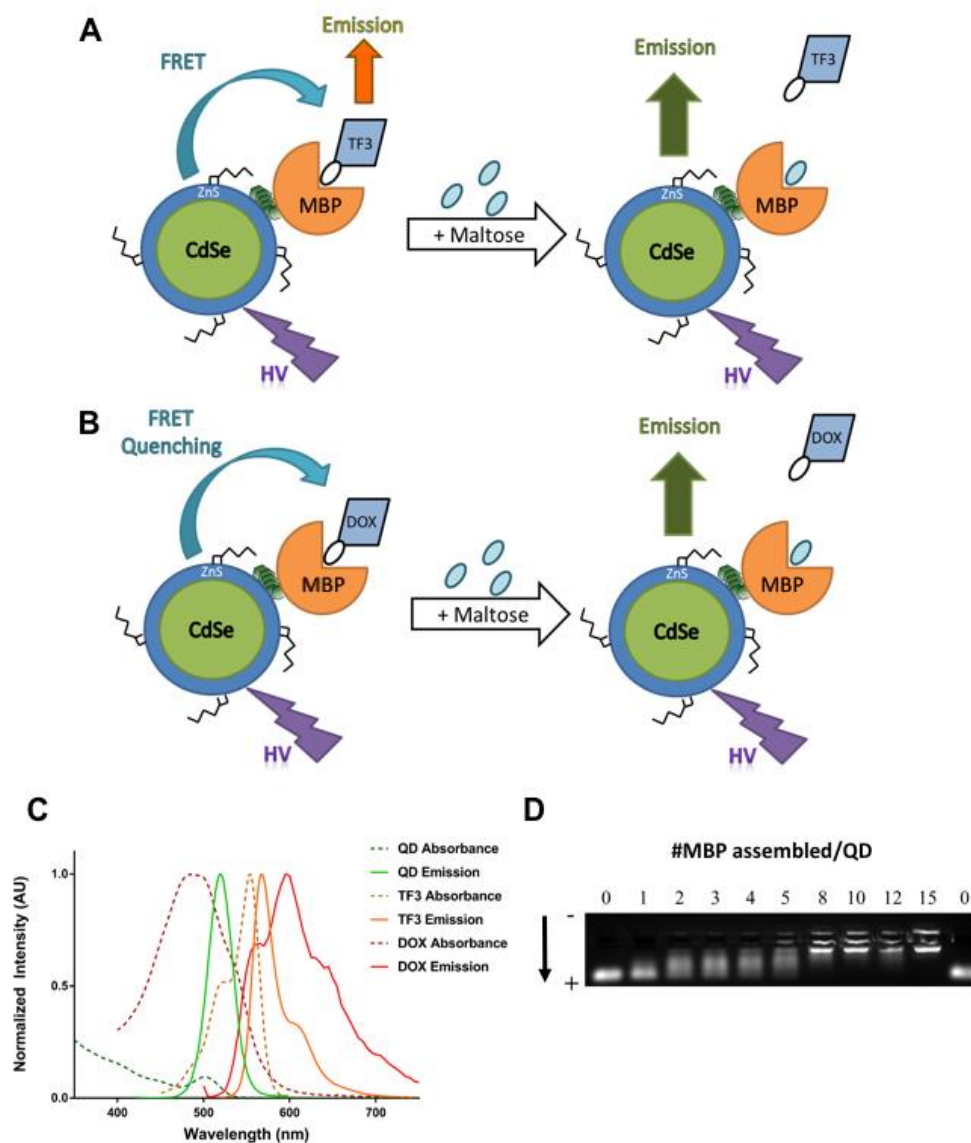


Figure 10. Design of QD-MBP- β CD-dye- and -drug conjugate systems. A) Schematic of the QD-MBP- β CD-TF3 actuation system. β CD-TF3 bound within the MBP binding pocket results in FRET-sensitized emission of the TF3 from the photoexcited QD donor. Addition of maltose displaces the β CD-TF3 resulting in re-emission of QD PL. B) Schematic of the QD-MBP- β CD-DOX actuation system. β CD-DOX in the MBP binding pocket results in quenched QD luminescence with minimal emission from DOX. Addition of maltose results in release of the β CD-DOX and re-emission of the QD donor. C) Absorbance and emission spectra for the 520 nm QD donor and TF3/DOX acceptors. Both the QD:TF3 and QD:DOX donor-acceptor pairs show significant overlap between the QD donor's emission and the acceptor absorption. D) 520 nm emitting QDs capped with CL4 ligands were assembled with increasing ratios of His₆-tagged maltose binding protein (MBP) as indicated and submitted to gel electrophoresis. Addition of increasing MBP/QD results in slower migration of the negatively-charged QDs towards the positive post.

the addition of maltose, there will be competitive displacement of the β CD-TF3 from the binding pocket, and so the TF3 peak will disappear and the QD peak will increase. Given that the doxorubicin will not produce a secondary peak, the visualization of release will be dependent on the change in QD peak alone. Once the maltose is added, the β CD-DOX will no longer be close enough to the QD to quench its emission and so the QD PL intensity will increase in response.

Given the ideal FRET donor properties of QDs, we utilized these particles as the NP scaffold and appended histidine-tagged MBP to the surface of the QDs. Into the MBP binding pocket was added the maltose analog β CD that was conjugated to TF3 or DOX. Once assembled, these constructs engage in FRET between the QD and the dye or DOX conjugates given the excellent spectral overlap of their absorbance with 520 nm QD donor emission (Figure 10C). The QD absorbance profile allows for excitation far in the UV, producing little direct excitation of the acceptor TF3 and the FRET can be further optimized by the addition of multiple donors per QD. It should be noted that DOX does not have a large molar extinction coefficient and so it acts merely as a quencher of the QD fluorescence, with no discernable QD sensitized emission from FRET¹²². To determine the efficiency of MBP assembly to the QD scaffold, gel electrophoresis was performed with increasing ratios of His₆ tagged MBP. The His₆ tag interacts with the Zn²⁺ present in the QD shell via metal affinity coordination, and assembly is rapid (complete within minutes) and has been shown to be stable for days in cellular environments⁹³. Figure 10D shows the decreased migration of QDs through the gel matrix as a function of increasing MBP:QD ratios. This analysis showed that maximal MBP loading of the QD surface was accomplished at a ratio of ~10 MBP:QD. Below a

ratio of 10 MBP per QD, a “smearing” pattern was seen and is indicative of a varied population of QDs which occurs when the number of proteins per QD, or valence, is assorted. Previous observations have shown this to be consistent with a Poissonian distribution at lower QD: protein valencies ⁷⁶. To produce the largest visualizable FRET signal and potential cargo loading, a ratio of 10 MBP per QD was chosen to use for all subsequent analysis.

Characterization of FRET Efficiency of QD-MBP- β CD Conjugates

To ascertain the utility of the QD-MBP- β CD conjugate system, we first confirmed and quantified the FRET efficiency of the fully assembled conjugates. Figure 11 A shows the resulting spectral traces collected from the QD-MBP- β CD-TF3 conjugate system where it was apparent that an increase in the number of MBP- β CD-TF3 assembled onto the QD surface resulted in a concomitant decrease in QD donor

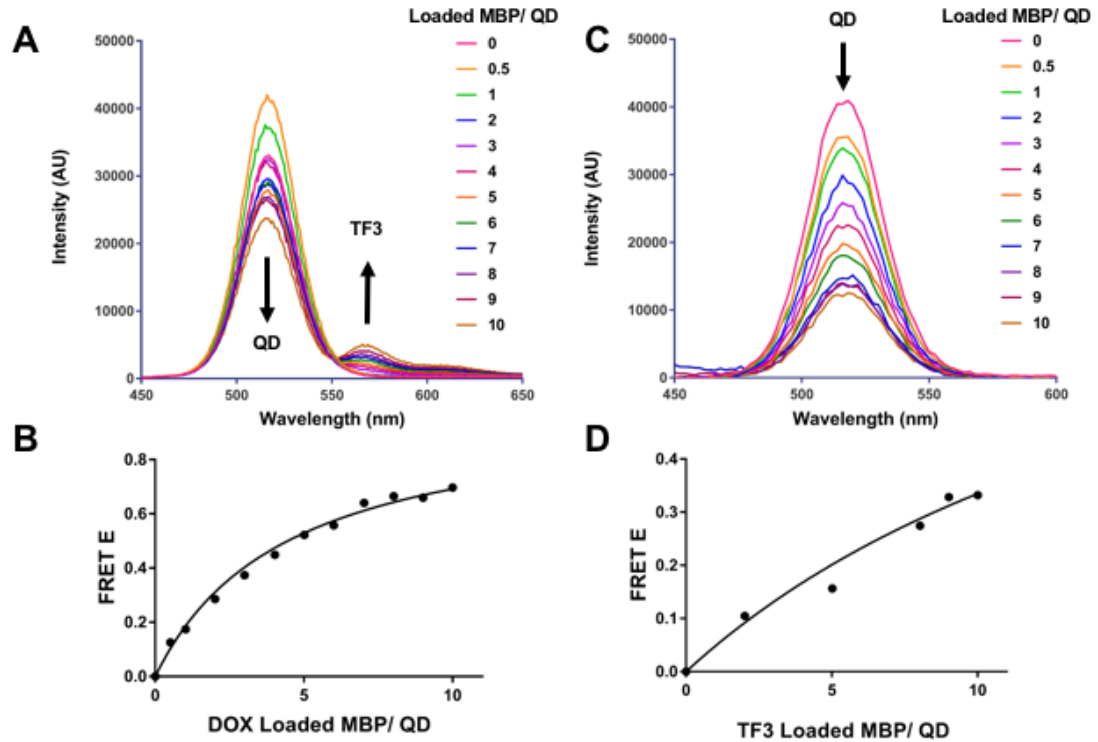


Figure 11: FRET analysis of the QD-TF3 and QD-DOX donor-acceptor pairs. A) Emission spectra of the QD-MBP- β CD-TF3 bioconjugates loaded with increasing MBP-TF3. Each spectra corresponds to the number of MBP-TF3 (loaded MBP) per QD and the balance of the QD surface (up to a ratio of 10 MBP) was made up with unloaded MBP. Spectra show decreasing QD PL and increasing TF3 PL that correlates with increasing loaded MBP per QD. B) Plot of the QD-MBP- β CD-TF3 FRET efficiency versus the number of loaded MBP per QD. Line is a fit to Eq 2 in Methods. C) Emission spectra of the QD-MBP- β CD-DOX system with increasing ratios of loaded MBP to unloaded MBP per QD show increasing QD PL that correlates to increasing loaded MBP. B) Plot of the QD-MBP- β CD-DOX FRET efficiency as function of number of loaded MBP per QD. Line is fit to Eq. 4 by using the calculated rDA values for each ratio and back-calculating what the corresponding FRET efficiency should be for that ratio of QD donor to acceptor.

luminescence coupled with an increase in the sensitized emission from the TF3 acceptor. Control experiments were performed to ensure that the passivation of the QD surface by His₆ binding was constant for each QD: MBP ratio (see Methods). Using these spectral data, the emission maxima for the donor and acceptor were plotted using Eq. 3 to determine the initial FRET efficiency at each QD:TF3 ratio. The R_0 (the QD-TF3 separation distance at which the FRET efficiency is 50%) for the QD-TF3 donor-acceptor pair was calculated using Eq. 1 to be 4.7 nm. These data were then analyzed using Eq. 4, which relates the FRET efficiency to R_0 to determine the calculated QD donor-TF3 acceptor distance (r_{DA}) for each ratio of QD:MBP- β CD-TF3. This equation takes into account the contribution of increasing numbers of acceptors, n , assembled onto the QD surface. As shown in Figure 11B, the FRET efficiency clearly tracked with the number of acceptor complexes arrayed around the central QD donor, with maximal FRET efficiency of ~33% obtained at a ratio of 10 MBP- β CD-TF3 per QD. Further, this analysis resulted in a calculated center-to-center QD to TF3 distance (β CD-TF3 within the MBP binding pocket) of ~7.8 nm.

Similar analysis was performed on the QD-MBP- β CD-DOX conjugate system. As evidenced by Figure 11C, the decrease in QD donor luminescence again tracked with increasing numbers of MBP- β CD-DOX acceptors arrayed around the QD. In contrast to the TF3 system, however, negligible photoluminescent reemission from the DOX acceptor was observed as a function of QD quenching. This is not surprising given the modest molar absorptivity of DOX and the dependence of DOX-histone interactions on DOX emission¹²³. Nevertheless, DOX clearly quenched the QD donor in a ratiometric, dose-dependent fashion. Analysis of the FRET efficiency as a function of the number

acceptors revealed a considerable difference in the calculated center-to-center distances for the QD-DOX system compared to the QD-TF3 donor-acceptor pair. The separation distance for the QD-DOX pair was ~4.3 nm, which is ~3.5 nm shorter than that determined for the QD-TF3 pair. In this instance, it is likely that flexible carbon spacer (linear length ~ 1.4 nm) could allow the DOX to extend back to the β CD. This fact, coupled with the amphiphilic nature of DOX ¹²⁴ and the role of the β CD as an efficient host for amphiphilic cargos (including DOX) ¹²⁵, presents the possibility that the DOX associates with the β CD in a guest-host configuration despite the physical link; which would bring the DOX closer to the QD surface, resulting in the shortened separation distance observed here.

Determination of Actuation Efficiency of QD-MBP- β CD Conjugates by Plate-based Assay

Having successfully demonstrated that the QD bioconjugates engage in efficient FRET, we next determined the temporal responsivity and sensitivity of the QD-MBP- β CD-conjugates to the addition of maltose. To do this, microplate-based assays were performed in which MBP was first loaded with the each respective β CD conjugate (at a ratio of 1:5 MBP: β CD conjugate) to ensure complete loading of the MBP protein. Then, the loaded MBP proteins were assembled with QDs (1:10 QD:MBP) to form the full ensemble conjugates wherein the photoexcited QD donor was engaged in FRET with either the TF3 or DOX acceptor. Replicate wells of the microplate were loaded with the assembled complexes and the system was excited at 400 nm to excite the QD donor while

spectra were collected (data not shown). This served as an internal reference control to ensure that all of the replicate wells yielded uniform peak intensities prior to maltose addition (“unactuated” state). Maltose was then added to the wells such that the final maltose concentration ranged from 50 nM to 20 mM. Immediately after delivery the spectra were again collected over the same range. Figure 12 A shows the resulting spectra for the response of the β CD-TF3 system to the addition of increasing concentrations of

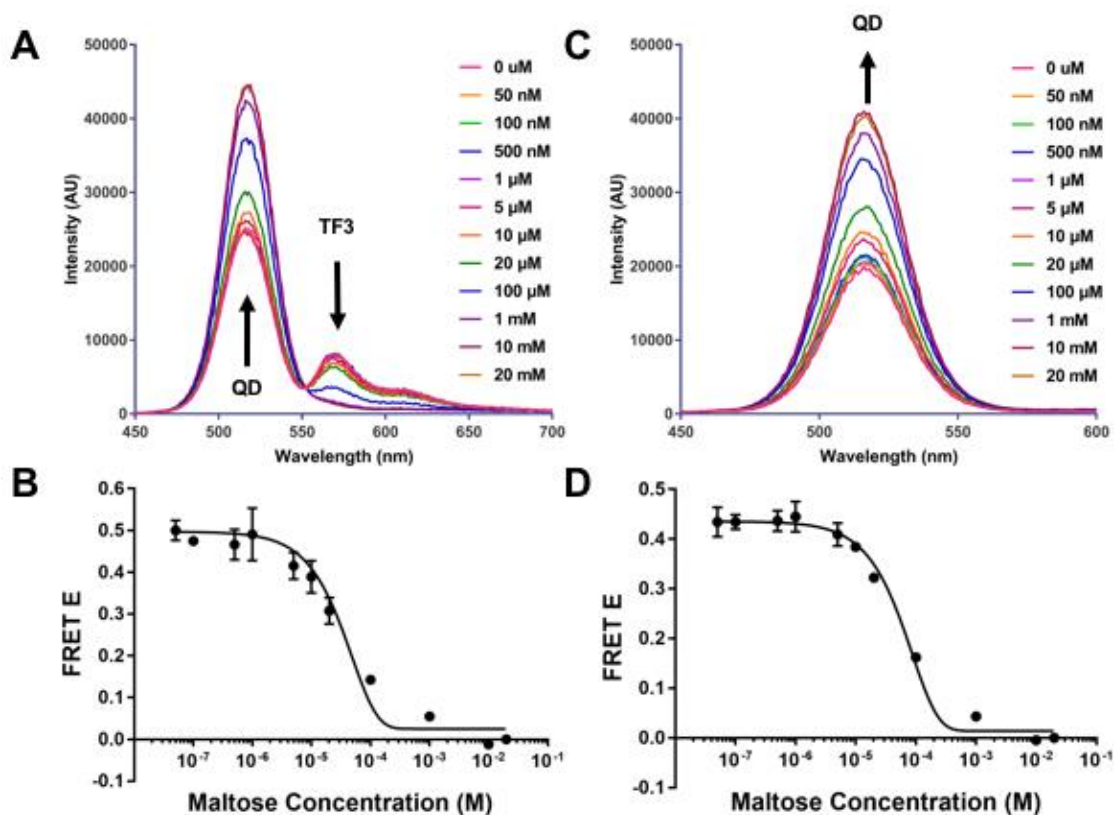


Figure 12: Responsiveness of QD-MBP- β CD-TF3/DOX systems to the addition of maltose. A) Emission spectra of the QD-MBP- β CD-TF3 complexes after addition of increasing concentrations of maltose. Displacement of the β CD-TF3 results in increasing QD PL and decreasing TF3 PL that tracks with increasing maltose concentration. B) Plot of the QD-MBP- β CD-TF3 FRET efficiency versus maltose fit to a sigmoidal binding isotherm. C) Emission spectra of the QD-MBP- β CD-DOX complexes after addition of increasing concentrations of show increasing QD PL that correlates to increasing maltose concentration. B) Plot of the QD-MBP- β CD-DOX FRET efficiency as a function of maltose concentration. Curve is fit to sigmoidal binding isotherm analysis function from GraphPad Prism.

maltose. There was a clear increase in QD emission and decrease in TF3 luminescence that tracked with the increasing maltose concentration added to the well. This provided strong evidence of the competitive displacement of the β CD-TF3 conjugate from within the MBP binding pocket by the exogenous maltose. The calculated FRET efficiency, when plotted as a function of concentration (Figure 12 B) resulted in an apparent binding dissociation constant (K_d) of $\sim 10 \mu\text{M}$, consistent with values reported in the literature ¹²⁶⁻¹²⁸. Comparable results were obtained with the maltose concentration-dependent studies on the QD-MBP- β CD-DOX conjugate. Here, only increased QD emission was observed, but the fit of the data to the binding isotherm resulted in a similar K_d value for that determined for the TF3 system. Collectively, these data gave us great confidence that not only did both systems engage in efficient FRET, but that the release of the β CD-TF3 or -DOX cargo could be efficiently achieved by the simple addition of maltose.

Intracellular Actuation of the QD-MBP- β CD Conjugate System

In this study, our working hypothesis was that the self-assembled, multi-component QD-MBP- β CD conjugate system could be introduced into the cytosol of cells and that the release of the appended cargo could be discretely controlled by the simple addition of exogenous maltose to the extracellular media. In this configuration, native sugar transporters resident in the plasma membrane transport the extracellular maltose into the cytosol where it induces the release of the β CD-conjugate from the MBP binding pocket. Our initial characterization showed that the conjugate system engaged in efficient FRET and that β CD-conjugate release could be induced by maltose in a concentration-dependent manner (*vide supra*). We next assessed the efficiency of the QD-MBP- β CD

conjugate system to be actuated by the addition of maltose. To do this, we first confirmed that the complexes engaged in stable FRET in the cellular cytosol upon microinjection (Appendix Figure A2). This was accomplished by performing photobleaching studies on the QD-MBP- β CD-TF3 conjugates after injection into the cytosol. Spectral imaging of the complexes prior to photobleaching showed significant sensitized emission from the TF3 acceptor coupled with QD donor quenching. After bleaching of the TF3 acceptor by direct excitation with 561 nm laser, however, significant increased emission of the QD donor was observed. These data clearly demonstrated that the bioconjugate system engaged in FRET in the cytosol.

Next, we characterized the time-resolved responsiveness of the QD-MBP- β CD-TF3 system to the addition of extracellular maltose. COS-1 cells were microinjected with the assembled complexes and initial imaging was performed to collect the baseline spectra. As expected, upon injection the complex was initially engaged in FRET, as evidenced by the strong yellow emission in the spectral image which is indicative of QD-sensitized emission from the TF3 acceptor (Figure 13A). Maltose (20 mM final concentration) was then added to the extracellular medium and spectral imaging was performed at two minute intervals over a 30-minute period. This maltose concentration was selected as membrane glucose transporters, the putative transporters for maltose, exhibit K_d for glucose of ~ 15 -20 mM¹²⁹⁻¹³⁰. After the addition of maltose, spectral imaging was performed every two minutes over a 30-minute window to monitor the change in FRET of the complex as a function of time as maltose was internalized into the cytosol. Indeed, analysis of the spectral traces confirmed the time-resolved decrease in

FRET as an ~35% increase in QD donor emission was observed concomitantly with an ~15% decrease in sensitized emission from the TF3 acceptor (Figure 13B). Control experiments wherein the FRET efficiency of the injected complex was monitored over this same 30-minute window without the addition of maltose showed negligible change in the QD/TF3 channels, demonstrating both the stability and responsivity of the complex in

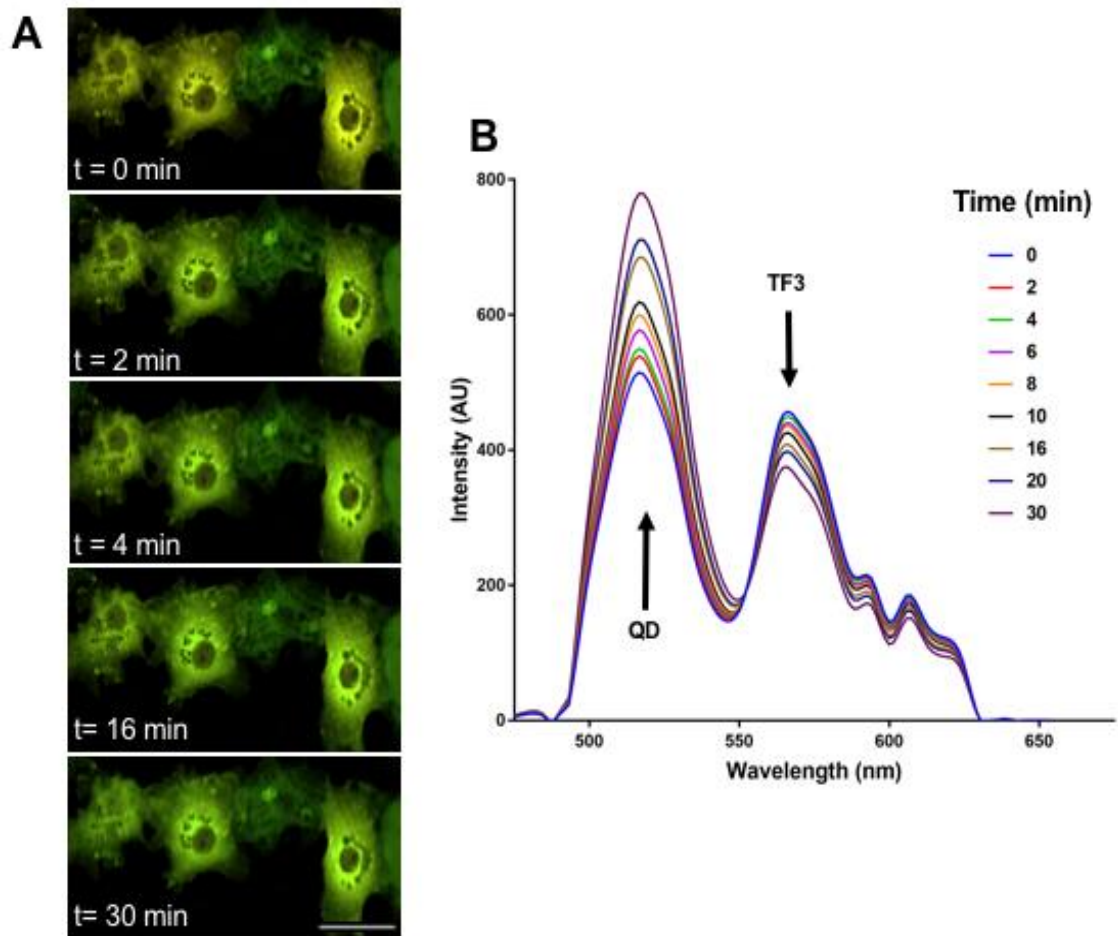


Figure 13: Response of intracellular QD-MBP- β CD-TF3 to maltose addition. A) COS-1 cells injected with QD-MBP- β CD-TF3 were imaged in spectral mode (10 nm bins from 480 nm to 650 nm) using confocal microscopy. After initial image collection at t=0, maltose was added to the cell media to a final concentration of 20 mM. Images were taken every two minutes for 30 minutes. Panel shows the gradual color change from yellow at t = 0 min to green at t = 30 min, indicating decreased sensitization of the TF3 acceptor after displacement by maltose. Scale bar is 20 μ m. B) Spectral data corresponding to the cells in (A). A time dependent increase in QD PL is observed.

the cellular cytosol. These data confirmed the time-resolved responsiveness of the QD-MBP- β CD-TF3 system to the addition of extracellular maltose.

Having demonstrated the utility of the intracellularly introduced QD-MBP- β CD-TF3 bioconjugate system to respond to extracellular maltose, we next sought to perform a more quantitative analysis of the responsivity of the bioconjugate assembly as a function of both maltose concentration and time. Spectral imaging was performed on COS-1 cells loaded with the conjugate system in the cytosol. The cells were incubated with discrete concentrations of extracellular maltose (over a concentration range spanning 1.25 mM to 30 mM maltose) and spectral imaging was performed over a 30 minute operational window. The data are shown graphically in Figure 14A where the change in the QD

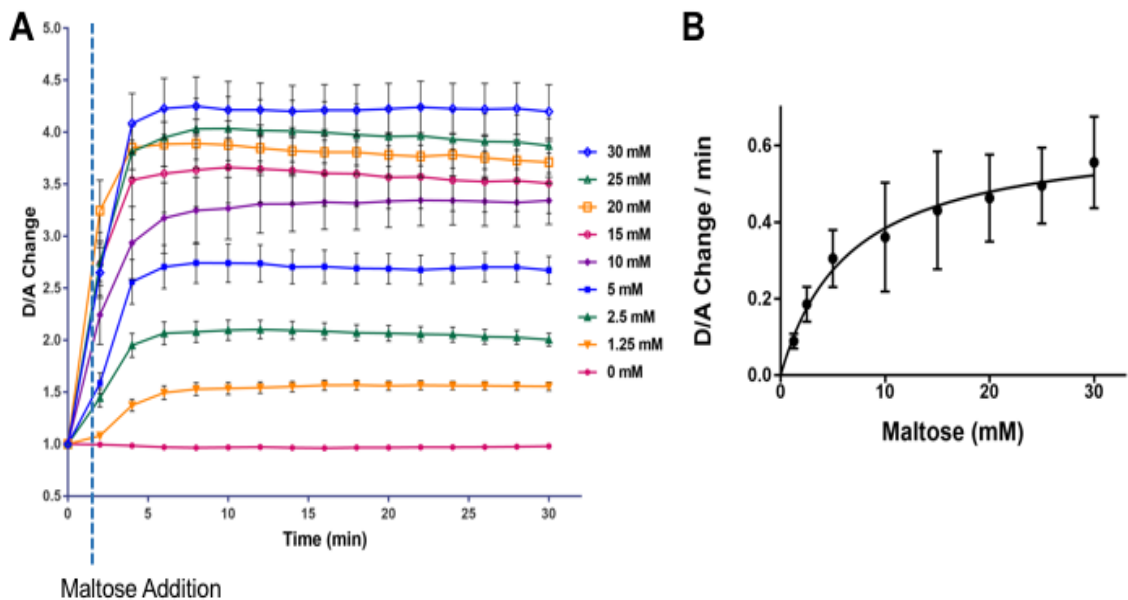


Figure 14: Time-resolved response of intracellular QD-MBP- β CD-TF3 to addition of extracellular maltose. A) Separate dishes of plated COS-1 cells were injected with QD-MBP- β CD-TF3 conjugates and then increasing concentrations of maltose were added. Spectral images were collected over 30 min. Plotted are the ratio of QD donor/TF3 acceptor peak height as a function of time. Data show that the β CD-TF3 is released quickly from the MBP binding pocket and is complete within ~6 min across all maltose concentrations. B) Plot of the calculated initial rate of response ($t=0$ to $t=4$ min) vs maltose concentration. Data are fitted with one site binding model shown in appendix Figure A3.

donor/TF3 acceptor PL emission ratio in response to extracellular maltose are plotted as a function of time. For each increasing concentration of maltose, a clear dose-dependent increase in the QD donor/TF3 acceptor PL emission ratio was observed. Notably, the slope of the initial rates of change in QD/TF3 emission ratio tracked positively with increasing maltose concentration and, within each maltose concentration, maximal displacement of the β CD-TF3 ligand was achieved in ~6 min. It is also important to note the inherent stability of the assembled complex, for in the absence of added maltose, there was negligible change observed in the QD/TF3 emission ratio. When the initial rates were plotted versus maltose concentration and fit to a one-site binding model (Appendix Figure A3), a calculated K_d of ~6.5 mM for the internalization of maltose was determined (Figure 14B). This value agrees well with that reported in the literature for the intracellular transport of maltose¹²⁹⁻¹³⁰. It is important to note that the K_d calculated for this system is an apparent K_d that includes both the rate of maltose internalization and the rate of release of the β CD-TF3 from the binding pocket of the MBP. The experimental setup does not allow for the contributions of each rate to be determined, but given how quickly each of the concentrations reaches their final values, it can be hypothesized that the limiting factor is the cells' ability to internalize maltose. This makes sense as the cells want to maintain a certain osmolarity and the rapid internalization of maltose would eventually be slowed to ensure that the cells remain viable. Fluorescence lifetime imaging confirmed that the assembly was engaged in FRET as the QD donor exhibited a ~20 % decrease in fluorescence lifetime in the intact bioconjugate. However, upon addition of 30 mM maltose, and displacement of the β CD-TF3 moiety, the QD lifetime returned to that measured for the QD alone in the cytosol

(Appendix Figure A4). Cumulatively, these data demonstrate the ability of the QD-MBP- β CD-TF3 bioconjugate system to serve as a robust actively triggered actuation modality that responds to extracellular maltose in a manner that is consistent with the known affinity of membrane transporters for the sugar.

Building on the demonstrated utility of the QD-MBP- β CD-TF3 system to be triggered by extracellular maltose, we next sought to use the conjugate system to deliver DOX, a potent chemotherapeutic whose delivery must be tightly controlled to avoid off-target tissue toxicity. The QD-MBP- β CD-DOX system presents a few variations from the TF3 system such that the experimental approach had to be slightly modified. First, because the DOX acceptor is minimally emissive, spectral imaging allowed the monitoring of the DOX channel only. Second, because DOX-induced toxicity has been shown to result in changes in cell/nuclear size⁴⁰ that could potentially affect QD PL, red-emitting (655 nm) QDs were co-injected into the cytosol along with the QD-MBP- β CD-DOX complexes. In this way, the 655 nm QDs served as a cross-channel internal imaging control.

In similar fashion to the β CD-TF3 system, the QD-MBP- β CD-DOX system also showed a similar time-dependent re-emission of the QD donor when 20 mM maltose was added to the media (Figure 15A). Importantly, the 655 QD imaging control showed no change in its luminescence, confirming that the observed increases in QD PL were due to maltose-induced displacement of the β CD-DOX moiety from the MBP binding pocket.

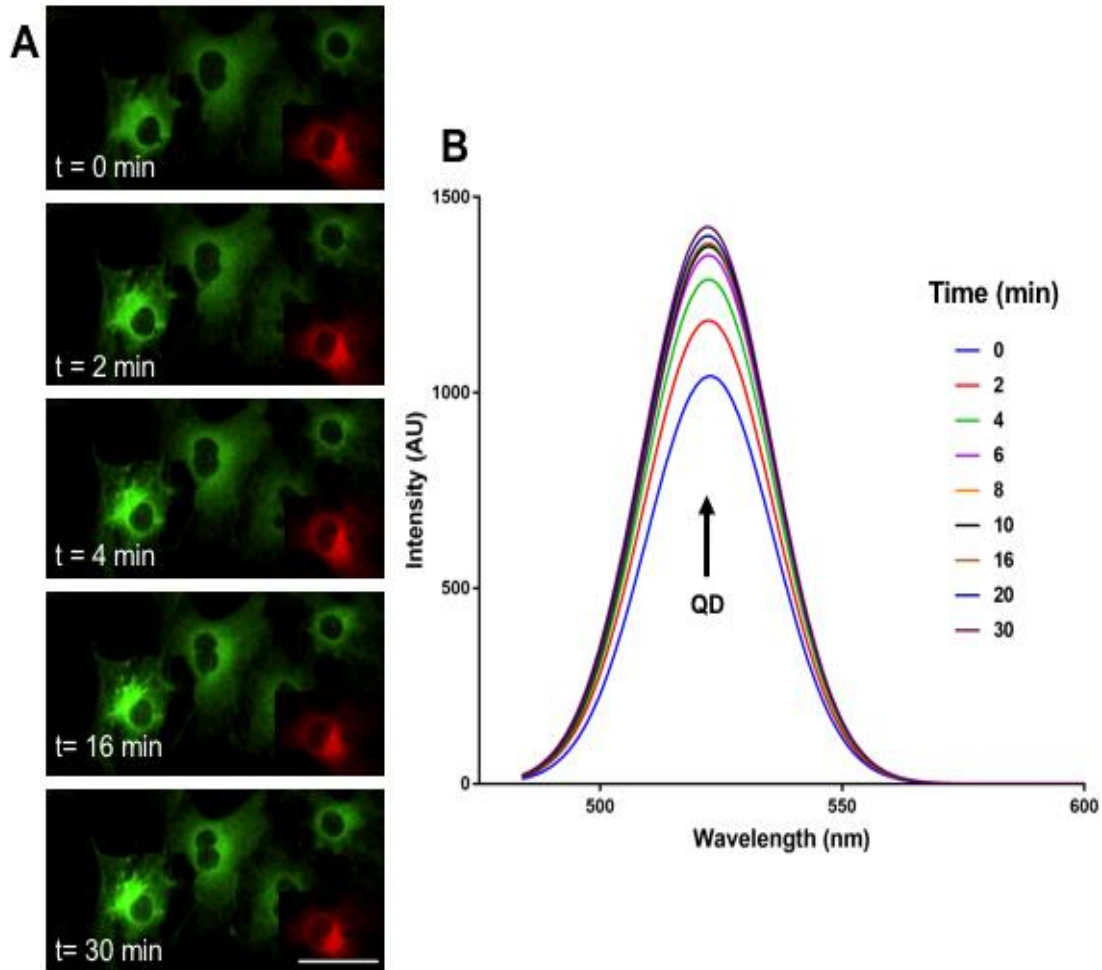


Figure 15: Response of intracellular QD-MBP-βCD-DOX to maltose addition. A) COS-1 cells injected with QD-MBP-βCD-DOX conjugates were imaged in spectral mode using confocal microscopy. After initial image collection at t=0, maltose was added to the media (final concentration 20 mM). Images were taken every two minutes for 30 minutes. Panels show the progressive increase in QD PL over the 30 min window, indicating the maltose-induced release of the βCD-DOX from the MBP binding pocket. Inset in each panel shows the emission intensity for the 655 nm QD imaging control for a cell outside the current view. Scale bar is 20 μm. B) Spectral data corresponding to the cells in (A). A time dependent increase in QD PL is observed.

A time-resolved plot of the rate of donor QD PL recovery showed the displacement of the βCD-DOX from the MBP is rapid, occurring within 10 minutes with a calculated K_d for the intracellular transport of maltose of ~1.1 mM which agrees well with that determined for the βCD-TF3 system, but is also an apparent K_d for the system, and could vary

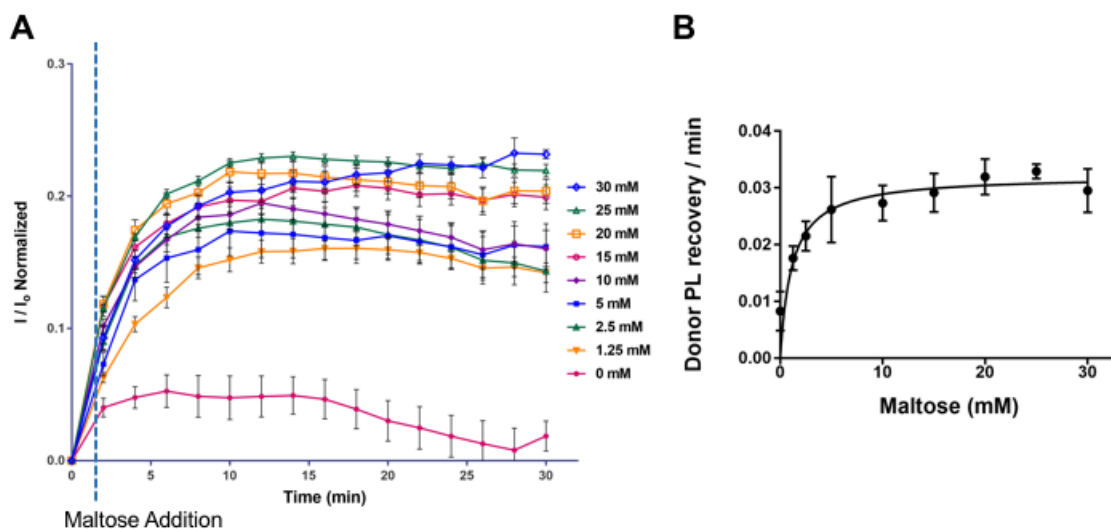


Figure 16: Time-resolved response of intracellular QD-MBP- β CD-DOX to addition of extracellular maltose. A) Increasing concentrations of maltose were added to replicate seeded plate of COS-1 cells that were injected with QD-MBP- β CD-DOX conjugates and then increasing concentrations of maltose were added and spectral imaging was subsequently performed at 2 min intervals over a 30 min period. Plotted are the calculated FRET E using Eq. 3 normalized to the initial timepoint. (I/I_0) B) Plot of the calculated initial rate of response ($t=0$ to $t=4$ min) vs maltose concentration. Data are fitted with one site binding model shown in appendix Figure A3.

slightly due to the β CD-DOX binding to the MBP in a less-efficient manner than the β CD-TF3 (Figure 16B). This was also confirmed by FLIM imaging where the quenched lifetime of the QD donor in the intracellular QD-MBP- β CD-DOX complex (~15%) was recovered after the addition extracellular maltose (Appendix Figure A4). Interestingly, there was a modest degree of release of the β CD-DOX moiety in the absence of added maltose, suggesting subtle differences in the way the β CD-DOX interacts with MBP binding pocket compared to the β CD-TF3 conjugate. It is likely that the amphiphilic nature of DOX, coupled with the flexible linker bridging the β CD and DOX, promotes guest-host interactions between the β CD and DOX that result in a lower-affinity interaction of β CD-DOX with MBP. Further supporting evidence for the altered activity of DOX in the β CD-DOX conjugate come from control studies of its nuclear uptake

compared to free DOX (Appendix Figure A5). While free DOX localized efficiently within the nucleus, β CD-DOX accumulated at the nuclear membrane, providing evidence that conjugation to β CD altered its innate nuclear uptake and DNA-binding properties.

Conclusions

The data presented here provide strong evidence of the utility of the novel actively-triggered self-assembled QD-based drug delivery system. The actuation modality is driven by the simple addition of an inert triggering molecule, maltose, to the extracellular environment. The multiple parts of the NP-bioconjugate system are easily assembled and the ensemble conjugate is directly introduced to the cytosol by microinjection, which bypasses the endolysosomal system, and allows for direct assessment of the system's responsiveness to the addition of the maltose to the extracellular media. The system responds in a dose- and time-dependent manner to affect the release of both dye- and drug-conjugates of β CD with similar release profiles observed for both ligand systems. FRET-based imaging allows for the real-time tracking and characterization of maltose-induced ligand release. This novel actuation modality has the benefit of not being dependent on light-mediated stimulation (which has limited tissue penetration) or the use of bulky, dedicated equipment (*e.g.*, magnetic field, radiofrequency) in a centralized facility. Future work could explore the potential range of sizes that the system could transport and also modify the binding efficiency of the bridging protein- potentially producing a variety of release rates specific to the desired target. This new method opens a new area of NP-mediated drug delivery.

Chapter 4: Design and Implementation of an Extracellular pH Sensor

Introduction

Cancer accounted for over half a million deaths in the United States of America in 2014, making it the second leading cause of death in the country ¹³¹. As cancer is defined as the uncontrolled growth of abnormal cells in a part of the body, any cell type can become cancerous - making a singular 'cure for cancer' a near impossibility. Initiation of abnormal cell growth is caused by the mutation of DNA in two types of specific genes, tumor suppressor genes (genes whose loss 'turns on' cancerous growth through inhibition loss) and oncogenes (genes that, once mutated, cause cancer) ¹³². As there are numerous possibilities for these types of mutations, the cancer present in one individual can be almost unique when compared to another's cancerous cells. However, there are some commonalities between almost all cancer types, the most well-known of which being tumor formation - where a large centralized conglomeration of abnormal cells grows in an uncontrolled manner ¹³³. These tumors can be benign, where they do not release cells into the bloodstream to form secondary tumors, or malignant, where cells traverse the body and form many secondary smaller tumors. Tumors commonly modify their extracellular environment to better suit their prolific growth. First, tumors excrete vascular endothelial growth factor (VEGF) that stimulates the formation of new vasculature to the tumor site therefore increasing the blood supply to the tumor site ¹³⁴. The vasculature in the tumor environment also displays what is called the EPR effect, where there is an enhanced perfusion and retention within the tumor locale ¹³⁵. Many drug delivery mechanisms attempt to take advantage of this leaky vasculature, where they assume that their delivered agent 'targets' the tumor simply because it spends more time

in the tumor location and can more easily extravasate across the epithelium¹³⁶. One other prominent feature of the tumor microenvironment is their lower pH compared to normal physiological conditions. Tumors can have pH microenvironments as low as pH 5, which is significantly lower than the 7-7.4 pH seen in healthy tissue⁹⁵. Measurement of the pH in the extracellular tumor environment could assist in the design, implementation and monitoring of more targeted release agents. However, this is not something easily achieved with currently available techniques as described in the following section.

Current pH Sensors

Many common pH sensors that are used in cellular applications focus on the change that occurs within the endolysosomal internalization process. As vesicles are shuttled from the cell surface, the pH within those vesicles gradually lowers to reach a final pH of 5 within the lysosomes. Commercially available sensors like pHrodo™ proprietary dyes, available from ThermoFisher, are designed to be internalized and increase in intensity as the pH of their environment decreases. This is a ‘turn on’ type of measurement that makes it difficult to quantifiably measure the actual pH of the environment. The sensor 2',7'-bis-(2-carboxyethyl)-5-(and-6)-carboxyfluorescein (BCECF, ThermoFisher) can give a more precise pH measurement but requires the sample to be excited at both 440 nm and 490 nm wavelengths, which is difficult on most microscopes. As mentioned in the Introduction, many labs use the pH-responsive properties of FITC in the design of pH sensors. Fluorescein exhibits pronounced pH dependent absorption and fluorescence features due to its intrinsic multistage protonated/deprotonated forms; as pH lowers, the lowest absorption band shows a

hypochromic shift while the fluorescence intensity concurrently decreases as well ¹³⁷⁻¹³⁸. Xu *et al.* used FITC and the pH-unresponsive dye Ru(phen)₃²⁺ as a ratiometric pH indicator by encapsulating the Ru(phen)₃²⁺ within silica particles decorated with covalently-bound FITC. This complex produced a single-excitation (450 nm) measurement system that displays a change from green to red during internalization in SMMC-7721 hepatoma cells ¹³⁹. Other pH-responsive systems have been designed using alternative fluorescent molecules as the monitoring component for intracellular pH sensing systems. The Parak Lab produced polyelectrolyte microcapsules loaded with pH-responsive SNARF-1-dextran that could be internalized and showed a change from red fluorescence in alkaline cell media to a green fluorescence in the acidic endosomal environment of MDA-MB435S breast cancer cells ¹⁴⁰. Dennis *et al.* used a GFP analog called mOrange that was appended onto a 525-nm emitting QD for a FRET-based intracellular pH sensor, and after internalization in HeLa cells the intensity of the mOrange decreased in response to the lowering of pH. This system produced PL changes across a dynamic range between pH 6 and 8, and was designed to overcome some of the limitations in imaging fluorescent probes over long periods of time (*i.e.* photobleaching)⁸⁷.

While there are a wide variety of intracellular pH sensors, there are very few sensors that are specifically designed for extracellular pH sensing. One method utilizes amphiphilic lipid-DNA molecules labeled with one of two fluorescent molecules, a green pH sensitive dye fluorescein (FAM) and an orange pH insensitive dye carboxytetramethylrhodamine (TAMRA) which can be co-localized with the extracellular leaflet of the membrane due to the lipid component of the two dye probes. This system,

however, is limited by the FAM's responsive range, which is very close to that of FITC given their structural similarities, and so the dynamic range that can be measured is only from pH 6-8. This system uses direct excitation of the FAM and so is very susceptible to photobleaching which is problematic for long-term tumor microenvironment studies ¹⁴¹. Another extracellular pH sensing approach does not focus on labeling the cellular membrane, per se, but rather on developing a blood-stream circulating sensor that uses red blood cell ghosts loaded with the FITC. The ghosts equilibrate quickly to the extracellular blood pH using the chloride-bicarbonate exchanger inherent in their cell membranes. This produces a sensitive system that has potential to act as a long-term blood sensor ¹⁴². This system travels rapidly throughout the body with blood flow, however, and so would give an overall measurement of the pH and will not be able to specifically measure a singular location with high precision. Our study attempts to overcome some of these limitations by using a new FRET-based sensor design combining a QD donor, a pH-responsive dye, and a unique peptide that labels the cellular membrane with a high degree of accuracy.

JB858: A Unique Membrane-Labeling Peptide

We have previously published work using short peptide sequences and their effect on the localization of QDs after delivery. The original peptide in those studies was shown to have promising results in delivering palmitoyl-protein thioesterase 1 (PPT1) inhibitors to neurons ¹⁴³⁻¹⁴⁴. These inhibitors are particularly of interest as they are chaperones in infantile Batten disease. This peptide, called JB577, has the following sequence: WG(Dap^{Pal})VKIKK(P₉)GG(H₆). Modifying the palmitoyl (Pal) linker from a

diaminopropionic acid (Dap) to a diaminobutyric acid (Dab), which amounts to the addition of one methyl group between the peptide backbone and the palmitoyl, yielded a very different functionality for the peptide. The sequence of the new delivery peptide, dubbed JB858, is WG(Dab^{Pal})VKIKK(P₉)GG(H₆), where the palmitoyl group is anchored to a Dab residue by a nonhydrolyzable amide linkage. The His₆ QD-coordination sequence is followed by the Gly₂ flexible linker and the Pro₉ motif. The Pro₉ is expected to form a rigid type II helix to help the (Dab^{Pal})VKIKK segment extend out beyond the surrounding PEG layers on the QD surface. The positively-charged VKIKK motif is supposed to mediate electrostatic interactions with cellular membranes while the palmitoyl group is thought to insert into the membrane allowing the QD to remain membrane-bound. Cells labeled with QDs conjugated with JB858 preferentially localized to the cellular membrane over the studied time periods (up to 48 hours). This prolonged labeling is ideal for live-cell monitoring of the extracellular pH.

In this study, we utilize one of the least developed areas of the visible fluorescence range (below 500 nm) for QD materials and tap into their potential for FRET-based pH sensing. The hydrophobic 464 nm emitting QDs synthesized for this purpose were modified by ligand exchange with compact hydrophilic ligands to evaluate the biocompatibility of the QDs for biological sensing and imaging studies. These water-soluble blue-emitting QDs exhibited reasonably high QYs (20-30%), narrow photoluminescence bands, and excellent pH and salt stability¹⁴⁵. Conjugating these nanocrystals with the pH-responsive FITC produces a FRET-based nanoscale pH sensor, as the QD emission profile overlaps the FITC's absorption profile. Fluorescein itself is highly susceptible to photobleaching and so using the molecule alone would not produce

a robust sensing system, but using the aforementioned blue QDs as a FRET donor will offer some protection to FITC molecules attached to the QDs as they can be sensitized during signal transduction and not directly excited. This QD-FITC sensing system can label cells using the JB858 peptide, producing an extracellularly localized pH sensor that has a dynamic range specific to that commonly seen in tumor microenvironments. Additionally, this system is reproducible and comparison to a standard titration curve can correctly identify the pH of an unknown buffer within 3% of the measured pH.

Experimental

QD-FITC Coupling and pH Sensing Assay

Typical reaction conditions used were as follows: 464 nm emitting QD coated with DHLA-PEG₇₅₀-OMe:DHLA-PEG₆₀₀-NH₂ (4:1) (12.0 μM, 250 μl, 3.0×10^{-9} mol) was mixed in 500 μl of 0.1 M NaHCO₃/Na₂CO₃ buffer (pH 9). The DHLA-PEG₆₀₀-NH₂ was used to conjugate the FITC to the QD surface. The specific synthesis of these QDs is described in ¹⁴⁵ and to conjugate FITC to the 464 nm QDs, a FITC solution (3.41 mM in DMSO, 18 μl, 6.1×10^{-8} mol) was added to the QD solution to initiate the reaction. After gentle stirring for 7 h in the dark at room temperature, the mixture was directly loaded onto a PD-10 desalting column (GE Healthcare Life Sciences) and eluted with 0.1× PBS ¹⁴⁶. Elution of the QD product (band) was traced by hand-held UV lamp. The first emitting single band was collected and transferred to a centrifugal purification unit (Amicon Ultra 30K, Millipore). The product solution was diluted with DI water and centrifuged at 3800 rpm for ~5-10 min, and the filtrate was discarded. The concentrated

QD solution was used for subsequent pH sensing experiments. Buffer solutions used are as follows: 0.1 M AcOH + 0.1 M NaOAc for pH 3-6; 50 mM Tris + HCl for pH 6.5-9.

Cell Culture and Cytotoxicity Test

African-green monkey kidney cells (COS-1) were maintained in complete growth medium (Dulbecco's Modified Eagle's Medium (DMEM; American Type Culture Collection (ATCC)) supplemented with 10% (v/v) heat inactivated Fetal Bovine Serum (FBS; ATCC) and 1% (v/v) antibiotic/antimycotic solution (Sigma-Aldrich) at 37 °C and 5% CO₂. The cells were cultured in T75 flasks under a humidified atmosphere and passaged at 80% confluency.

The water-soluble QDs were conjugated to the membrane localization peptide JB858¹⁴⁷ by incubating the assemblies at a QD:peptide ratio of 1:30 in DMEM supplemented with 25 mM HEPES (DMEM/HEPES, pH 7.4; Life Technologies, Carlsbad, CA). To ensure that no aggregation occurred in response to the incubation, each component was mixed following a specific protocol. First, the peptides were suspended in DMSO, and the DMSO solution was further mixed with DMEM/HEPES buffer so that the final DMSO concentration was 5 % (v/v). Second, the QDs were added to the peptide solution, vortexed, and allowed to incubate for 30 minutes; after which the solution was spun briefly to ensure that no aggregation had occurred. The final concentration of the QDs were 500 nM. For cytotoxicity analysis, cellular proliferation was analyzed using the CellTiter 96® AQueous One Solution Cell Proliferation Assay (Promega, Madison, WI) by following the manufacturer's prescribed instructions. The assay is based upon the conversion of a tetrazolium substrate to a formazan product by

viable cells at the assay end point. Briefly, 96-well plates were seeded with $\sim 2 \times 10^3$ cells/well and allowed to incubate overnight. The cells were then exposed to increasing concentrations of the QDs for 30 min in DMEM/HEPES. The solutions were removed, the cells were washed with DMEM/HEPES, and replaced with complete media. The cells were cultured for further 48 hours before performing the assay. A control of DMEM delivery was performed to standardize the results, and media alone was used as a blank control.

QD-FITC Delivery to Cellular Membranes Using Peptide JB858

For QD-FITC delivery and attachment to cellular membranes, 14 mm dishes (MatTek Corporation; Ashland, MA) were seeded with $\sim 2 \times 10^5$ cells per dish and allowed to incubate overnight. The QD-FITC conjugates were assembled with the membrane targeting peptide JB858 by incubating the conjugates at a QD:peptide ratio of 1:40 in DMEM/HEPES. The final concentration of the QDs and JB858 were 200 nM and 8 μ M, respectively. The QD-FITC-JB858 assemblies were incubated on pre-washed cells for 30 minutes, washed, and the media was changed to Dulbecco's phosphate-buffered saline (DPBS) ¹⁴⁷.

Acquisition and Image Analysis of Extracellular pH Sensing

The cells were subsequently imaged on a Nikon A1RSi confocal microscope using spectral acquisition from 440 to 625 nm binned over 5 nm. A 405 nm laser was used to excite the sample in the same manner as normal confocal microscopy, and the emission beam from the sample was then polarized and sent through a diffraction grating

cassette which was set at 5 nm resolution. The output was then focused onto a 32 photomultiplier tube (PMT) array which acquires the output from each of the 5 nm bins and produces images and intensity data. The resulting image is a compilation of each of the wavelengths and provides intensity data for each specific wavelength bin. To explore pH effects on the fluorescent profiles of the QD-FITC conjugates attached to the cell membranes, the cells were iteratively incubated in buffers of decreasing pH values. In between each media exchange the cell monolayers were washed twice. After each image was taken, multiple regions of interest (ROI's) were chosen at centers on the membrane and the spectral intensity data were exported into Excel for analysis. Images were processed using Nikon Elements 4.50.00. As a control, the same QD-FITC conjugates were assembled with JB858 at a QD:peptide ratio of 1:15 in DPBS with each desired pH, and the fluorescence spectra of each sample were measured using the Tecan microtiter plate reader.

Results and Discussions

Ligand Exchange to Produce Biocompatible Blue-Emitting QDs

Directly following synthesis, the ZnSe/Cd_xZn_{x-1}/ZnS multishell QDs, where the Cd is ratiometrically exchanged with Zn ions (to produce x amount of Cd and x-1 of Zn), are coated with their native hydrophobic surface ligands¹⁴⁵. For use in biological applications, they must be made colloiddally stable for use in aqueous environments. The as-prepared QDs were further modified *via* ligand exchange with hydrophilic ligands to demonstrate that they are both compatible with common surface modification techniques and can be stable in aqueous media without significant deterioration of their intrinsic

photophysical properties. The surface ligand used for this study is a poly(ethylene glycol) (PEG) appended thiolated ligand DHLA-PEG₇₅₀-OMe⁶⁹, and a pre-metallation method was adopted for ligand exchange¹⁴⁸. We, along with many other groups, have previously demonstrated that DHLA-based thiol ligands and their derivatives provide QDs with enhanced colloidal stability over a wide range of buffer conditions due to their multidentate structures^{75, 149-153}. To further facilitate ligand exchange in a gentle manner, a two-step ligand exchange method was also incorporated as described¹⁵⁴.

We compared the absorption and fluorescence spectra of the blue-emitting QDs before and after ligand exchange¹⁴⁵. The spectral shape and position of the lowest absorption band after ligand exchange were essentially the same as those of the newly synthesized QDs, and the same trend was observed for the fluorescence spectra as well. This indicates that the intrinsic photophysical properties of the QDs were preserved during the ligand exchange. QYs of the blue-emitting QDs before and after ligand exchange were also measured. For ligand exchange of conventional CdSe/ZnS QDs, a ~50% or more decrease in QY after ligand exchange compared to the parent QD materials has been commonly reported^{112, 149, 155}. While the current blue-emitting multishell QDs prepared in this study still showed a ~20-45 % decrease in QY after ligand exchange, the values in water were still relatively high (QY ~0.2-0.3) compared with the original values measured for the as-prepared ZnSe/Cd_xZn_{1-x}/ZnS QDs. We surmise that the multishell formation helped to protect the ZnSe core, and the Cd_xZn_{1-x}S layers in between the ZnSe core and ZnS outer layers alleviated the lattice mismatch during the shell overcoating. When the ZnSe core is protected by multishell layers with

minimum surface strain, the QD fluorescence is expected to be less sensitive to surface modifications and reduction of the QY following ligand exchange can be minimized.

To assess the long-term colloidal stability of the blue-emitting QDs coated with our hydrophilic ligands, 0.5 μ M blue-emitting QDs coated with DHLA-PEG₇₅₀-OMe were dispersed in a wide range of pH buffers from pH 2 to 13 (Figure S9 in ¹⁴⁵). QD solutions showed good colloidal stability from weakly acidic (pH \geq 3~4) to basic pHs. At lower pHs (pH \leq 3~4), a partial or complete fluorescence quenching and sedimentation were observed similar to the results seen with CdSe/ZnS QDs coated with multidentate thiol ligands ^{75, 149}. The strongly acidic buffer results in “acidic” etching of the QD surface as well as destabilizing the ligand-to-QD coordination due to protonation of the thiol anchoring groups. The remaining QD dispersions were colloiddally stable in weakly acidic to strongly basic pH conditions (pH 5~12) without apparent fluorescence quenching for at least one year. In a similar manner, the colloidal stability of QDs coated with DHLA-PEG₇₅₀-OMe were examined under high salt concentration as well (data not shown). QDs were dispersed in 3M NaCl aqueous solution and the fluorescence of the colloidal solution was monitored over time. The QDs remained stable for over a year without any visible sign of aggregation or quenching.

Not only is long-term QD stability fundamental for biological applications but the issue of toxicity can also be exceedingly important when working with cells and tissues ^{83, 156}. We thus examined the cytotoxicity potential of blue-emitting QDs coated with DHLA-PEG₇₅₀-OMe on COS-1 cells using a standard colorimetric tetrazolium-based cell proliferation assay. This assay is commonly used to monitor inhibition of cellular proliferation especially when contemplating working with QDs ^{83, 157}. Equivalent

concentration ranges of unconjugated QDs and QDs conjugated to JB858 were exposed to COS-1 cells. Following washing, and a subsequent 48 h culture, we found no detrimental changes in proliferation for either unconjugated QDs (tested up to 200 nM) or QD-peptide assemblies (QD:peptide ratio of 1:30) relative to the untreated control (Figure 17E). We should note that no apparent toxicity has been observed for the same peptide when directly exposed to the cells alone as controls¹⁴⁷. Delivery of CdSe/ZnS QDs coated with the same ligands has also been demonstrated not to impair viability and proliferation in various cell lines and developing tissues^{147, 156, 158}.

Ratiometric pH Sensing Assay

We then coupled the QDs to fluorescein to construct a QD FRET-based ratiometric pH sensing system^{87, 159}. When used as FRET donors the fluorescence of the blue-emitting QDs can provide significant spectral overlap with the fluorescein acceptor absorption (450 to 500 nm). The 464 nm emitting QDs applied here have a reasonably high spectral overlap with fluorescein (Förster distance R_0 of 4.1 nm at pH 9) while its narrow fluorescence band is still well separated from the fluorescein emission allowing for a simple direct analysis without requiring spectral deconvolution. The conjugation chemistry using the current surface ligands is expected to keep the QD and fluorescein close enough for efficient energy transfer. Moreover, the ability to decorate the QD donor with multiple fluorescein acceptors will also increase the FRET efficiency since it proportionally increases the acceptor cross section and manifests practically as a larger R_0 ^{1, 13}.

In order to make the QD amenable for surface conjugation, the 464 nm emitting QDs were prepared using a 4:1 mixture of DHLA-PEG₇₅₀-OMe/DHLA-PEG₆₀₀-NH₂. The terminal amine groups on the QD surface provide a chemical handle for coupling to fluorescein isothiocyanate (FITC) which forms a stable thiourea bond with it (Figure 17A). In the labeling reaction, the amine-terminated QDs were mixed with a ~20-fold excess FITC in pH 9 buffer, the reaction mixture was stirred at room temperature in the dark for several hours and directly passed through a gel filtration column to remove the unbound dyes. During the conjugation reaction and subsequent purification, the QD solution showed no apparent sign of aggregation or precipitation. FITC conjugation on the QD surface was confirmed by agarose gel electrophoresis (Figure 17B). The pK_a of the amine group is ~9, and therefore the QD surface is expected to be positively charged to some degree in 1× TBE buffer (pH ~8.3). Corresponding to this, the 464 nm emitting QDs capped with 20% DHLA-PEG₆₀₀-NH₂ move towards the cathode under the applied electric field. The low QD mobility is presumably due to low surface coverage (20%) of the amine functional groups and the presence of the neutral methoxy groups in conjunction with the cumulative contributions from all the neutral PEG groups. On the other hand, free FITC moved toward the anode with high mobility due to its small size and negatively charged carboxyl groups. QD-FITC conjugates showed low mobility toward the anodic electrode since the positive charges of the amine terminal groups on the QDs were now masked by thiourea bonds and the negative charges of FITCs bound on the QDs counter the influence of any remaining unbound amines. FITC conjugation on the QD surface was also assessed using dynamic light scattering (DLS) measurements (Figure S12 in ¹⁴⁵). The hydrodynamic diameter of 464 nm emitting QDs with DHLA-

PEG₇₅₀-OMe/DHLA-PEG₆₀₀-NH₂ (4:1) was estimated to be 13.0 ± 0.5 nm. The hard diameter of the 464 nm emitting QD sample measured by TEM was 7.1 ± 0.52 nm. These measurement values are an average of at least 100 QDs for each sample. The difference between hydrodynamic size and the hard core/shell size arises from the hydrodynamic interactions of the ligand layer with the surrounding buffer⁷⁶. The contribution of the surface ligands to the hydrodynamic radius is ~ 3 nm, which falls within the range previously measured for different sized DHLA-PEG₇₅₀-OMe-coated QDs^{75, 154}. The conjugation of multiple FITC dyes at the terminal amine groups of the PEG ligands led to only slight increase of the hydrodynamic size ($13.9 \text{ nm} \pm 0.2 \text{ nm}$). DHLA-PEG₆₀₀-NH₂ is shorter than DHLA-PEG₇₅₀-OMe and serves to minimize any increase in the hydrodynamic size after FITC conjugation. Compact hydrodynamic size after FITC conjugation is also crucial to ensure efficient FRET between the QD and FITC and further reflects the excellent colloidal stability of the QD-FITC conjugates following chemical modification and purification steps. The absorption spectrum of the QD-FITC conjugates was easily deconvoluted into a simple sum of the individual spectra of QD and fluorescein dye, and the average number of conjugated FITC dyes per QD was estimated to be ~ 13.9 ¹⁴⁵. The QD-FITC conjugate fluorescence spectrum also showed two major peaks at 464 and 523 nm corresponding to the QD and FITC, respectively (Figure 17C).

For the ratiometric pH sensing assay, the conjugates were excited at 400 nm, where the absorption of FITC is lowest to minimize its direct excitation. The assay was carried out by monitoring the FRET acceptor intensity/donor intensity ratio, where the acceptor intensity corresponds to the FITC peak emission at 523 nm and the donor intensity corresponds to the QDs emission at 464 nm. Fluorescence peak intensities were monitored directly without correction since there was almost no spectral leakage at each fluorescence peak position from its counterpart. The intense FITC fluorescence signal at

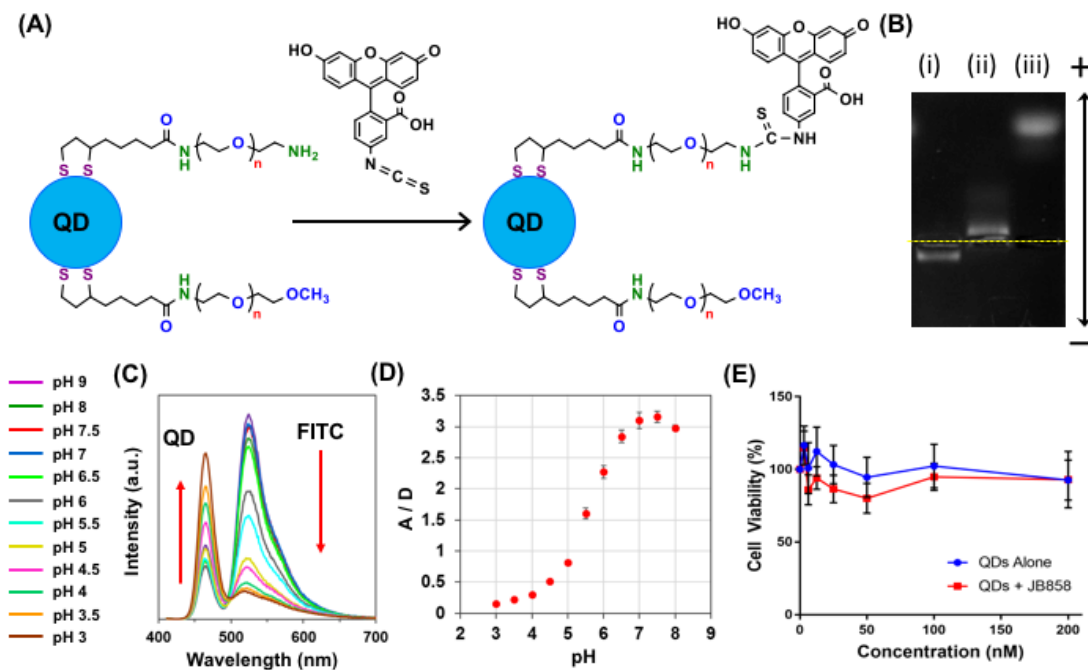


Figure 17. 464 nm QD-FITC FRET construct analysis. (A) Schematic representation of aqueous conjugation chemistry between the 464 nm emitting QDs coated with DHLA-PEG₇₅₀-OMe:DHLA-PEG₆₀₀-NH₂ (4:1) and FITC. (B) Gel electrophoretic separation of (i) the blue-emitting QDs coated with DHLA-PEG₇₅₀-OMe:DHLA-PEG₆₀₀-NH₂ (4:1), (ii) the QD-FITC conjugates, and (iii) FITC. Gels were run on 0.8% agarose gel in 1×TBE buffer (pH 8.3) at ~12 V/cm for ~30 min. The yellow dotted line indicates the position of wells. (C) Photoluminescent changes of the QD-FITC conjugates in different pH buffers. The sample was excited at 400 nm. (D) Plot of the FRET ratio (A(523 nm)/D(464 nm)) of the QD-FITC conjugates as a function of pH. (E) Cytotoxicity assay results demonstrating the effects of 483 nm emitting CdZnSe/Cd_{0.1}Zn_{0.9}S/ZnS core/shell QDs coated with DHLA-PEG₇₅₀-OMe (blue line) and the QD-JB858 conjugates (red line) on cellular proliferation of COS-1 cells.

523 nm at higher pH reflects FRET from the QD to the FITC bound to the PEG terminal. Excitation of the same concentration of FITC solution at 400 nm showed only ~6% of the fluorescence intensity of the QD-FITC conjugates, confirming significant sensitization of the FITC (data not shown). Analysis of the spectral data showed the FRET efficiency at pH 9 was 96.5%. As the pH was lowered, FITC fluorescence intensity decreased concomitant with a gradual recovery of the QD fluorescence (Figure 17C). Clearly, the changes to the pH-dependent spectral overlap between the QD and FITC drives the pH dependent spectral behavior of the QD-FITC conjugates. The FRET ratio increased with pH manifesting a generally sigmoidal function from pH 3 to ~7.5 (Figure 17D). Beyond pH 8, the FRET ratio was saturated and decreased slightly. In particular, the FRET ratio showed the most dynamic changes between pH 5 and 7, an ideal range for tumor microenvironment measurement.

Since ratiometric pH sensing in acidic buffers was successfully demonstrated, we next explored the conjugates pH sensing capability in extracellular environment. As nanoscale materials that are exposed to cells typically undergo endocytosis and subsequent cellular internalization, development of a technology to image acidic cellular microenvironments without the sensor itself being subjected to endocytosis is fundamental to detecting tumors and characterizing the relevant extracellular microenvironments. To accomplish this, we complexed the QD-FITC conjugates to the previously described JB858 peptide which localizes QDs to the plasma membrane stably for up to 48 hours following cellular exposure¹⁴⁷. JB858 was self-assembled on the QD-FITC conjugates at 1:40 QD:peptide molar ratio in DMEM/HEPES buffer just by simple mixing. The resulting conjugates were then exposed to COS-1 cells for extracellular

labeling and the fluorescence signal was monitored at different extracellular pHs using DPBS as the extracellular media.

As can be seen in Figure 18A, the majority of QD-FITC conjugates effectively labeled the plasma membranes. The green emission at pH 7 and 8 reflects that the fluorescence signal was dominated by FITC as expected from the pH sensing experiments described above. With stepwise decreases in pH down to 3 using buffer exchange, the emission color of the QD-FITC conjugates bound on the membranes progressively changed from green toward blue. The fluorescence spectra from 440 nm to 625 nm measured in 5 nm binned wavelengths were compiled for each of the pH levels and a representative set is shown in Figure 18B. As pH lowers, the FITC fluorescence decreases along with concomitant increase of the QD fluorescence; the trend is essentially the same as in Figure 17C. The fluorescence spectra were analyzed across multiple regions of interest ($n \geq 15$), and the average A/D ratios are plotted as shown in Figure 18C. The fluorescence spectra of the same QD-FITC conjugates assembled with JB858 were also measured in the same DPBS buffers as a control and the A/D ratios were compared (Figure 18D). As observed in the cellular images, the FRET ratios measured in the extracellular environments correlate to an increase in the pH and can be potentially used to monitor changes in extracellular pH. To investigate the potential for the QD-FITC system to identify the extracellular pH, a series of unknowns were analyzed. In a blind analysis, three DPBS solutions were arbitrarily chosen by another member of the lab and

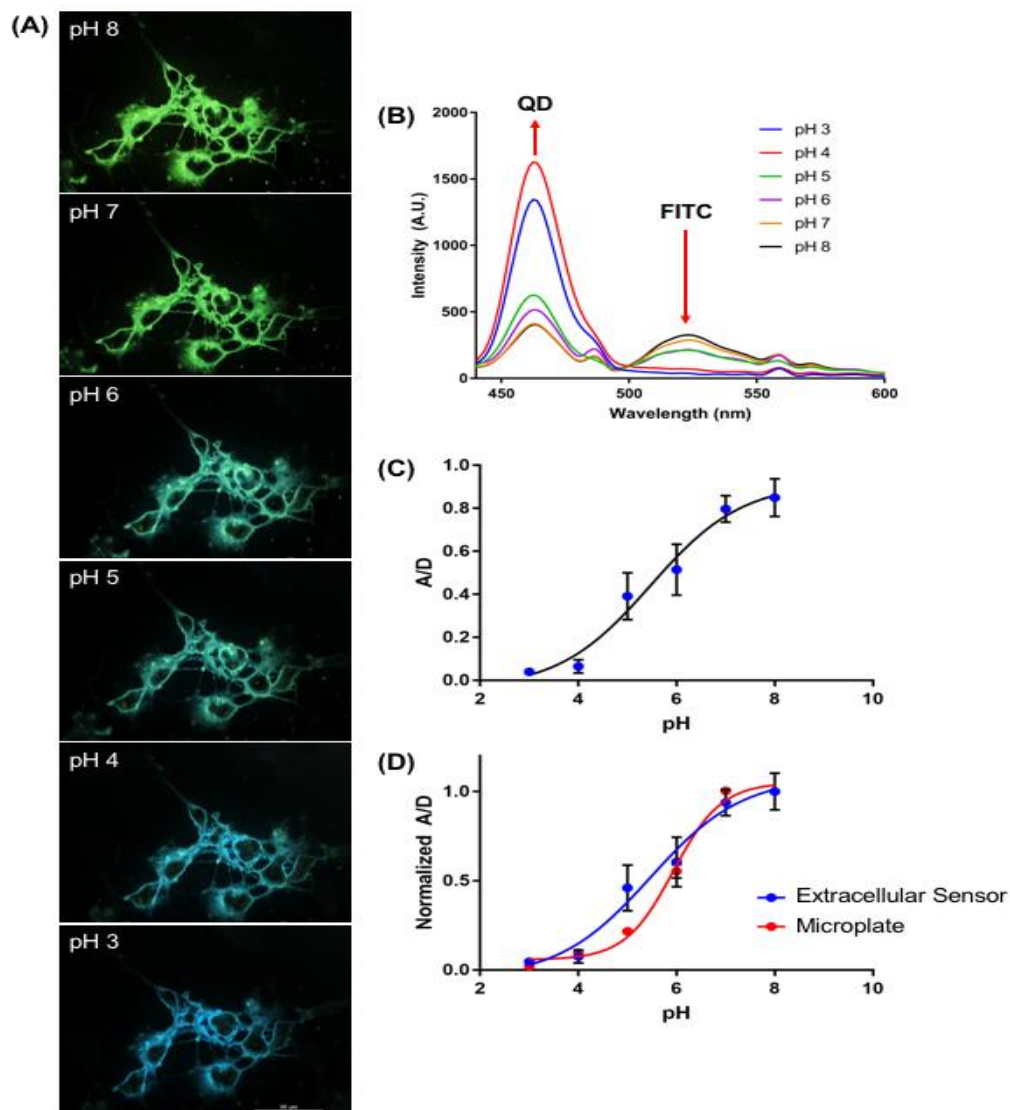
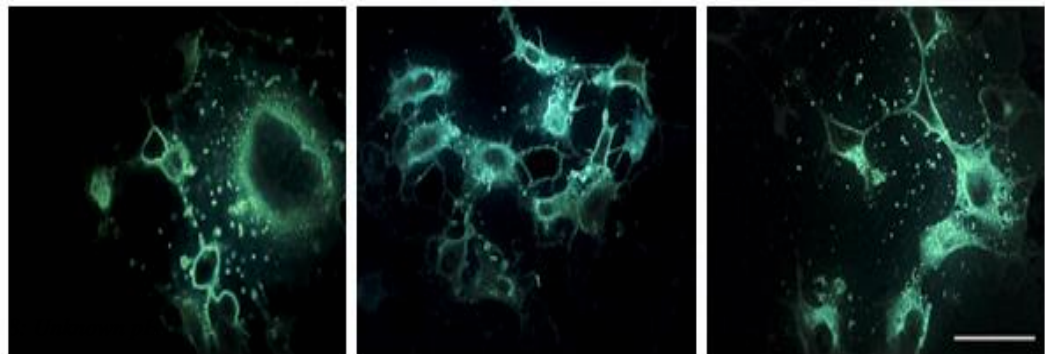


Figure 18. 464 nm QD-FITC Sensor Efficacy. (A) Representative images of the QD-FITC conjugates labeled using the membrane-localization peptide JB858 on COS-1 cells at the denoted pH levels. The images depict the spectral output from 440-625 nm in wavelength. The scale bar is 50 μ m. (B) Superimposed pH-dependent fluorescence spectra of the QD-FITC conjugates with self-assembled JB858 bound on cellular membranes. (C) Plot of the acceptor peak intensity (A) / donor peak intensity (D) of the QD-FITC conjugates with self-assembled JB858 as a function of pH while bound on cellular membranes. From the cell images at each pH, the QD and FITC peak intensities were extracted from the spectral data of at least 15 individual ROI's, and the FRET ratio was averaged. (D) Normalized A/D comparing the responsiveness of the QD-FITC conjugates measured in DPBS on a TECAN plate reader with those seen for the cellular images

labeled with A/B/C. Cells were labeled with the QD:FITC sensing system in the same manner as performed for the titration assay. Each of the unknown solutions were introduced to the cells, washed 2 times, and allowed to incubate in the unknown pH buffer for 15 minutes. Directly before imaging, the unknown buffer solution was replaced another 2 times to ensure that the final pH encountering the QD-FITC system was that of the unknown buffer. Images were taken and multiple ROIs were analyzed to determine the average A/D for each of the unknown pH's, this value is noted as the measured pH (Figure 19). Using the titration curve, the measured values of the unknown pHs were calculated and compared to the expected unknown values and found to be within 3% of the values expected using a pH meter.



Measured pH:	6.8 ± 0.2	5.2 ± 0.1	5.7 ± 0.1
Expected pH:	7	5.14	5.8
Relative Error:	-2.8%	2.3%	-2.0%

Figure 19. (A) Representative images of the QD-FITC conjugates labeled using the membrane-localization peptide JB858 on COS-1 cells at 3 unknown pH's. The images depict the spectral output from 440-625 nm in wavelength. The scale bar is 50 μ m. From the cell images at each pH, the QD and FITC peak intensities were extracted from the spectral data of at least 10 individual ROI's, and the A/D ratio was averaged. Using the A/D standard curve for the QD-FITC constructs, the unknown pH's were interpolated. The expected values and relative error for each unknown are shown.

We do note that the FRET ratio changes measured in the extracellular environment are not of the same magnitude as those measured in buffer solutions, although the response function is essentially the same as shown by the normalized data in Figure 15D. We have previously demonstrated that conjugation of His-tagged biomolecules onto QD surfaces often increases fluorescence intensity of the QDs; this enhancement has been explained as passivation of the QD surface trap states by coordination of the oligohistidine^{75, 160}. Despite the use of the same QD-FITC conjugates assembled with JB858 as control to cancel out the possible QD fluorescence enhancement promoted by the oligohistidine binding on the QD surfaces, the FRET ratios measured in the extracellular environments were still lower than those of the control samples at higher pHs. One possible reason under the present experimental conditions is self-quenching of FITC in the cellular membranous environments. It has been reported that fluorescein and other dyes aggregate in cellular membranes or vesicles and form nonfluorescent dimers¹⁶¹⁻¹⁶³. Energy transfer from monomer to the nonfluorescent dimer can lead to significant fluorescence quenching. Nevertheless, with careful calibration, the current QD-FITC conjugate system does show strong potential to monitor pH in biological environments.

Conclusions

Few studies focus on the design of extracellular pH sensors, with the majority of systems designed to monitor pH focusing on the intracellular endolysosomal pathway. Sensors that have been implemented for extracellular pH sensing rely on fluorescent probes that have limitations for long-term monitoring of localized pH, including chemical

and physical degradation, low QYs and susceptibility to photobleaching. QDs are ideal for overcoming many of these limitations given their superior optical properties, and specifically a new range of biocompatible blue-emitting QDs produced at NRL can provide a scaffold for extracellular pH sensing. Capitalizing on the pH-responsive nature of FITC and the tunable emission of the blue-emitting QDs, 464 nm emitting QDs were conjugated with FITC to produce a FRET-based pH sensor. This sensor was further colocalized to the exofacial leaflet of the cellular membrane in cultured cells and produced a robust pH sensor with a high degree of accuracy. This sensing design has the potential to be used in tumor monitoring and other instances where the pH of the localized microenvironment is of interest.

Chapter 5: Conclusions

Conclusions Overview

Producing an effective theranostic agent requires the careful consideration of many components, from the choice of parts to assembly of the system and the possible methods of cargo actuation, all while necessitating the ability to monitor what is happening in real-time. This project has focused on expanding our understanding of what is required to produce effective nanoscale theranostic systems. In order to build the effective ‘toolbox’ we examined multiple areas of interest including the surface chemistry of the NP scaffold used for construct design, the method of complex conjugation, and the intracellular location of assembly. We subsequently used the components of this ‘toolbox’ in the design of potential intracellular sensors and cargo actuation modalities. For all of these studies, we focused on the use of a proto-typical hard NP, namely - semiconductor quantum dot (QDs) as its optical properties afford easy monitoring potential.

First, in Chapter 2, we examined the efficacy of a FRET-based QD donor with mCherry used as an acceptor to determine the dependence of the chemistry and size of the capping ligand used to produce biocompatible QDs on the complex’s FRET efficiency (Figure 3). Additionally, the location of the final FRET construct inside the cells was analyzed for energy transfer efficiency optimization. To accomplish this analysis, cells were transfected with His₆-tagged mCherry proteins present in either the cytosol or appended to the inner leaflet of the cellular membrane. Cells expressing the proteins were then microinjected with QDs capped with a range of capping ligands, and the cells were imaged to determine the FRET potential for each system (*i.e.* each

capping-ligand at both expression localizations). The capping ligand used clearly needs to be balanced between the passivation of the QD surface for biocompatibility while still allowing for the acceptor protein to be close enough to the donor QD. As discussed in the Introduction, the relationship between FRET efficiency and donor-acceptor distance is dependent on an inverse 6th factor, so a few nanometers in size difference can dramatically lower the efficiency¹³. The two longer capping ligands, DHLA-PEG₇₅₀-OMe and DHLA-PEG₆₀₀-NTA have estimated end-to-end sizes larger than 6 nm which is over three times the size of the small CL4 capping ligand (~1.8 nm)¹⁰⁷. Coordination between the acceptor mCherry proteins and the QDs also varied for the capping ligand used, with the assembly driven by metal-affinity coordination for the PEG₇₅₀-OMe and CL4 capping ligands compared to Ni²⁺-NTA assembly for the PEG₆₀₀-NTA ligand. All of these factors contributed to our findings that the smallest, zwitterionic capping ligand CL4 produced the most efficient intracellular FRET both when associated to a cytosolically-expressed mCherry protein and to a transmembrane-appended mCherry. FRET efficiency produced by the complexed systems was also higher for the cytosolically-localized mCherry when compared to the transmembrane mCherry, which we attribute to the increased number of mCherry produced for cytosolic transfection and the steric hindrance caused by membrane-tethering the mCherry⁹⁶. By closely examining the components of surface chemistry and protein localization, we have shown that we can assemble efficient FRET sensors intracellularly, as opposed to introducing a pre-fabricated construct to the cellular environment. This directly suggests that such theranostic devices can utilize some of the cellular machinery already in place as part of its function. The capping ligand used for the design of intracellular sensing and actuation modalities must be chosen with care to

balance the necessity for stable colloidal QDs with the greatest FRET potential for visualization. Greater understanding of these individual components helps broaden the range of potential nanoparticle-based applications, be that for monitoring intracellular processes or the implementation of theranostic delivery agents.

Second, in Chapter 3, we used the knowledge gained in the first aim to produce a novel intracellular actuation modality. Instead of relying on triggered delivery using conventional approaches like a change in the localized environment around the NP surface (*e.g.* pH ²¹, REDOX ²³) or external application of a power source (*e.g.* ultrasound ²⁷, magnetism ²⁴), we decided to explore a new mechanism for triggering cargo release - the addition of an inert secondary triggering molecule. Again, using QDs capped with CL4 capping ligands as our NP scaffold, we conjugated a carrier protein to the surface called maltose binding protein (MBP). Within the binding pocket, a maltose analog β -cyclodextrin (β CD) acted as the carrier for both a dye (TF3) and a drug (DOX), each chosen to facilitate a visualizable FRET response after release (Figure 4). Once within the cytosol, actuation of the cargo occurred specifically in response to external delivery of maltose. We showed that the constructs functioned intracellularly, and responded in a visualizable manner to increasing addition of maltose extracellularly. This response tracked with both increased time and increasing maltose delivery, and the process occurred relatively quickly (<10 minutes) after maltose stimulation. This triggering mechanism using an innocuous secondary molecule is directly relevant to theranostics as it opens a new area for potential actuation methods that is more specific than passive delivery and does not have some of the limitations of other active triggering modalities. Specifically, intracellularly triggered systems necessitate a specified location for effective

delivery, be that in the endosomal pathway or in the cytosol, and extracellularly triggered systems require for the targeted site to be known and application of the external power source (light²⁵⁻²⁶, magnetism²⁴) can damage the surrounding tissue and have issues with depth penetration⁵⁸.

The actuation modality described in this dissertation is not reliant on location for release and has the potential to be targeted to specific cells through the addition of peptides or other targeting moieties. Using the sugar molecule maltose, in this example, means that there will be few systemic side effects given that maltose is consumed readily as it is the carbon source for bread and beer production and can be easily removed from the diet. Although we have proven that this type of actuation modality is a viable release mechanism, there are many hurdles still to overcome in implementing such a system. These include the long-term stability of the actuatable conjugate to ensure a low amount of cargo ‘leaking’ with effective targeting concentrations, the need to target the construct to a specific area within the body to ensure correct targeting, and the necessary dosing for both the NP complex and the secondary triggering molecule. Additionally, the use of the His₆ tag could produce severe immune reactions if the MBP dissociates from the QD surface, and if the treatment required multiple doses of the NP complex. Shortening the histidine tag would overcome these issues, and we have previously shown that His₅ tags can still efficiently coordinate to the QD surface¹⁰⁸. This actuation system utilizes the tools we’ve delineated in Chapter 2, showing one of the potential application possibilities that can be produced from our components.

Finally, in Chapter 4, we used that same toolbox to tackle a difficult sensing application, that of monitoring the extracellular pH in live cells. This area of research is

of interest given the lowering in pH that occurs in tumor microenvironments. With this area changing from a normal pH of around 7.5 to as low as 5, a system that could effectively monitor the extracellular environment would be of benefit to researchers ⁹⁵. Again, using the QD as a central scaffold, pH-responsive FITC molecules were appended to the surface and the whole complex was coordinated to the exofacial leaflet of the cellular membrane through the use of the peptide JB858 (Figure 5). The QDs utilized in this design are unique, however, in that they were specifically designed to be stable and emit in the blue range of wavelengths. Commonly used QDs have a CdSe core that is difficult to stabilize at the extremely small sizes required for emission below 500 nm, and addition of the protective ZnS shell shifts the emission wavelength further to the red ¹⁴⁵. To overcome this, a Zn-doped CdS core was produced where the Zn was ratiometrically increased during synthesis, displacing the Cd and producing larger, and more stable, blue-emitting QDs. These new QDs were ideal as a FRET donor for FITC, and we showed in Chapter 4 that this FRET pair could quantifiably measure localized pH around the cellular membrane. Additionally, the system was robust enough to accurately determine ‘unknown’ pH values within 3% of the experimental value. This promising system could be used to image the pH change in the tumor microenvironment over time. Implementing such a system in a tumor model would require careful optimization of the delivery method, including timing, peptide ratio and sensor concentration, which could be made easier by the enhanced permeability and retention (EPR) effect that occurs in many tumor sites ¹³⁶. Other considerations for real-time imaging in tissue would have to take into account the depth of imaging required (which can be increased through the use of two-photon excitation of the QD ¹⁶⁴), the effect of tissue localization on the titration

curve of the sensor and the long-term localization of the sensor in tissue samples. This effective sensing technique was built using the understanding gained through analysis of available nanoscale tools that have the potential to be applied to numerous systems.

This dissertation specifically contributed to our understanding of what is required for QD donors and FRET-based monitoring for use in nanoscale cellular sensing systems. The first aim of this dissertation specifically showed how critical the QD capping ligand is for both intracellular stability and the QD's ability to assemble to acceptor proteins intracellularly. Additionally, we showed how it is possible to assemble FRET constructs to specific locations within the cell by modifying the location of the expressed acceptor protein. This research expanded the possibilities for implementing intracellular monitoring systems by reducing the number of components that need to be synthesized outside the cell and allowing for targeting to be incorporated into the acceptor protein instead of through the use of other targeting modalities that would take up precious space on the QD surface and reduce the overall FRET efficiency of the designed system. The second aim used the information learned from the first to successfully interrogate a novel method for cargo actuation that could be monitored using the same QD donor and FRET-based monitoring. This type of extracellularly- triggered release of cargo has not been shown previously and is unique in that it does not rely on 1) achieving a specified location within the cell to trigger release as is required for active- intracellular actuation or 2) the knowledge of the location of the targeted treatment location as is required for current active- extracellularly triggered actuation. Instead, cargo release can occur wherever the location is simply by systemically delivering the innocuous triggering molecule maltose. This method adds one more potential specified delivery modality to

the growing field of theranostic systems. Finally, our final aim again used the same QD donor scaffold and FRET-based monitoring components to try to target an under-served area of tumor research by designing a new extracellular pH sensor. Using a new range of biologically stable, blue-emitting QDs and a proprietary extracellular labeling peptide, we capitalized on the inherent responsiveness of FITC to its localized pH environment as the FRTE acceptor molecule to produce the extracellular pH sensor. This system is one of very few sensors that monitor the extracellular pH and is the only one that utilizes this FRET-based method of sensing, which increases the possible tools available for cancer researchers for use in studying tumor microenvironments.

Overall, we hope this work has displayed the incredible potential NPs provide for the design and implementation of sensing and actuation complexes. This is a difficult and complicated process and increasing the available methods for monitoring intracellular processes or the types of specified triggering for drug delivery can only help facilitate future breakthroughs.

Future Directions

Each of the specific aims in this dissertation can be built upon to further advance the design of nanoscale theranostic agents. From Chapter 2, we produced the building blocks for potential intracellular sensors that can be complexed directly in the cell. Using QDs in these systems has numerous benefits, including their large 2 photon cross section¹⁶⁴, their ability to act as a good FRET donor, their tunable emission for a range of acceptor molecules for optimum FRET efficiency, and that multiple acceptors can be appended to one QD donor¹. In addition to using mCherry as the intracellular acceptor,

one of the numerous GFP analogs could be used to produce a wide range of visualizable FRET pairs within the cell. Many labs are modifying these proteins to have even better photophysical properties, like the protein mScarlet, which emits in the same range as mCherry but has superior optical properties (QY ~70% compared to mCherry QY at ~20%)¹⁶⁵. These proteins could be used to build even more efficient intracellular FRET complexes. Possible future avenues for study using these FRET complexes include the addition of cleavable regions between the histidine tag and the acceptor protein to assess intracellular enzyme activity. Once cleaved, the acceptor protein would no longer associate with the QD surface and the FRET efficiency of the system would change. This could be applied to numerous intracellular signaling pathways that rely on enzymatic activity to induce cellular responses. One such process is the apoptotic pathway, which activates enzymes called caspases in a signaling cascade to induce cellular death¹⁶⁶. Other possible intracellular responses include reactions to hormone stimulation like insulin¹⁶⁷ or kinase signaling pathways¹⁶⁸ that could be monitored intracellularly, comparing normal function to drug inhibition or stimulation. There are a wide range of processes that could be examined more closely by implementing such a FRET-based intracellular complex.

Future work with the actuation modality from Chapter 3 would need to look at the longer-term stability of the structure in a cellular environment. We looked at the system for up to 6 hours intracellularly but for specified delivery the assembly would need to be studied over longer delivery periods. This stability would be critical for delivery to targets within the body, as it would take time for the delivered complex to accumulate in the desired location, and so should also be examined while in more complex media than

the HBSS used in this dissertation. In addition to the long-term stability the binding kinetics of the β CD-TF3/DOX to the MBP while in the presence of other sugars and glycoproteins and glycolipids that would be present on the exofacial leaflet of cellular membranes should be examined as this could cause unwanted displacement of the cargo. In addition to determining the stability, a wide array of methods could be examined to target the complex to the desired cellular location. Incorporation of internalization modalities like the HIV derived TAT peptide or the use of JB858 or its internalization analog JB577 could introduce the complex to different areas of the cells and would need to be studied for the amount of peptide to MBP required for efficient targeting. If specific locations within the body were to be targeted, antibodies or molecules could also be associated with the QD surface and would need to undergo the same analysis as the intracellular targeting peptide to maximize cargo capacity and targeting efficiency. The final aspect that must be examined to determine the potential for this system to be effectively implemented *in vivo* is the determination of how maltose will be administered to stimulate release. If injected, the amount of maltose that enters the bloodstream would have to be discerned and if injected, the amount and circulation time of maltose would need to be studied to determine what doses the targeted locations received. For both of these delivery methods, it should be stated that an extremely large amount of maltose could cause issues like insulin disruption and glycemic shock and should be taken into consideration.

To apply this complex to a larger range of diseases, a wider range of delivery cargos could be examined for the system's efficacy based on cargo size. It would be interesting to see if the β CD could facilitate delivery of larger cargos like proteins, or if

that would be too unwieldy. This could increase the application potential for this cargo system to treat diseases other than cancer. Finally, the binding kinetics of the MBP could also be modified to be more or less responsive to the added maltose, which could provide slower delivery methods compared to the less than 10-minute release times shown in this research ¹⁶⁹. This could be ideal as MBP could interact with the aforementioned glycoproteins and glycolipids, and so modifying the protein to be more specified to the cargo and displacement molecule could increase the delivery efficacy. Alternative carrier proteins could be studied as well, with periplasmic binding proteins being specific for a range of molecules (various sugars ¹⁷⁰, amino acids ¹⁷¹, metals ¹⁷²⁻¹⁷³ and even vitamins ¹⁷⁴) or the use of DNA aptamers designed to release in response to a delivered molecule ¹⁷⁵. This could be ideal in cancerous cells that have a high number of multiple drug resistance (MDR) pumps present in their cytoplasm, and so a slower rate of delivery would prevent loss of drug ¹⁷⁶. We believe that this novel actuation system holds much potential for future directions in theranostic agents, providing a new way for specified drug release and delivery intracellularly from just the addition of an extracellular trigger – namely an innocuous nutrient.

Finally, there are future directions that should be explored using our pH sensor from Chapter 4. First, the system should be introduced to cancerous cell lines to determine if those cells produce an acidic local environment around the cells, and then secondarily used to label actual tumor sites to measure their localized pH *in vivo*. Additionally, the ability of the system to label a three-dimensional tumor would need to be investigated. As one of the key features of tumor development is the loss of sufficient blood flow to the entire tumor, the requirements for sufficient delivery would need to be

examined for both cultured tumor models and physical tumors *in vivo*. One interesting avenue of research could be to monitor non-tumor sites and determine if a change can be discerned in the pH around cells. If there is a pH change, could it occur before cancerous mutations are discovered - possibly providing a first warning sign for tumor models. Additionally, this sensor could eventually be coupled to therapeutic delivery. By varying the number of FITC per QD, surface area on the QD could be freed to carry cargo in addition to the sensing functionality. To produce a triggered release, acid-labile linkages could be used between the histidine tag and the drug analog¹⁷⁷. As the pH lowers around the cancerous cells, the sensing function would report on the localized conditions and the drug would be released for a therapeutic effect - producing another theranostic, multifunctional agent. The possibilities for drug delivery are widespread, but one promising option is doxorubicin, as it would allow for a secondary imaging possibility once it reached the nucleus.

This dissertation has attempted to broaden the available methods for the design of theranostic agents. Each of the specific aims worked to introduce new techniques that can be further applied to future delivery modalities and sensing systems. As we become more and more fluent in the production of new hybrid bio-nano materials and their use in new configurations, the potential for new nanoscale tools grows exponentially.

Appendix

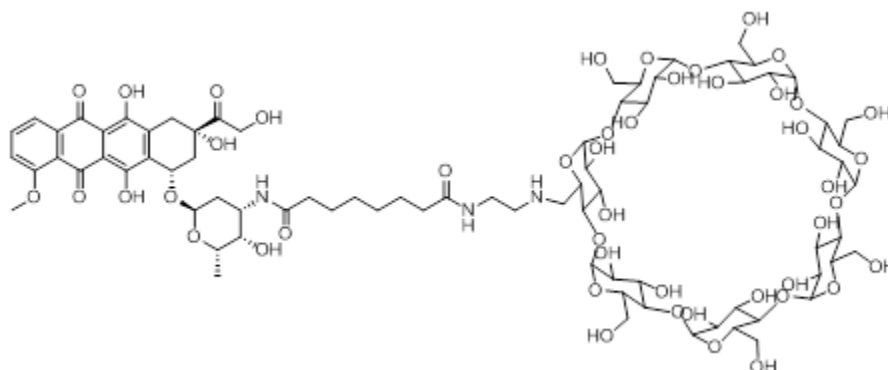
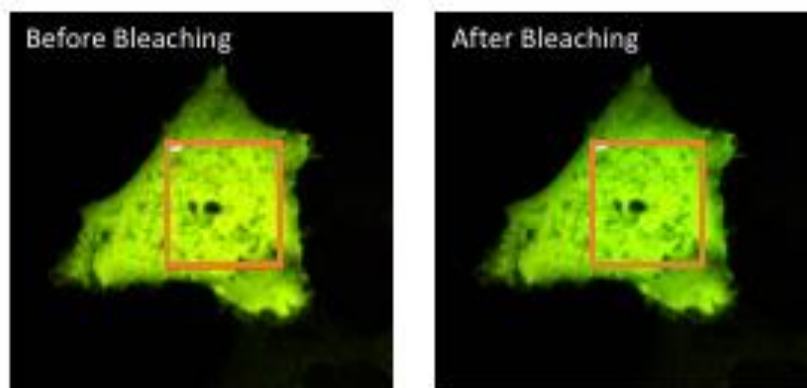


Figure A1: Schematic of synthesized β CD-DOX.



N	23
FRET E Range	20.0-30.3
FRET E Average	0.24
STDEV	0.04

Figure A2: Representative images and data from FRET bleaching experiments. COS-1 cells injected with QD-MBP- β CD-TF3 and imaged spectrally from 430nm – 730 nm. Red highlighted region on interest was bleached using a 561 nm laser to remove the TF3 fluorescence. Using the spectral profiles from before and after bleaching and Equation 3, the FRET efficiency was calculated over n=23 cells. Data shown in table.

$$Y = \frac{B_{\max} \cdot X}{K_d + X}$$

Figure A3: Rate equation used for maltose delivery analysis

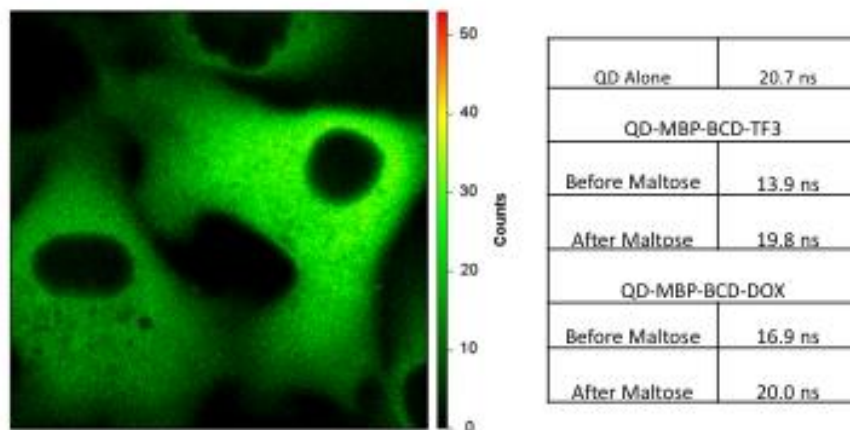


Figure A4: Representative image and data from FLIM analysis. COS-1 cells injected with QD alone, QD-MBP- β CD-TF3, and QD-MBP- β CD-DOX were imaged using a FLIM microscope. Representative image shows QDs alone and the average counts captured over time for the injected cells. Table shows lifetime data collected for both of the QD constructs before and after 30 mM maltose addition compared to that shown by QDs alone.

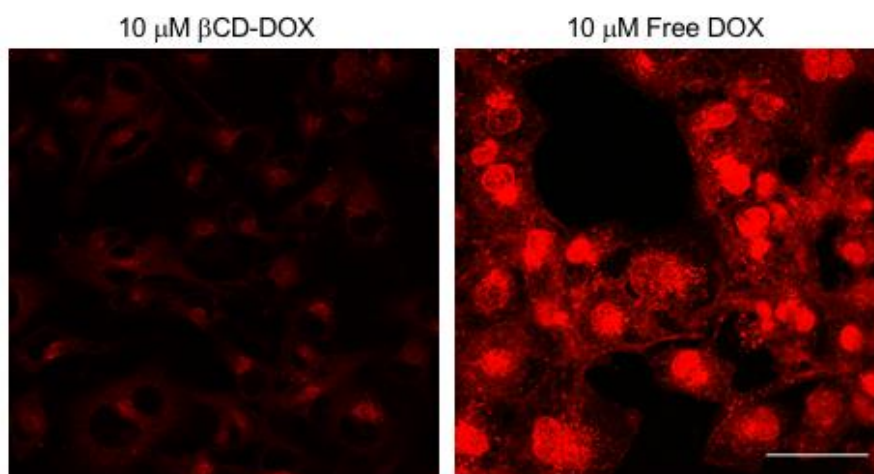


Figure A5: β CD-DOX and free DOX delivery comparison. COS-1 cells treated for 2 hours with 10 μ M β CD-DOX or free DOX and imaged for DOX localization.

References:

1. Hildebrandt, N.; Spillmann, C. M.; Algar, W. R., *et al.*, Energy transfer with semiconductor quantum dot bioconjugates: A versatile platform for biosensing, energy harvesting, and other developing applications. *Chem Rev* **2017**, *117* (2), 536-711.
2. Nag, O. K.; Field, L. D.; Chen, Y., *et al.*, Controlled actuation of therapeutic nanoparticles: an update on recent progress. *Ther Deliv* **2016**, *7* (5), 335-52.
3. Kelkar, S. S.; Reineke, T. M., Theranostics: combining imaging and therapy. *Bioconjug Chem* **2011**, *22* (10), 1879-903.
4. Ho, Y. P.; Leong, K. W., Quantum dot-based theranostics. *Nanoscale* **2010**, *2* (1), 60-8.
5. Picard, F. J.; Bergeron, M. G., Rapid molecular theranostics in infectious diseases. *Drug Discov Today* **2002**, *7* (21), 1092-101.
6. Chen, Y.; Zhu, C.; Cen, J., *et al.*, Ratiometric detection of pH fluctuation in mitochondria with a new fluorescein/cyanine hybrid sensor. *Chem Sci* **2015**, *6* (5), 3187-3194.
7. Lee, M. H.; Park, N.; Yi, C., *et al.*, Mitochondria-immobilized pH-sensitive off-on fluorescent probe. *J Amer Chem Soc* **2014**, *136* (40), 14136-14142.
8. Srivastava, J.; Barber, D. L.; Jacobson, M. P., Intracellular pH sensors: design principles and functional significance. *Physiology* **2007**, *22* (1), 30-39.
9. Han, J.; Burgess, K., Fluorescent indicators for intracellular pH. *Chem Revi* **2010**, *110* (5), 2709-2728.
10. Sugiura, K.; Nagai, T.; Nakano, M., *et al.*, Redox sensor proteins for highly sensitive direct imaging of intracellular redox state. *Biochem Biophys Res Commun* **2015**, *457* (3), 242-8.
11. Tada, M.; Ohashi, M.; Shiratori, Y., *et al.*, Analysis of K-ras gene mutation in hyperplastic duct cells of the pancreas without pancreatic disease. *Gastroenterology* **1996**, *110* (1), 227-231.

12. Blackstock, D.; Chen, W., Halo-tag mediated self-labeling of fluorescent proteins to molecular beacons for nucleic acid detection. *Chem Commun* **2014**, 50 (89), 13735-13738.
13. Lakowicz, J. R., *Principles of Fluorescence Spectroscopy*. 3rd ed.; Springer: New York, 2006; p xxvi, 954 p.
14. Delehanty, J. B.; Susumu, K.; Manthe, R. L., *et al.*, Active cellular sensing with quantum dots: transitioning from research tool to reality; a review. *Anal Chim Acta* **2012**, 750, 63-81.
15. Ruedas-Rama, M. J.; Walters, J. D.; Orte, A., *et al.*, Fluorescent nanoparticles for intracellular sensing: a review. *Anal Chim Acta* **2012**, 751, 1-23.
16. Nazareus, M.; Zhang, Q.; Soliman, M. G., *et al.*, In vitro interaction of colloidal nanoparticles with mammalian cells: What have we learned thus far? *Beilstein J Nanotechnol* **2014**, 5, 1477-1490.
17. Paranjpe, M.; Müller-Goymann, C., Nanoparticle-mediated pulmonary drug delivery: A review. *Int J Mol Sci* **2014**, 15 (4), 5852.
18. Ryzolova, M.; Chomoucka, J.; Drbohlavova, J., *et al.*, Modern micro and nanoparticle-based imaging techniques. *Sensors* **2012**, 12 (11), 14792.
19. Delehanty, J. B.; Medintz, I. L., Controlled actuation of therapeutic nanoparticles: moving beyond passive delivery modalities. *Ther Deliv* **2013**, 4 (2), 127-9.
20. Delehanty, J. B.; Breger, J. C.; Gemmill, K. B., *et al.*, Controlling the actuation of therapeutic nanomaterials: enabling nanoparticle-mediated drug delivery. *Ther Deliv* **2013**, 4 (11), 1411-29.
21. Samanta, D.; Meiser, J. L.; Zare, R. N., Polypyrrole nanoparticles for tunable, pH-sensitive and sustained drug release. *Nanoscale* **2015**, 7 (21), 9497-504.
22. Hou, X. F.; Chen, Y.; Liu, Y., Enzyme-responsive protein/polysaccharide supramolecular nanoparticles. *Soft Matter* **2015**, 11 (12), 2488-93.

23. Wang, Y.; Han, N.; Zhao, Q., *et al.*, Redox-responsive mesoporous silica as carriers for controlled drug delivery: a comparative study based on silica and PEG gatekeepers. *Eur J Pharm Sci* **2015**, *72*, 12-20.
24. Hayashi, K.; Nakamura, M.; Miki, H., *et al.*, Magnetically responsive smart nanoparticles for cancer treatment with a combination of magnetic hyperthermia and remote-control drug release. *Theranostics* **2014**, *4* (8), 834-44.
25. Timko, B. P.; Arruebo, M.; Shankarappa, S. A., *et al.*, Near-infrared-actuated devices for remotely controlled drug delivery. *Proc Natl Acad Sci U S A* **2014**, *111* (4), 1349-54.
26. Yin, W.; Yan, L.; Yu, J., *et al.*, High-throughput synthesis of single-layer MoS₂ nanosheets as a near-infrared photothermal-triggered drug delivery for effective cancer therapy. *ACS Nano* **2014**, *8* (7), 6922-6933.
27. Yang, P.; Li, D.; Jin, S., *et al.*, Stimuli-responsive biodegradable poly(methacrylic acid) based nanocapsules for ultrasound traced and triggered drug delivery system. *Biomaterials* **2014**, *35* (6), 2079-88.
28. Oh, E.; Delehanty, J. B.; Sapsford, K. E., *et al.*, Cellular uptake and fate of PEGylated gold nanoparticles is dependent on both cell-penetration peptides and particle size. *ACS Nano* **2011**, *5* (8), 6434-6448.
29. Alkilany, A. M.; Murphy, C. J., Toxicity and cellular uptake of gold nanoparticles: what we have learned so far? *J Nanopart Res* **2010**, *12* (7), 2313-2333.
30. Giljohann, D. A.; Seferos, D. S.; Daniel, W. L., *et al.*, Gold nanoparticles for biology and medicine. *Angew Chem Int Ed Engl* **2010**, *49* (19), 3280-94.
31. He, H.; Xie, C.; Ren, J., Nonbleaching fluorescence of gold nanoparticles and its applications in cancer cell imaging. *Anal Chem* **2008**, *80* (15), 5951-7.
32. Popovtzer, R.; Agrawal, A.; Kotov, N. A., *et al.*, Targeted gold nanoparticles enable molecular CT imaging of cancer. *Nano Lett* **2008**, *8* (12), 4593-6.
33. Seo, J. M.; Kim, E. B.; Hyun, M. S., *et al.*, Self-assembly of biogenic gold nanoparticles and their use to enhance drug delivery into cells. *Colloids Surf B Biointerfaces* **2015**, *135*, 27-34.

34. Cheng, Y.; C. Samia, A.; Meyers, J. D., *et al.*, Highly efficient drug delivery with gold nanoparticle vectors for in vivo photodynamic therapy of cancer. *J Amer Chem Soc* **2008**, *130* (32), 10643-10647.
35. Kumar, A.; Zhang, X.; Liang, X., Gold nanoparticles: emerging paradigm for targeted drug delivery system. *Biotech Adv* **2013**, *31* (5), 593-606.
36. Di Marco, A.; Cassinelli, G.; Arcamone, F., The discovery of daunorubicin. *Cancer Treat Rep* **1981**, *65 Suppl 4*, 3-8.
37. Wang, X.; Sun, X.; Lao, J., *et al.*, Multifunctional graphene quantum dots for simultaneous targeted cellular imaging and drug delivery. *Colloids Surf B Biointerfaces* **2014**, *122*, 638-44.
38. Bellini, M.; Mazzucchelli, S.; Galbiati, E., *et al.*, Protein nanocages for self-triggered nuclear delivery of DNA-targeted chemotherapeutics in Cancer Cells. *J Control Release* **2014**, *196*, 184-196.
39. Ding, Q.; Si, X.; Liu, D., *et al.*, Targeting and liposomal drug delivery to CD40L expressing T cells for treatment of autoimmune diseases. *J Control Release* **2015**, *207*, 86-92.
40. Spillmann, C. M.; Naciri, J.; Algar, W. R., *et al.*, Multifunctional liquid crystal nanoparticles for intracellular fluorescent imaging and drug delivery. *ACS Nano* **2014**, *8* (7), 6986-6997.
41. Suk, J. S.; Xu, Q.; Kim, N., *et al.*, PEGylation as a strategy for improving nanoparticle-based drug and gene delivery. *Adv Drug Deliv Rev* **2016**, *99* (Pt A), 28-51.
42. Nelson, C. E.; Kintzing, J. R.; Hanna, A., *et al.*, Balancing cationic and hydrophobic content of PEGylated siRNA polyplexes enhances endosome escape, stability, blood circulation time, and bioactivity *in vivo*. *ACS Nano* **2013**, *7* (10).
43. Kamaly, N.; Xiao, Z.; Valencia, P. M., *et al.*, Targeted polymeric therapeutic nanoparticles: design, development and clinical translation. *Chem Soc Rev* **2012**, *41* (7), 2971-3010.
44. Pelaz, B.; Alexiou, C.; Alvarez-Puebla, R. A., *et al.*, Diverse applications of nanomedicine. *ACS Nano* **2017**, *11* (3), 2313-2381.

45. Gabizon, A. A., Pegylated liposomal doxorubicin: metamorphosis of an old drug into a new form of chemotherapy. *Cancer Invest* **2001**, *19* (4), 424-36.
46. Bobo, D.; Robinson, K. J.; Islam, J., *et al.*, Nanoparticle-based medicines: A review of FDA-approved materials and clinical trials to date. *Pharm Res* **2016**, *33* (10), 2373-87.
47. Kato, Y.; Ozawa, S.; Miyamoto, C., *et al.*, Acidic extracellular microenvironment and cancer. *Cancer Cell Int* **2013**, *13* (1), 1-8.
48. Liang, K.; Such, G. K.; Johnston, A. P., *et al.*, Endocytic pH-triggered degradation of nanoengineered multilayer capsules. *Adv Mater* **2014**, *26* (12), 1901-5.
49. Huang, P.; Song, H.; Wang, W., *et al.*, Integrin-targeted zwitterionic polymeric nanoparticles with acid-induced disassembly property for enhanced drug accumulation and release in tumor. *Biomacromolecules* **2014**, *15* (8), 3128-3138.
50. Zolata, H.; Abbasi Davani, F.; Afarideh, H., Synthesis, characterization and theranostic evaluation of Indium-111 labeled multifunctional superparamagnetic iron oxide nanoparticles. *Nucl Med Biol* **2015**, *42* (2), 164-70.
51. Hwang, C.; Sinsky, A.; Lodish, H., Oxidized redox state of glutathione in the endoplasmic reticulum. *Science* **1992**, *257* (5076), 1496-1502.
52. Chen, X.; Sun, H.; Hu, J., *et al.*, Transferrin gated mesoporous silica nanoparticles for redox-responsive and targeted drug delivery. *Colloids Surf B Biointerfaces* **2017**, *152*, 77-84.
53. Liu, J.; Zhang, B.; Luo, Z., *et al.*, Enzyme responsive mesoporous silica nanoparticles for targeted tumor therapy in vitro and in vivo. *Nanoscale* **2015**, *7* (8), 3614-26.
54. Park, E.-J.; Umh, H.; Choi, D.-H., *et al.*, Magnetite- and maghemite-induced different toxicity in murine alveolar macrophage cells. *Arch Toxicol* **2014**, *88* (8), 1607-1618.
55. Soenen, S. J.; De Cuyper, M.; De Smedt, S. C., *et al.*, Investigating the toxic effects of iron oxide nanoparticles. *Methods Enzymol*, Nejat, D., Ed. Academic Press: 2012; Vol. Volume 509, pp 195-224.

56. Lee, J.-H.; Chen, K.-J.; Noh, S.-H., *et al.*, On-demand drug release system for *in vivo* cancer treatment through self-assembled magnetic nanoparticles. *Angew Chem Int Ed Engl* **2013**, *52* (16), 4384-4388.
57. Hu, X.; Tian, J.; Liu, T., *et al.*, Photo-triggered release of caged camptothecin prodrugs from dually responsive shell cross-linked micelles. *Macromolecules* **2013**, *46* (15), 6243-6256.
58. Kielbassa, C.; Roza, L.; Epe, B., Wavelength dependence of oxidative DNA damage induced by UV and visible light. *Carcinogenesis* **1997**, *18* (4), 811-816.
59. Qin, Y.; Chen, J.; Bi, Y., *et al.*, Near-infrared light remote-controlled intracellular anti-cancer drug delivery using thermo/pH sensitive nanovehicle. *Acta Biomater* **2015**, *17* (0), 201-209.
60. Pugliese, D.; Maiorano, E.; Pascone, M., Histopathological features of tissue alterations induced by low frequency ultrasound with cavitation effects on human adipose tissue. *Int J Immunopathol Pharmacol* **2013**, *26* (2), 541-7.
61. Ninomiya, K.; Yamashita, T.; Kawabata, S., *et al.*, Targeted and ultrasound-triggered drug delivery using liposomes co-modified with cancer cell-targeting aptamers and a thermosensitive polymer. *Ultrason Sonochem* **2014**, *21* (4), 1482-1488.
62. Steigerwald, M. L.; Brus, L. E., Synthesis, stabilization, and electronic structure of quantum semiconductor nanoclusters. *Annu Rev Mat Sci* **1989**, *19* (1), 471-495.
63. Dabbousi, B. O.; RodriguezViejo, J.; Mikulec, F. V., *et al.*, (CdSe)ZnS core-shell quantum dots: Synthesis and characterization of a size series of highly luminescent nanocrystallites. *J Phys Chem B* **1997**, *101* (46), 9463-9475.
64. Alivisatos, A. P., Semiconductor clusters, nanocrystals, and quantum dots. *Science* **1996**, *271* (5251), 933-937.
65. Medintz, I. L.; Uyeda, H. T.; Goldman, E. R., *et al.*, Quantum dot bioconjugates for imaging, labelling and sensing. *Nat Mater* **2005**, *4* (6), 435-46.
66. Michalet, X.; Pinaud, F. F.; Bentolila, L. A., *et al.*, Quantum dots for live cells, *in vivo* imaging, and diagnostics. *Science* **2005**, *307* (5709), 538-44.

67. Berezin, M. Y.; Achilefu, S., Fluorescence lifetime measurements and biological imaging. *Chem Rev* **2010**, *110* (5), 2641-84.
68. Efros, A. L.; Rosen, M., The electronic structure of semiconductor nanocrystals 1. *Annu Rev Mat Sci* **2000**, *30* (1), 475-521.
69. Mei, B. C.; Susumu, K.; Medintz, I. L., *et al.*, Modular poly(ethylene glycol) ligands for biocompatible semiconductor and gold nanocrystals with extended pH and ionic stability. *J Mat Chem* **2008**, *18* (41), 4949-4958.
70. Resch-Genger, U.; Grabolle, M.; Cavaliere-Jaricot, S., *et al.*, Quantum dots versus organic dyes as fluorescent labels. *Nat Methods* **2008**, *5* (9), 763-75.
71. Massey, M.; Wu, M.; Conroy, E. M., *et al.*, Mind your P's and Q's: the coming of age of semiconducting polymer dots and semiconductor quantum dots in biological applications. *Curr Opin Biotechnol* **2015**, *34*, 30-40.
72. Bilan, R.; Fleury, F.; Nabiev, I., *et al.*, Quantum dot surface chemistry and functionalization for cell targeting and imaging. *Bioconjug Chem* **2015**, *26* (4), 609-24.
73. Chan, W. C. W.; Nie, S., Quantum Dot Bioconjugates for Ultrasensitive Nonisotopic Detection. *Science* **1998**, *281* (5385), 2016-2018.
74. Mattoussi, H.; Mauro, J. M.; Goldman, E. R., *et al.*, Self-Assembly of CdSe–ZnS Quantum Dot Bioconjugates Using an Engineered Recombinant Protein. *J Amer Chem Soc* **2000**, *122* (49), 12142-12150.
75. Susumu, K.; Oh, E.; Delehanty, J. B., *et al.*, Multifunctional Compact Zwitterionic Ligands for Preparing Robust Biocompatible Semiconductor Quantum Dots and Gold Nanoparticles. *J Amer Chem Soc* **2011**, *133*, 9480-9496.
76. Pons, T.; Uyeda, H. T.; Medintz, I. L., *et al.*, Hydrodynamic dimensions, electrophoretic mobility, and stability of hydrophilic quantum dots. *J Phys Chem B* **2006**, *110* (41), 20308-16.
77. Dennis, A. M.; Sotto, D. C.; Mei, B. C., *et al.*, Surface ligand effects on metal-affinity coordination to quantum dots: implications for nanoprobe self-assembly. *Bioconjug Chem* **2010**, *21* (7), 1160-70.

78. Algar, W. R.; Susumu, K.; Delehanty, J. B., *et al.*, Semiconductor quantum dots in bioanalysis: crossing the valley of death. *Anal Chem* **2011**, *83* (23), 8826-37.
79. Mahamuni, S.; Borgohain, K.; Bendre, B., *et al.*, Spectroscopic and structural characterization of electrochemically grown ZnO quantum dots. *J Appl Phys* **1999**, *85* (5), 2861-2865.
80. Aboulaich, A.; Balan, L.; Ghanbaja, J., *et al.*, Aqueous route to biocompatible ZnSe: Mn/ZnO core/shell quantum dots using 1-thioglycerol as stabilizer. *Chem Mater* **2011**, *23* (16), 3706-3713.
81. Yang, X.; Zhao, D.; Leck, K. S., *et al.*, Full visible range covering InP/ZnS nanocrystals with high photometric performance and their application to white quantum dot light-emitting Diodes. *Adv Mater* **2012**, *24* (30), 4180-4185.
82. Yong, K.-T.; Law, W.-C.; Hu, R., *et al.*, Nanotoxicity assessment of quantum dots: from cellular to primate studies. *Chem Soc Rev* **2013**, *42* (3), 1236-1250.
83. Oh, E.; Liu, R.; Nel, A., *et al.*, Meta-analysis of cellular toxicity for cadmium-containing quantum dots. *Nat Nano* **2016**, *11* (5), 479-486.
84. Chen, X.; Tang, Y.; Cai, B., *et al.*, 'One-pot' synthesis of multifunctional GSH-CdTe quantum dots for targeted drug delivery. *Nanotechnology* **2014**, *25* (23), 235101.
85. Medintz, I. L.; Pons, T.; Susumu, K., *et al.*, Resonance energy transfer between luminescent quantum dots and diverse fluorescent protein acceptors. *J Phys Chem C Nanomater Interfaces* **2009**, *113* (43), 18552-18561.
86. Dif, A.; Boulmedais, F.; Pinot, M., *et al.*, Small and stable peptidic PEGylated quantum dots to target polyhistidine-tagged proteins with controlled stoichiometry. *J Amer Chem Soc* **2009**, *131* (41), 14738-46.
87. Dennis, A. M.; Rhee, W. J.; Sotito, D., *et al.*, Quantum dot-fluorescent protein FRET probes for sensing intracellular pH. *ACS Nano* **2012**, *6* (4), 2917-24.
88. Shaheen, S. M.; Akita, H.; Yamashita, A., *et al.*, Quantitative analysis of condensation/decondensation status of pDNA in the nuclear sub-domains by QD-FRET. *Nucleic Acids Res* **2011**, *39* (7), e48.

89. Heyduk, T., Measuring protein conformational changes by FRET/LRET. *Curr Opin Biotech* **2002**, *13* (4), 292-296.
90. Truong, K.; Ikura, M., The use of FRET imaging microscopy to detect protein-protein interactions and protein conformational changes *in vivo*. *Curr Opin Struct Biol* **2001**, *11* (5), 573-8.
91. Lipman, E. A.; Schuler, B.; Bakajin, O., *et al.*, Single-molecule measurement of protein folding kinetics. *Science* **2003**, *301* (5637), 1233-1235.
92. Mank, M.; Reiff, D. F.; Heim, N., *et al.*, A FRET-based calcium biosensor with fast signal kinetics and high fluorescence change. *Biophys J* **2006**, *90* (5), 1790-1796.
93. Boeneman, K.; Delehanty, J. B.; Susumu, K., *et al.*, Intracellular bioconjugation of targeted proteins with semiconductor quantum dots. *J Amer Chem Soc* **2010**, *132* (17), 5975-7.
94. Shamirian, A.; Ghai, A.; Snee, P. T., QD-Based FRET Probes at a Glance. *Sensors (Basel)* **2015**, *15* (6), 13028-51.
95. Gerweck, L. E.; Seetharaman, K., Cellular pH gradient in tumor versus normal tissue: potential exploitation for the treatment of cancer. *Cancer research* **1996**, *56* (6), 1194-1198.
96. Field, L. D.; Walper, S. A.; Susumu, K., *et al.*, Modulation of intracellular quantum dot to fluorescent protein forster resonance energy transfer via customized ligands and spatial control of donor-acceptor assembly. *Sensors* **2015**, *15* (12), 30457-68.
97. Dreifuss, T.; Betzer, O.; Shilo, M., *et al.*, A challenge for theranostics: is the optimal particle for therapy also optimal for diagnostics? *Nanoscale* **2015**.
98. Kumar, R.; Shin, W. S.; Sunwoo, K., *et al.*, Small conjugate-based theranostic agents: an encouraging approach for cancer therapy. *Chem Soc Rev* **2015**.
99. Goldsmith, C. R.; Jaworski, J.; Sheng, M., *et al.*, Selective labeling of extracellular proteins containing polyhistidine sequences by a fluorescein-nitrilotriacetic acid conjugate. *J Amer Chem Soc* **2006**, *128* (2), 418-9.

100. Guignet, E. G.; Hovius, R.; Vogel, H., Reversible site-selective labeling of membrane proteins in live cells. *Nat Biotechnol* **2004**, *22* (4), 440-4.
101. Fessenden, J. D., Förster resonance energy transfer measurements of ryanodine receptor type 1 structure using a novel site-specific labeling method. *PLoS ONE* **2009**, *4* (10), e7338.
102. Yip, K. P.; Cha, B. J.; Tse, C. M., *et al.*, Functional expression of aquaporin-2 tagged with photoconvertible fluorescent protein in mpkCCD cells. *Cell Physiol Biochem* **2015**, *36* (2), 670-682.
103. Los, G. V.; Encell, L. P.; McDougall, M. G., *et al.*, HaloTag: a novel protein labeling technology for cell imaging and protein analysis. *ACS Chem Biol* **2008**, *3* (6), 373-82.
104. Adams, S. R.; Tsien, R. Y., Preparation of the membrane-permeant biarsenicals FAsH-EDT2 and ReAsH-EDT2 for fluorescent labeling of tetracysteine-tagged proteins. *Nat Protoc* **2008**, *3* (9), 1527-34.
105. Lee, M. J.; Cho, Y. A.; Hwang, H. J., *et al.*, Development of in-cell imaging assay systems for MMP-2 and MMP-9 based on trans-localizing molecular beacon proteins. *Arch Pharm Res* **2015**, *38* (6), 1099-107.
106. Mercanti, V.; Marchetti, A.; Lelong, E., *et al.*, Transmembrane domains control exclusion of membrane proteins from clathrin-coated pits. *J Cell Sci* **2010**, *123* (Pt 19), 3329-35.
107. Susumu, K.; Oh, E.; Delehanty, J. B., *et al.*, Multifunctional compact zwitterionic ligands for preparing robust biocompatible semiconductor quantum dots and gold nanoparticles. *J Amer Chem Soc* **2011**, *133* (24), 9480-96.
108. Susumu, K.; Medintz, I. L.; Delehanty, J. B., *et al.*, Modification of poly(ethylene glycol)-capped quantum dots with nickel nitrilotriacetic acid and self-assembly with histidine-tagged proteins. *J Phys Chem C* **2010**, *114* (32), 13526-13531.
109. Oh, E.; Fatemi, F. K.; Currie, M., *et al.*, PEGylated luminescent gold nanoclusters: synthesis, characterization, bioconjugation, and application to one- and two-photon cellular imaging. *Part Part Syst Charact* **2013**, *30* (5), 453-466.

110. Clapp, A. R.; Medintz, I. L.; Mauro, J. M., *et al.*, Fluorescence resonance energy transfer between quantum dot donors and dye-labeled protein acceptors. *J Amer Chem Soc* **2004**, *126* (1), 301-10.
111. Prasuhn, D. E.; Deschamps, J. R.; Susumu, K., *et al.*, Polyvalent display and packing of peptides and proteins on semiconductor quantum dots: predicted versus experimental results. *Small* **2010**, *6* (4), 555-64.
112. Dai, M.-Q.; Yung, L.-Y. L., Ethylenediamine-assisted ligand exchange and phase transfer of oleophilic quantum dots: stripping of original ligands and preservation of photoluminescence. *Chem Mater* **2013**, *25*, 2193-2201.
113. Tamang, S.; Beaune, G.; Texier, I., *et al.*, Aqueous phase transfer of InP/ZnS nanocrystals conserving fluorescence and high colloidal stability. *ACS Nano* **2011**, *5* (12), 9392-402.
114. Nazarenus, M.; Zhang, Q.; Soliman, M. G., *et al.*, In vitro interaction of colloidal nanoparticles with mammalian cells: What have we learned thus far? *Beilstein J Nanotechnol* **2014**, *5*, 1477-90.
115. Resh, M. D., Palmitoylation of ligands, receptors, and intracellular signaling molecules. *Sci STKE* **2006**, *2006* (359), re14.
116. Sebti, S. M., Protein farnesylation: implications for normal physiology, malignant transformation, and cancer therapy. *Cancer Cell* **2005**, *7* (4), 297-300.
117. Lange, A.; Mills, R. E.; Lange, C. J., *et al.*, Classical nuclear localization signals: definition, function, and interaction with importin alpha. *J Biol Chem* **2007**, *282* (8), 5101-5.
118. Tiwari, G.; Tiwari, R.; Sriwastawa, B., *et al.*, Drug delivery systems: An updated review. *Int J Pharm Investig* **2012**, *2* (1), 2-11.
119. Jacques, S. L., Optical properties of biological tissues: a review. *Phys Med Bio* **2013**, *58* (11), R37.
120. Medintz, I. L.; Goldman, E. R.; Lassman, M. E., *et al.*, A fluorescence resonance energy transfer sensor based on maltose binding protein. *Bioconjugate Chem* **2003**, *14* (5), 909-918.

121. Gemmill, K. B.; Díaz, S. n. A.; Blanco-Canosa, J. B., *et al.*, Examining the polyproline nanoscopic ruler in the context of quantum dots. *Chem Mat* **2015**, *27* (18), 6222-6237.
122. Bagalkot, V.; Zhang, L.; Levy-Nissenbaum, E., *et al.*, Quantum dot-aptamer conjugates for synchronous cancer imaging, therapy, and sensing of drug delivery based on bi-fluorescence resonance energy transfer. *Nano Lett* **2007**, *7* (10), 3065-70.
123. Mohan, P.; Rapoport, N., Doxorubicin as a molecular nanotheranostic agent: effect of doxorubicin encapsulation in micelles or nanoemulsions on the ultrasound-mediated intracellular delivery and nuclear trafficking. *Mol Pharm* **2010**, *7* (6), 1959-73.
124. Prabakaran, M.; Graier, J. J.; Pilla, S., *et al.*, Amphiphilic multi-arm-block copolymer conjugated with doxorubicin via pH-sensitive hydrazone bond for tumor-targeted drug delivery. *Biomaterials* **2009**, *30* (29), 5757-5766.
125. Qiu, L. Y.; Wang, R. J.; Zheng, C., *et al.*, Beta-cyclodextrin-centered star-shaped amphiphilic polymers for doxorubicin delivery. *Nanomedicine* **2010**, *5* (2), 193-208.
126. Ferenci, T.; Muir, M.; Lee, K.-S., *et al.*, Substrate specificity of the Escherichia coli maltodextrin transport system and its component proteins. *Biochim Biophys Acta* **1986**, *860* (1), 44-50.
127. Szmelcman, S.; Schwartz, M.; Silhavy, T. J., *et al.*, Maltose transport in Escherichia coli K12. *Eur J Biochem* **1976**, *65* (1), 13-19.
128. Miller, D. M., 3rd; Olson, J. S.; Pflugrath, J. W., *et al.*, Rates of ligand binding to periplasmic proteins involved in bacterial transport and chemotaxis. *J Biol Chem* **1983**, *258* (22), 13665-72.
129. Leturque, A.; Brot-Laroche, E.; Le Gall, M., *et al.*, The role of GLUT2 in dietary sugar handling. *J Physiol Biochem* **2005**, *61* (4), 529-37.
130. Colville, C. A.; Seatter, M. J.; Jess, T. J., *et al.*, Kinetic analysis of the liver-type (GLUT2) and brain-type (GLUT3) glucose transporters in Xenopus oocytes: substrate specificities and effects of transport inhibitors. *Biochem J* **1993**, *290* (Pt 3), 701-6.
131. Statistics, NCH, Health, United States, 2015: with special feature on racial and ethnic health disparities. **2016**.

132. Vogelstein, B.; Kinzler, K. W., Cancer genes and the pathways they control. *Nat Med* **2004**, *10* (8), 789-799.
133. Kleinsmith, L. J., *Principles of Cancer Biology*. Benjamin-Cummings Publishing Company: 2006.
134. Carmeliet, P.; Jain, R. K., Angiogenesis in cancer and other diseases. *Nature* **2000**, *407* (6801), 249.
135. Maeda, H.; Wu, J.; Sawa, T., *et al.*, Tumor vascular permeability and the EPR effect in macromolecular therapeutics: a review. *J Cont Rel* **2000**, *65* (1), 271-284.
136. Fang, J.; Nakamura, H.; Maeda, H., The EPR effect: unique features of tumor blood vessels for drug delivery, factors involved, and limitations and augmentation of the effect. *Adv Drug Deliv Rev* **2011**, *63* (3), 136-151.
137. Sjöback, R.; Nygren, J.; Kubista, M., Absorption and fluorescence properties of fluorescein. *Spectrochim. Acta, Part A* **1995**, *51*, L7-L21.
138. Slyusareva, E. A.; Gerasimova, M. A., pH-dependence of the absorption and fluorescent properties of fluorone dyes in aqueous solutions. *Russ. Phys. J.* **2014**, *56*, 1370-1377.
139. Xu, J.; Sun, L.; Li, J., *et al.*, FITC and Ru(phen)₃²⁺ co-doped silica particles as visualized ratiometric pH indicator. *Nanoscale Res Lett* **2011**, *6* (1), 561.
140. Kreft, O.; Javier, A. M.; Sukhorukov, G. B., *et al.*, Polymer microcapsules as mobile local pH-sensors. *J Mater Chem* **2007**, *17* (42), 4471-4476.
141. Ke, G.; Zhu, Z.; Wang, W., *et al.*, A cell-surface-anchored ratiometric fluorescent probe for extracellular pH sensing. *ACS Appl Mater Interfaces* **2014**, *6* (17), 15329-34.
142. Ritter, S. C.; Milanick, M. A.; Meissner, K. E., Encapsulation of FITC to monitor extracellular pH: a step towards the development of red blood cells as circulating blood analyte biosensors. *Biomed Opt Express* **2011**, *2* (7), 2012-21.

143. Kobayashi, S.; Nakase, I.; Kawabata, N., *et al.*, Cytosolic targeting of macromolecules using a pH-dependent fusogenic peptide in combination with cationic liposomes. *Bioconjug Chem* **2009**, *20* (5), 953-9.
144. Iversen, T. G.; Skotland, T.; Sandvig, K., Endocytosis and intracellular transport of nanoparticles: Present knowledge and need for future studies. *Nano Today* **2011**, *6* (2), 176-185.
145. Susumu, K.; Field, L. D.; Oh E., *et al.*, Blue-emitting multishell quantum dots: synthesis, characterization and application for ratiometric extracellular pH sensing. *Chem Mater* **Submitted 05/17**
146. Prasuhn, D. E.; Feltz, A.; Blanco-Canosa, J. B., *et al.*, Quantum dot peptide biosensors for monitoring caspase 3 proteolysis and calcium ions. *ACS Nano* **2010**, *4*, 5487-5497.
147. Boeneman, K.; Delehanty, J. B.; Blanco-Canosa, J. B., *et al.*, Selecting improved peptidyl motifs for cytosolic delivery of disparate protein and nanoparticle materials. *ACS Nano* **2013**, *7*, 3778-3796.
148. Liu, D.; Snee, P. T., Water-soluble semiconductor nanocrystals cap exchanged with metalated ligands. *ACS Nano* **2011**, *5*, 546-550.
149. Susumu, K.; Uyeda, H. T.; Medintz, I. L., *et al.*, Enhancing the stability and biological functionalities of quantum dots via compact multifunctional ligands. *J Amer Chem Soc* **2007**, *129*, 13987-13996.
150. Muro, E.; Pons, T.; Lequeux, N., *et al.*, Small and stable sulfobetaine zwitterionic quantum dots for functional live-cell imaging. *J Amer Chem Soc* **2010**, *132*, 4556-4557.
151. Park, J.; Nam, J.; Won, N., *et al.*, Compact and stable quantum dots with positive, negative, or zwitterionic surface: specific cell interactions and non-specific adsorptions by the surface charges. *Adv Funct Mater* **2011**, *21*, 1558-1566.
152. Zhou, D.; Li, Y.; Hall, E. A. H., *et al.*, A chelating dendritic ligand capped quantum dot: preparation, surface passivation, bioconjugation and specific DNA detection. *Nanoscale* **2011**, *3*, 201-211.

153. Zhan, N.; Palui, G.; Safi, M., *et al.*, Multidentate zwitterionic ligands provide compact and highly biocompatible quantum dots. *J Amer Chem Soc* **2013**, *135*, 13786-13795.
154. Susumu, K.; Oh, E.; Delehanty, J. B., *et al.*, A new Family of pyridine-appended multidentate polymers as hydrophilic surface ligands for preparing stable biocompatible quantum dots. *Chem Mater* **2014**, *26*, 5327-5344.
155. Breus, V. V.; Heyes, C. D.; Nienhaus, G. U., Quenching of CdSe-ZnS core-shell quantum dot luminescence by water-soluble thiolated ligands. *J Phys Chem* **2007**, *111*, 18589-18594.
156. Agarwal, R.; Domowicz, M. S.; Schwartz, N. B., *et al.*, Delivery and tracking of quantum dot peptide bioconjugates in an intact developing avian brain. *ACS Chem Neurosci*. **2015**, *6*, 494-504.
157. Bradburne, C. E.; Delehanty, J. B.; Gemmill, K. B., *et al.*, Cytotoxicity of quantum dots used for *in vitro* cellular labeling: Role of QD surface ligand, delivery modality, cell type, and direct comparison to organic fluorophores. *Bioconjugate Chem* **2013**, *24*, 1570-1583.
158. Delehanty, J. B.; Bradburne, C. E.; Boeneman, K., *et al.*, Delivering quantum dot-peptide bioconjugates to the cellular cytosol: Escaping from the endolysosomal system. *Integr Biol* **2010**, *2*, 265-277.
159. Snee, P. T.; Somers, R. C.; Nair, G., *et al.*, A ratiometric CdSe/ZnS nanocrystal pH sensor. *J Amer Chem Soc* **2006**, *128* (41), 13320-13321.
160. Medintz, I. L.; Clapp, A. R.; Mattoussi, H., *et al.*, Self-assembled nanoscale biosensors based on quantum dot FRET donors. *Nat Mater* **2003**, *2* (9), 630-638.
161. Chen, R. F.; Knutson, J. R., Mechanism of fluorescence concentration quenching of carboxyfluorescein in liposomes: Energy transfer to nonfluorescent dimers. *Anal Biochem* **1988**, *172*, 61-77.
162. MacDonald, R. I., Characteristics of self-quenching of the fluorescence of lipid-conjugated rhodamine in membranes. *J Biol Chem* **1990**, *265*, 13533-13539.

163. Swiecicki, J.-M.; Thiebaut, F.; Pisa, M. D., *et al.*, How to unveil self-quenched fluorophores and subsequently map the subcellular distribution of exogenous peptides. *Sci Rep* **2016**, *6*, 20237.
164. Clapp, A. R.; Pons, T.; Medintz, I. L., *et al.*, Two-photon excitation of quantum-dot-based fluorescence resonance energy transfer and its applications. *Adv Mater* **2007**, *19* (15), 1921-1926.
165. Bindels, D. S.; Haarbosch, L.; van Weeren, L., *et al.*, mScarlet: a bright monomeric red fluorescent protein for cellular imaging. *Nat Methods* **2017**, *14* (1), 53-56.
166. Boeneman, K.; Mei, B. C.; Dennis, A. M., *et al.*, Sensing caspase 3 activity with quantum dot-fluorescent protein assemblies. *J Amer Chem Soc* **2009**, *131* (11), 3828-9.
167. Kubota, T.; Kubota, N.; Kadowaki, T., Imbalanced insulin actions in obesity and type 2 diabetes: Key mouse models of insulin signaling pathway. *Cell Metab* **25** (4), 797-810.
168. McKinnon, B. D.; Kocbek, V.; Nirgianakis, K., *et al.*, Kinase signalling pathways in endometriosis: potential targets for non-hormonal therapeutics. *Hum Reprod* **2016**, *22* (3), 382-403.
169. Walker, I. H.; Hsieh, P. C.; Riggs, P. D., Mutations in maltose-binding protein that alter affinity and solubility properties. *Appl Microbiol Biotechnol* **2010**, *88* (1), 187-97.
170. Lansky, S.; Salama, R.; Solomon, H. V., *et al.*, Structure-specificity relationships in Abp, a GH27 beta-L-arabinopyranosidase from *Geobacillus stearothermophilus* T6. *Acta Crystallogr D Biol Crystallogr* **2014**, *70* (Pt 11), 2994-3012.
171. Trakhanov, S.; Vyas, N. K.; Luecke, H., *et al.*, Ligand-free and -bound structures of the binding protein (LivJ) of the *Escherichia coli* ABC leucine/isoleucine/valine transport system: trajectory and dynamics of the interdomain rotation and ligand specificity. *Biochemistry* **2005**, *44* (17), 6597-608.
172. Sharma, N.; Selvakumar, P.; Saini, G., *et al.*, Crystal structure analysis in Zn²⁺-bound state and biophysical characterization of CLas-ZnuA2. *Biochim Biophys Acta* **2016**, *1864* (12), 1649-1657.

173. Sun, X.; Baker, H. M.; Ge, R., *et al.*, Crystal structure and metal binding properties of the lipoprotein MtsA, responsible for iron transport in *Streptococcus pyogenes*. *Biochemistry* **2009**, *48* (26), 6184-90.
174. Karpowich, N. K.; Huang, H. H.; Smith, P. C., *et al.*, Crystal structures of the BtuF periplasmic-binding protein for vitamin B12 suggest a functionally important reduction in protein mobility upon ligand binding. *J Biol Chem* **2003**, *278* (10), 8429-34.
175. He, X.; Zhao, Y.; He, D., *et al.*, ATP-responsive controlled release system using aptamer-functionalized mesoporous silica nanoparticles. *Langmuir* **2012**, *28* (35), 12909-12915.
176. Gillet, J. P.; Gottesman, M. M., Mechanisms of multidrug resistance in cancer. *Methods Mol Biol* **2010**, *596*, 47-76.
177. Kim, Y. H.; Park, J. H.; Lee, M., *et al.*, Polyethylenimine with acid-labile linkages as a biodegradable gene carrier. *J Control Release* **2005**, *103* (1), 209-19.